UNIVERSITY OF OTTAWA

DOCTORAL THESIS

Kerr Effect at the THz Frequencies

Author: Payman Rasekh

Supervised by: Prof. Ksenia Dolgaleva

A thesis submitted in Partial fulfillment of the requirements

for the degree of Doctor of Philosophy

Ottawa-Carleton Institute for Electrical and Computer Engineering

University of Ottawa

To Zora,

for her love, support and encouragement

Acknowledgments

It is with immense gratitude that I acknowledge the support and help of my supervisor Prof. Ksenia Dolgaleva for providing me with the opportunity of doing this research and patiently guiding me through it. I have gained invaluable experience being a member of her research team and always felt supported during my studies. Her constructive comments, insightful feedback, and endless support were essential for any steps toward the progress of my research.

It was an honor to work with Prof. Robert Boyd. I am thankful to him for his great mentoring, support, and guidance. I really appreciate working with him and learned extensively from him.

I cannot find words to express my gratitude to Prof. Jean-Michel Ménard for his healthy criticism and mentoring. This thesis would have remained a dream had it not been for his mentoring and supervision.

I am grateful to Prof. Ravi Bhardwaj. This thesis would not have been possible without his support and mentoring. He kindly let us use his laser facility, and he always provided

wise supervision.

I would also like to thank my fellow teammates, who were involved in the progress of this research. My fellow labmate, Dr. Murat Yildirim, helped me with optimizing the experimental setup as well as performing the measurements, as discussed in Chapter 2. Also, Dr. Akbar Safari helped me develop the theory, discussed in Chapter 4. He was also my very good friend and mentor who was always available for me. Soheil Zibod helped me with the data analysis, as discussed in Chapter 5. When I started this Ph.D. program, I could not imagine learning the skills of optical experiments with such detail and efficiency. Especial thanks to Dr. Deepak Kallepalli for helping me with my first experiment, and thanks to Dr. Mikko J. Huttunen for his generous and insightful help.

I am indebted to my colleagues who taught me the skills of nano-fabrication: Kashif M. Awan, Sebastian Schulz, Jeremy Upham, and Tony Olivieri.

I would especially like to acknowledge my friends and colleagues with whom I interacted the most at uOttawa: Md Saad Bin Alam, Shayan Saeidi, Ehsan Mobini, Kaustubh Vyas, Daniel Espinosa, Orad Reshef, Mitra Rahimian, Maryam Amiri, Tuhin Paul, Hugo Begin, Gloria Kaneza and many others.

Last, and by no means least, I am endlessly grateful to my family: my lovely wife, Zora, for her countless sacrifices and support who stood by me through all my travail; my parents Mahvash and Abolghasem, and my siblings: Parivash, Pezhman, and Niloufar for their love, encouragement and always understanding me.

Abstract

This doctoral dissertation focuses on the nonlinear optical response of water vapour as well as some solids at terahertz (THz) frequencies. In this study, the propagation of broadband single-cycle THz pulses through a medium with the third-order nonlinear optical response is theoretically investigated. Also, a technique to measure the nonlinear response of transparent materials based on the time-domain THz spectroscopy is developed, which provides frequency dispersion curves of the nonlinear Kerr coefficient (n_2).

A numerical model is used to simulate the THz pulse propagation. This model takes into account non-paraxial effects, self-focusing, and diffraction, as well as dispersion, in both the linear and nonlinear optical regimes. The contribution of non-instantaneous Kerr-type nonlinearity to the overall instantaneous and delayed Kerr effect at the THz frequencies is investigated. It is shown how increasing the nonlinear relaxation time and its dispersion modifies the THz pulse after the propagation through a transparent medium. The effect of linear dispersion on self-action during pulse propagation is also discussed.

Moreover, the nonlinear spectroscopy of water vapour at THz frequencies is reported.

Atmospheric water vapour has a rich spectrum with several strong resonances at frequencies below 3 THz, falling within the range of operation of most existing THz sources. An extremely large nonlinear response to THz radiation is observed at the positions of these resonances. Using the optical Kerr model for the nonlinear response, a minimum nonlinear refractive index of the order of 10^2 m^2/W is estimated. The results provide insight into the energy levels of the water molecule and give a more accurate picture of its response to electromagnetic radiation, paving the way to more accurate THz spectroscopy, imaging, and sensing systems, and thereby facilitating future emerging THz technologies.

Finally, the nonlinear response of solids at THz frequencies is studied. It has been shown that a phonon-induced THz Kerr effect can result in a larger nonlinear refractive index than the nonlinear refractive index at the visible or near-infrared range (optical Kerr effect). This pronounced nonlinear optical behavior is verified using a time-domain characterization approach. The results indicate a large delay occurred to the THz fields as they transmit through some of the material samples. In the frequency domain, the induced nonlinear phase shift of the intense THz field is shown to be relatively large of the order of 0.1 rad. From the phase information, the nonlinear phase is extracted by which the dispersion profile of n_2 is obtained.

Contents

List of Tables

List of Figures

1. Introduction

Electromagnetic radiation in the frequency range from around 0.1 to 10 THz is known as Terahertz (THz) radiation. This frequency range corresponds to the wavelength range from 3000 to 30 μm. While THz radiation stands between the visible and near-infrared region on one side of the electromagnetic spectrum and the Microwave region on the other side, it exhibits very different properties when it comes to interaction of light with matter. Hence, THz radiation provides the window to study and control some properties of materials that are not accessible through other frequency ranges. However, efficient generation and detection of THz radiation are exceedingly nontrivial, which makes this field relatively unexplored. Reducing the energy of the visible photons generated by electron transitions in a semiconductor material is inhibited since the energy of the THz photon is less than the thermal energy at room temperature. On the other hand, increasing the microwave operating frequency is bounded by the carrier mobility of the oscillating semiconductor [1]. Hence, approaching the THz frequencies from either of these bounding frequency regions of the visible and microwaves brings unique challenges. There are a few established techniques to generate THz radiation and to detect it in a coherent process. This enables THz spectroscopy where the material response to THz radiation is studied by observing

the changes occurred to amplitude and phase of the transmitted or reflected THz field.

1.1 THz Time-Domain Spectroscopy

THz time-domain spectroscopy (THz-TDS) is a powerful technique for characterizing the response of materials to the THz electric field. It plays an important role in the fields of material science [2], chemistry [3], medicine [4] and engineering [5]. In the field of material science, it can be used to measure the charge carriers which leads to the measurement of conductivity [6], topological insulators [7], superconductors [8] and phase transitions in these materials [9]. Moreover, THz-TDS provides an effective tool to study two-dimensional materials such as Graphene [10]. In the field of chemistry, THz-TDS is commonly used to study the molecular structure of the materials as well as their inter-molecular motions [3]. To this end, it is mainly the spectral features in the spectroscopy measurement data that help to unlock this information. For instance, to observe distinct spectral features in the absorption spectra of a substance at the THz frequencies, some long-range order is required. Since substances in the condensed phase are held together by either ionic, covalent or other electrostatic forces, the lower frequency modes in these materials will be associated with inter-molecular motions. Therefore, if the material has a crystalline structure, there will be phonon-like intermolecular modes at discrete frequency bands. On the other hand, for material with an amorphous structure, there will be a continuum of strongly damped intermolecular vibrational modes. This information is hard to extract at the higher frequencies where intra-molecular modes, as well as the electronic transitions, are involved. Also, due to the transparency of the THz

radiation in most of the clothing and packaging materials, there are several applications of THz-TDS in the detection of drugs and explosives.

In THz-TDS, an optical pulse is used to directly measure the electric field of the THz radiation. A typical THz pulse has sub-picosecond to a few picosecond time duration. Hence, a fast and sensitive detection technique is employed to capture its field. In this technique both the amplitude and the phase of the THz radiation are measured which provides more information than the conventional Fourier transform spectroscopy where only the amplitude of radiation is retrieved [11].

1.1.1 THz Generation Techniques

There are four common techniques for generating THz pulses based on ultra-short pulses from Ti:sapphire lasers or mode-locked fiber lasers. The first technique is based on the surface field emission effect where THz pulses can be generated using surface emitters [12]. In this technique, an ultra-short optical pulse illuminates a semiconductor material. If the wavelength of the ultra-short pulse is above the energy bandgap of the semiconductor material, the semiconductor absorbs the incident photons and creates electron-hole pairs at the surface region. The natural surface bias, also called Fermi level pinning, creates a band bending that has the effect of accelerating carriers of different signs in different directions, thereby creating a dipole. A transient photo-current will be generated from the dipole which is normally perpendicular to the surface. The rise time of this current is on the order of the laser pulse duration and its fall time is proportional to the transit time of the free carriers across the depletion zone. The photo-current can normally radiate a sub-picosecond electromagnetic pulse in the THz frequencies.

Short-pulse radiation at THz frequencies can also be generated in ambient air [13]. This can be achieved by focusing an intense laser beam into the air and was first reported in [14]. Higher intensity laser pulse at the focus creates ionized air (plasma), and the generation process is attributed to the ponderomotive force inside the plasma. Higher intensity THz radiation can also be achieved from laser-induced gas-plasma by focusing both the fundamental laser pulse and its second harmonic [13]. In this case, the THz wave emission is based on the four-wave mixing nonlinear optical process.

The next coherent radiation source of THz is based on optically pumped photoconductive antennas (PCA). PCA-based THz sources were first introduced and developed in [15, 16]. PCA is a DC-biased metal dipole antenna that is patterned on a photoconductive substrate. An optical pulse illuminates the antenna gap and propagates through the substrate. Once it gets absorbed in the photoconductive material, it produces a transient photocurrent which drives the dipole antenna and makes it emit a THz transient. The radiated THz transient has a duration on the order of picosecond depending on the carrier lifetime of the substrate [1]. However, there are fundamental limitations in the frequency response of the photoconductive-based techniques, due to their natural time constants for carrier dynamics.

THz generation based on the optical rectification as a second-order nonlinear process [17] is another technique that suggests the potential to generate THz radiation. The generated THz spectrum in the electro-optic crystal can be wideband, provided that the optical pump pulse is short enough, on the order of femtoseconds [18–20]. The bandwidth of the THz radiation in this technique can boost up to 40 THz and depends on the phase matching of the nonlinear process, phonon absorption of the crystal in THz frequencies,

the thickness of the crystal and, most importantly, the time duration of the pump laser pulse. The most common crystal materials to be used in this technique are <110> oriented GaAs, ZnTe, GaP, CdTe and InP. Generation of intense THz pulses with amplitudes exceeding $1\mathrm{MV/cm}$ has been reported in $LiNbO_3$ where its second-order nonlinear coefficient is 2-3 times larger than the nonlinear coefficient of the other commonly used crystals [21, 22]. This makes $LiNbO_3$ a good candidate to use in the THz-TDS to generate intense THz radiation with reasonably high bandwidth.

1.1.2 THz Detection Techniques

THz detection techniques use an ultra-short femtosecond laser pulse which is several times shorter than the THz electric field transient. In principle, the measurement of the unknown THz transient is performed by convolving it with the known ultra-short pulse in a sampling material. This obtains a trace of the time-domain THz electric field. Similar to the generation techniques, the detection is based on photoconductive sampling or electro-optic sampling [23, 24].

In the photoconductive sampling, a similar PCA to the generation antenna is used at the receiver. The generation and detection scheme is shown in Fig. 1.1. For the detection, there is no external DC bias. Instead, the THz beam focuses on the gap region of the PCA receiver, where it induces a transient bias voltage across the gap. At the same time, an ultra-short optical probe pulse copropagates with the THz beam into the photoconductive substrate where it generates photocarriers. The probe beam propagates through an adjustable optical delay line which allows for sweeping the optical delay line and convolving the photocarrier impulse signal with the THz field-induced transient voltage

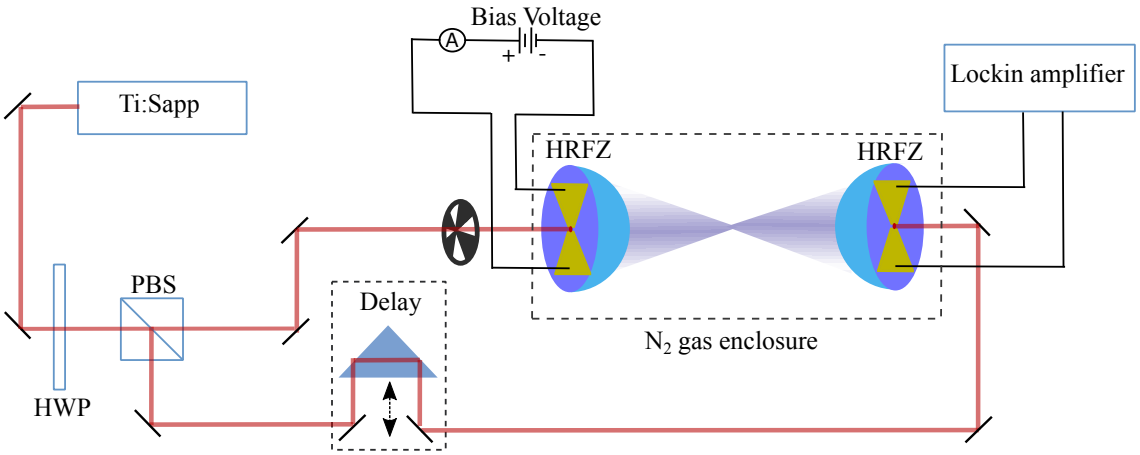

Figure 1.1: Collinear experimental setup diagram for THz generation and detection using PCA. Highly resistive float-zone (HRFZ) Silicon lens is used as the substrate of the antenna to focus and/or collect the THz beam. The THz part of the setup is enclosed and purged with dry nitrogen to prevent unwanted absorption from the water vapour in the room.

signal. This way, the temporal profile of the THz pulse can be measured by collecting and correlating the optical delay position and the induced photocurrent signal [1].

The second method of THz pulse detection is the electro-optic sampling technique which is based on the electro-optic (Pockels) effect. The material used to implement this technique can be the same material used for the optical rectification-based THz generation. Fig. 1.2 shows a typical collinear THz-TDS experimental setup where ZnTe is used to generate and detect the THz radiation. Using the quarter-wave plate, one can set the polarization state of the probe beam at the Wollaston prism to be circular in the absence of the THz beam. Once the THz beam transmits through the detection crystal, it induces a slight birefringence in the crystal. This birefringence then converts the purely circular state of polarization of the optical probe beam at the Wollaston prism into an elliptical state of polarization. The Wollaston prism then converts this asymmetry in the state of

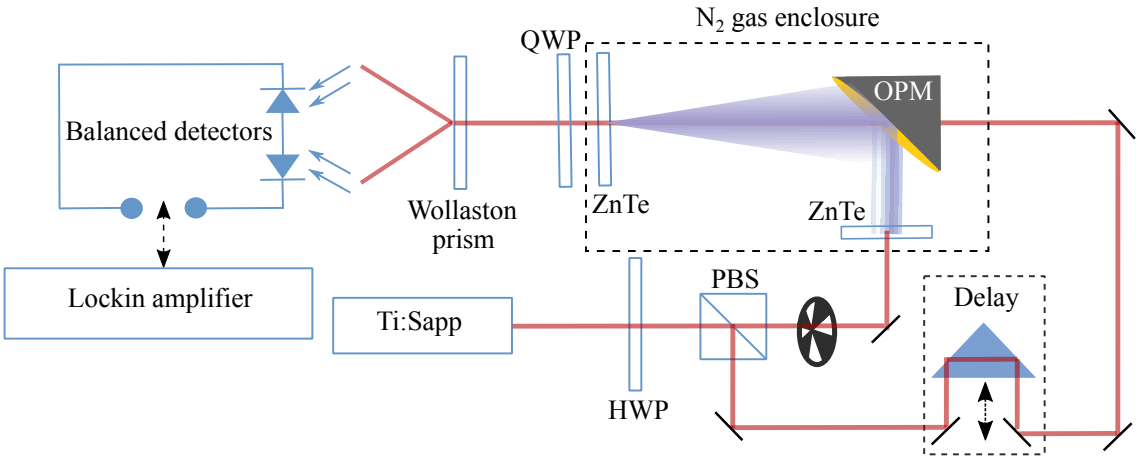

Figure 1.2: Collinear experimental setup diagram for THz generation and detection using ZnTe. Off-axis parabolic mirror is used to focus the THz beam in the detection crystal.

polarization to amplitude modulation. Similar to the Photoconductive based detection, a temporal profile of the THz field is obtained by convolving the probe pulse with the THz transient inside the crystal.

In this study, we use the electro-optic sampling technique to extract the pockels effect induced by the THz electric field on the nonlinear detection crystal. For the generation, we use the optical rectification in a $LiNbO_3$ (LN) crystal to generate THz radiation.

1.2 Nonlinear THz-TDS

Thanks to the recent developments in the terahertz (THz) coherent radiation sources, THz pulses with higher intensities are becoming routinely accessible [25–32]. These sources have enabled a range of nonlinear THz-TDS techniques where nonlinear light-matter interactions can be controlled by temporally trapping the generated field within a single-cycle pulse, and then by coherently releasing the high peak field into the matter. The

broadband coherent spectral content of these pulses is desirable in many imaging and spectroscopic applications [23, 33].

1.2.1 THz Nonlinear Optics

As the peak electric field of the THz signal exceeds hundreds of kV/cm, nonlinear optical interactions start to appear with the excitation of new fundamental modes such as the motion of free electrons, rotation of molecules and vibration of crystal lattices, etc. The dynamics of the nonlinear transport phenomena and nonlinear interaction of excitation modes can be studied, and the properties of condensed matter or chemical or biological systems can be controlled using these intense phase-stable transients [34, 35]. The underlying concept behind the electronic nonlinear effects is the ponderomotive energy. This energy is defined as the average kinetic energy of an electron that is trapped in an oscillating field. Since ponderomotive energy scales with the inverse square of the frequency, a THz laser with the same amount of intensity as for a visible laser source can make around 10^4 times more ponderomotive energy [36]. In THz frequencies, this energy can become much more than the bandgap energy of most semiconductor materials which enables many interesting nonlinear optical phenomena.

Also, in the THz frequencies, due to the longer time scales, it is possible to excite molecular vibration as the relaxation constant for most of the solids falls within the picosecond time range. We believe this lattice-based mechanism boosts the nonlinear interaction which results in a much larger nonlinear Kerr coefficient as compared to the electronic Kerr coefficient in the visible and near-infrared range.

1.2.2 THz Kerr effect

The refractive index of the optical materials depends on the intensity of the light used to measure the refractive index. This results in the well-known self-action effects in the time, spatial or spectral domain of the light, such as self-phase modulation, self-focusing, or self-broadening, respectively [17]. Intensity-dependent refractive index can be described using

$$n = n_0 + n_2 I, \tag{1.1}$$

where n_0 represents the weak-field refractive index, and I is the time-averaged intensity of the optical field. The parameter n_2, which is known as the Kerr coefficient describes the rate at which the refractive index increases with increasing optical intensity. This quantity is a material characteristic and determines the strength of the third-order nonlinear response of the material.

The mechanisms behind the nonlinear optical response of a transparent dielectric can be grouped into two main categories [17, 37, 38]: The mechanisms that work based on a change in the density of the substances (atoms, molecules, etc.) in the medium, and the mechanisms that are based on the nonlinear response of each substance. In this study, we focus on the second mechanism where in contrary to the first mechanism, it is characterized by the relaxation times shorter than a nanosecond. Hence, an intense THz pulse with a pico-second duration should excite a nonlinear polarization that arises from single-particle sources rather than a nonlinear polarization which roots in cumulative changes in the material density. Furthermore, this faster nonlinear polarization has different origins depending on the excitation pulse. In the visible and near-infrared regime of frequencies,

the dominant mechanism behind the nonlinear response is electronic whereas in the far-infrared and THz frequency range, it is expected to be mostly vibrational. In other words, the fast nonlinear response comes in the following form

$$n_2 = n_{2,e} + n_{2,v}, \tag{1.2}$$

where $n_{2,e}$ and $n_{2,v}$ are the electronic and vibrational contributions to the nonlinear refractive index. Moreover, it has been shown that the contribution of the Kerr coefficient in solids that is associated with anharmonic vibrations of the lattice in the crystalline materials at the THz frequencies can be up to several orders of magnitude larger than the Kerr coefficient in the visible and near-infrared regime ($n_{2,v} \gg n_{2,e}$) [38].

1.3 Existing Studies on the THz Nonlinear Optical Interactions

One of the earliest studies on the far-infrared nonlinear interactions was the observation of the ionization of high-lying Rydberg states in *Sodium* (Na) Rydberg atoms using half-cycle THz pulses (HCP) [39]. In this study, the authors apply an electric field parallel to the surface of a thin GaAs semiconductor wafer. Then, by illuminating one side of the wafer by 770 nm, 100 fs laser pulses, they make the semiconductor layer to conduct. Single-polarity HCPs are generated which are the spatially coherent radiation energy due to the rapidly accelerating electrons in the photoconductor. In their experiment, ground state Na atoms are excited to a Rydberg state using two tunable dye lasers, and then they focus

the generated THz pulses to ionize Rydberg atoms. Finally, a micro-channel plate (MCP) detector was used to collect the generated ions. They showed that there is a threshold field proportional to the binding energies of the Rydberg states at which ionization begins to appear.

Also, self-phase modulation (SPM) due to the nonlinear response of free electrons to the intense single-cycle THz pulse was reported at the THz frequencies [40]. In [40] the authors performed a nonlinear THz-TDS experiment in transmission configuration and reported on the observation of SPM and saturable absorption in an n-doped bulk semiconductor GaAs, resulting in a 200 fs group delay and 32% increase in transmission, respectively. Other THz-related works probing the nonlinear optical response at this frequency range have focused on THz-induced carrier multiplication via impact ionization [41–43] and THz saturable absorption and higher-harmonic generation by hot electrons [44–49]. For instance, the authors in [44] exposed an n-type bulk GaN semiconductor to high-field THz radiation and found coherent emission centered at 2 THz with picosecond decoherence time. They associated this emission with the impurity transitions in the semiconductor material. It is worth mentioning that, in contrary to the Drude theory of intra-band electron response that predicts a decay time of $\approx$ 150 fs, they observed a relatively long decoherence time. However, they justified their observations using a quantum mechanical discrete state model capable of describing the disordered impurity potential responsible for such behavior. In this context, the emitted THz field can be realized as a phase-coherent stimulated emission from impurities having a populated excited state and an unpopulated ground state (inversion). Also, [45] studied the nonlinear interaction of intense sub-cycle THz pulses with a doped semiconductor. They employ an inter-digitated large-aperture

photoconductive antenna (ILAPCA) by which they generate half-cycle THz pulses with duration up to 580 fs and the peak frequency around 0.2 THz. They use these pulses to perform nonlinear terahertz time-domain spectroscopy on an n-doped semiconductor $In_{0.57}Ga_{0.43}As$ thin film by varying the incident peak electric field and comparing the time and frequency domain electric field profiles. They observe a truncation of the half-cycle THz pulse and emission of high-frequency terahertz photons. They attribute this observation to the abrupt current drop caused by strong inter-valley scattering effects. They also use a thin-film transmission equation to model the sub-cycle nonlinear carrier dynamics.

Metamaterials have also been employed in [43] to enhance the THz peak fields to the MV/cm regime where a strong carrier generation across the bandgap of an un-doped GaAs semiconductor can be obtained. This strongly non-perturbative nonlinear regime would result in the generation of ultra-broadband near-infrared and visible inter-band luminescence, and a strong terahertz nonlinearity on the single-cycle time scale.

Another physical process that can contribute to the third-order nonlinear optical interactions in THz frequencies is molecular vibrations. Since the time scale of the THz pulse is on the order of the relaxation constants of molecular vibrations in most of the solids, a strong nonlinear polarization can be produced as a result of coherent oscillation of phonons excited by the THz pulse. Previous theoretical and experimental studies focusing on the THz frequency range have shown that by operating close to the vibrational lattice resonance, one can create a non-instantaneous nonlinear contribution to the Kerr effect in addition to the nearly instantaneous electronic response, which could result in an enhancement of the overall Kerr effect by several orders of magnitude [25, 38, 50, 51].

[50] presents a detailed discussion on the infrared dispersion of the third order nonlinear susceptibility ($\chi^{(3)}$) where a mixing of visible light beams in a transparent crystal occurs. For instance, they studied $\chi^{(3)}(-\omega_3, \omega_1, \omega_1, -\omega_2)$ in a cubic crystal where the frequencies ω_1, ω_2 and $\omega_3 = 2\omega_1 - \omega_2$ are in the transparent region of the crystal and they show a strong resonant behavior for the case $\omega_1 - \omega_2 = \omega_{\text{phonon}}$. They justify the $\chi^{(3)}$ behavior by considering the contributions from the properly retarded fields, created by distant nonlinear polarization sources proportional to the lower order nonlinear susceptibility $\chi^{(2)}$. In a different work [25], the authors study the polariton generation in $LiNbO_3$ (LN) crystal as a result of the excitation of strong vibrational modes using intense THz pulses. The idea is that since LN is ferro-electric, and can be switched between two different domain orientations, it shows significant anharmonicity associated with the double-well lattice potential and the barrier between the wells. They were able to observe nonlinear responses in THz which are originated from anharmonic lattice response of the LN crystal. They also look into polariton harmonic generation as well as self phase modulation by comparing the spectral power of the high intensity and low intensity THz pulses.

In a theoretical effort, [38] proposes a method for calculating the coefficient n_2 of crystals in the THz spectral range. The authors introduce a basic expression for the nonlinear coefficient n_2 of a crystal whose structural unit is considered to be a classical anharmonic oscillator with quadratic and cubic nonlinearities. Then, they can find the expression for the vibrational contribution to the coefficient n_2 in terms of known characteristics of the crystal by calculating the expressions for the linear refractive index and the coefficient of thermal expansion of the crystal. In this study, the authors show that for the pulses in the far infrared range, the dominant mechanism of Kerr nonlinearity is associated with

anharmonic vibrations of the lattice which can be studied by considering the dynamics of ions in the lattice resulting from the force induced by the electric field of the THz pulse. For the calculations, they consider an electronic response as well as a vibrational response in the total nonlinear polarization where they relate the vibrational contribution to the nonlinear refractive index and the thermal expansion coefficient of the crystal. Finally, they obtain a nonlinear refractive coefficient of $n_2 = 4.42 \times 10^{-16}$ m^2/W for the crystalline quartz which is around 1000 times higher than the nonlinear refractive index in the visible range.

The theoretical study reported in [38] leads to a good understanding of the physics of light-matter interactions at the THz frequencies and brings about potential applications to the emerging THz technology. However, an experimental work aiming at the measurement of the nonlinear optical characteristics of different dielectric materials is missing. To the best of our knowledge, there is no experimental study of the nonlinear optical response of various materials that yields measured values of the Kerr coefficient as well as its dispersion behavior at the THz frequencies.

In this thesis, we investigate the nonlinear optical response of various materials by including various solids and water vapour. We build a THz-TDS experimental setup where we measure the nonlinear phase-shift acquired by the transmitted THz pulse as it propagates through the material under study. This way, we find the value of the Kerr coefficient of the material as a function of frequency. We also perform numerical modeling to simulate the propagation of a THz pulse inside a nonlinear optical material and to study its nonlinear dynamics. In our model, we consider two different relaxation times (fast and slow) for the nonlinear polarization term by which we determine the contribution of the slow

nonlinear response in the overall Kerr effect, including both nearly instantaneous and non-instantaneous processes. Finally, we carry out high-resolution THz-TDS measurements in water vapour and find a large nonlinear response at the location of its several sharp resonances in the THz frequency range from 1 to 1.5 THz. Our results can help the THz spectroscopy scientists to compensate for the strong nonlinear response of the water vapour when analyzing their measurement data. Also, this work represents a significant contribution to a better understanding of water vapour molecular structure, as well as their interactions with THz radiation.

1.4 Thesis Layout

The introductory chapter (Chapter 1) starts with the background of this work along with motivation and some fundamentals of THz spectroscopy and nonlinear optics. In Chapter 2, we present the details of our experimental approach to building an intense THz generation and detection setup. This experimental setup allows for performing our nonlinear THz-TDS measurements.

Also, since it is still not clear what the share of the delayed response in the strength of the overall Kerr effect is, we explore the characteristic time scales for different contributions to the overall Kerr effect during the nonlinear optical interactions at the THz frequencies. We do so, for the first time, by adopting a model taking into account both contributions of the Kerr effect corresponding to a nearly instantaneous and retarded third-order nonlinear responses. This is the topic of Chapter 3. The model that we use is similar to the conventional model for the Raman effect in silica fibers [52]. Since

lattice-driven nonlinearities are slower than the electronic responses, they are modeled in a similar manner to the stimulated Raman scattering (SRS) in silica fiber where there is a long interaction length with optical pulses resulting in important changes in the optical spectrum observed at the fiber output.

In Chapter 4, we focus on the nonlinear optical response of water vapour at the THz frequencies. Unlike solids and liquids, gaseous materials such as water vapour can have sharp resonances due to the vibrational-rotational transitions in the THz range, and the nonlinear response of these transitions have not been studied to date. We make an effort to extend its optical response from linear to the nonlinear regime. We also quantify its nonlinear response by estimating its nonlinear Kerr coefficient.

Chapter 5 presents the experimental results on the measurement of the nonlinear refractive index n_2 for different solids including crystalline and amorphous crystals. We show how phonon contribution can affect the measurement results by introducing a time delay to the propagating THz electric field.

Finally, Chapter 6 provides a summary and conclusion.

2. Intense THz Generation

Building a source of intense THz pulse is the first step toward realizing the nonlinear optical measurements at THz frequencies. Among the different methods to generate intense THz pulses, optical rectification in $LiNbO_3$ is one of the most efficient techniques. This crystal provides a high effective electro-optic coefficient that leads to a relatively high near-infrared pump to THz conversion.

This chapter provides the theoretical details and some of the important design considerations to build an intense THz pulse generation and detection setup, followed by discussing the experimental setup and the initial results. We present the generation part of the setup in sections 1.1 through 1.3. Section 1.4 focuses on the detection technique used to detect the THz electric field transient. Finally, section 1.5 presents the experimental setup and discusses some of the optimization techniques that we use to fully utilize it.

2.1 THz Generation Using Optical Rectification

Most THz generation techniques are based on optical rectification in organic / non-organic nonlinear crystals, laser-driven ion acceleration, or emission by gas ionization [26–28, 53,

54]. Different generation techniques based on nonlinear optical processes yield intense, single-cycle THz pulses with the peak electric fields from a few kV/cm up to hundreds of MV/cm [55, 56]. Optical rectification of ultra-short optical pulses due to the frequency difference of different spectral components within the spectrum of the laser pulse will result in the spectral generation around 1 THz. A review on different material candidates suitable for optical rectification is given in [57], where a figure of merit (FOM) is defined, and different materials with different figures of merits are compared. We start off by redefining the figure of merit using the formula given in [58] for the efficiency of difference-frequency generation (DFG) process by long plane-wave pulses in the absence of pump depletion. This equation,

$$\eta_{\mathrm{THz}} = \frac{2\,\omega^2\, d_{\mathrm{eff}}^2 L^2 I}{\varepsilon_0\, n_{\mathrm{NIR}}^2\, n_{\mathrm{THz}}\, c^3}\, \exp\left(-\alpha_{\mathrm{THz}}\, L/2\right) \frac{\sinh^2\left[\alpha_{\mathrm{THz}}\,(L/4)\right]}{\left[\alpha_{\mathrm{THz}}\,(L/4)\right]^2}, \tag{2.1}$$

can be used to describe the DFG efficiency under the phase matching condition, and includes the effect of THz absorption during propagation in the nonlinear crystal. In this equation, ω is the angular difference frequency, which is in the THz range, L is the length of the nonlinear crystal, I is the intensity of the near-infrared (NIR) light, ε_0 is the vacuum permittivity, and n_{NIR} and n_{THz} are the refractive indices at the near-infrared and the THz frequencies, respectively. Also, α_{THz} is the absorption coefficient at the THz frequencies. The effective nonlinear coefficient is shown by d_{eff}. This parameter is proportional to the electro-optic coefficient of the material (r) and is given by [59]

$$d_{\mathrm{eff}} = -n_{\mathrm{NIR}}^4\, r/4. \tag{2.2}$$

We can re-evaluate the DFG efficiency (η_{THz}) under the two opposite limits of very strong ($\alpha_{\mathrm{THz}}\, L \gg 1$) and very weak ($\alpha_{\mathrm{THz}}\, L \ll 1$) absorption regimes. This way we get simpler forms of η_{THz} based on absorption of the material. In the limit of very weak absorption, one finds the DFG efficiency as

$$\eta_{\mathrm{THz}} = \frac{2\,\omega^2\, d_{\mathrm{eff}}^2\, L^2\, I}{\varepsilon_0\, n_{\mathrm{NIR}}^2\, n_{\mathrm{THz}}\, c^3}. \tag{2.3}$$

On the other hand, η_{THz} for the material with strong absorption will have the form:

$$\eta_{\mathrm{THz}} = \frac{8\,\omega^2\, d_{\mathrm{eff}}^2\, I}{\varepsilon_0\, n_{\mathrm{NIR}}^2\, n_{\mathrm{THz}}\, \alpha_{\mathrm{THz}}^2\, c^3}. \tag{2.4}$$

Based on the formula derived for the efficiency of the nonlinear process in the electro-optic crystal, we are able to define a FOM for the two different limits of material absorption. For the material with negligible absorption, we have

$$\mathrm{FOM}_{\mathrm{NA}} = \frac{d_{\mathrm{eff}}^2 L^2}{n_{\mathrm{NIR}}^2\, n_{\mathrm{THz}}}. \tag{2.5}$$

We notice that FOM of the weakly absorbing material is directly proportional to the square of the length of the nonlinear crystal. However, for the absorptive material, it is inversely proportional to the square of the absorption coefficient. Hence we obtain

$$\mathrm{FOM}_{\mathrm{A}} = \frac{4\, d_{\mathrm{eff}}^2}{n_{\mathrm{NIR}}^2\, n_{\mathrm{THz}}\, \alpha_{\mathrm{THz}}^2}. \tag{2.6}$$

It is worth pointing out that, depending on the relative values of the absorption of the material and its length, we will decide which FOM to use to evaluate that material.

Table 2.1 compares some of the different parameters involved in the THz generation process in some nonlinear optical materials.

Material	d_{eff} (pm/V)	n^{gr}_{800nm}	n_{THz}	α_{THz} (cm^{-1})	FOM ($\text{pm}^2\text{cm}^2/\text{V}^2$)
CdTe	81.8	–	3.24	4.8	11.0
GaAs	65.6	4.18	3.59	0.5	4.21
GaP	44.8	3.67	3.34	0.2	0.72
ZnTe	68.5	3.13	3.17	1.3	7.27
GaSe	28.0	3.13	3.27	0.5	1.18
$sLiNbO_3$	168	2.25	4.96	17	18.2
$sLiNbO_3$ 100K	–	–	–	4.8	48.6

Table 2.1: Optical properties of some nonlinear crystals suitable for optical rectification. Data is taken from [57]. THz refractive index and absorption coefficient values are shown at 1 THz. $n^{gr}_{800\,\text{nm}}$ is the group index of the material medium at 800 nm.

It can be seen from Table 2.1 that stochastic lithium niobate ($sLiNbO_3$) offers the highest effective electro-optic coefficient (d_{eff}) among the different material candidates. However, refractive index of this crystal in the near-infrared (NIR) and THz differs the most, which brings the difficulty of achieving a collinear phase matching. For the most of other material candidates, the refractive indices at the NIR and THz do not show much of the difference. This facilitates the phase matching condition of the DFG through a collinear phase matching process. For instance, although ZnTe has the forth largest FOM, it is known to be the most commonly used electro-optic crystal for optical rectification and electro-optic sampling. The reason is that a collinear scheme can approximately fulfill the phase matching condition due to the similarity of the refractive index of this material at NIR and THz that are 3.13 and 3.17, respectively.

To overcome the phase matching problem with the $sLiNbO_3$, a non-collinear phase matching technique is proposed [60]. This technique is called velocity matching by pulse front tilting, and will be discussed in the next sections. Also, it is a regular practice, to dope 3% MgO into the $LiNbO_3$ crystal to suppress its photorefraction and to increase its damage threshold (Hence called $sLiNbO_3$). This way, it withstands pulses of higher peak powers and can generate more THz radiation, without being damaged. Material candidates are not limited to the cases shown in Table 2.1. It has recently been shown that the organic crystal DAST can also be used to generate and detect THz radiation [61]. This material can have larger electro-optic coefficient and better FOM than $sLiNbO_3$, depending on the excitation wavelength. But this material has a strong absorpton at 1 THz. Hence, it is a good material candidate for generation of THz radiation beyond 1.5 THz.

2.2 Phase matching condition

An efficient nonlinear conversion process requires the phase matching condition to be fulfilled i.e. the generated THz wave should maintain a fixed phase relation with respect to the induced nonlinear polarization. In the case of difference frequency generation for THz generation, by fulfilling the phase matching condition, the generated THz radiation oscillates in phase with the excitation pulse for up to a certain length in crystal. This constructive build up of the newly generated THz frequency components guarantees an efficient NIR to THz conversion. Phase matching can be implemented collinearly or non-collinearly. For the case of collinear phase matching, one needs to force the wavevector of the NIR pump beam to match that of the generated THz beam in the crystal, so that the

generated THz frequencies sum up coherently, and contribute to the THz spectrum. In other words,

$$\Delta k = k_{\omega_{\mathrm{NIR}}+\omega_{\mathrm{THz}}} - k_{\omega_{\mathrm{NIR}}} - k_{\omega_{\mathrm{THz}}} = 0, \tag{2.7}$$

where k is the wavevector of the corresponding frequency. In order to get the phase matching condition for the specific case of THz generation in $LiNbO_3$, we re-write Eq. (2.7) as follows:

$$k_{\omega_{\mathrm{NIR}}+\omega_{\mathrm{THz}}} - k_{\omega_{\mathrm{NIR}}} = k_{\omega_{\mathrm{THz}}}. \tag{2.8}$$

Dividing the above equation by the THz angular frequency (ω_{THz}), one gets:

$$\frac{k_{\omega_{\mathrm{NIR}}+\omega_{\mathrm{THz}}} - k_{\omega_{\mathrm{NIR}}}}{\omega_{\mathrm{THz}}} = \frac{k_{\omega_{\mathrm{THz}}}}{\omega_{\mathrm{THz}}}. \tag{2.9}$$

The left-hand side of this equation is the definition of the derivative when ω_{THz} is relatively small. So, we have [19]:

$$\frac{\partial k_{\omega_{\mathrm{NIR}}}}{\partial \omega_{\mathrm{NIR}}} = \frac{k_{\omega_{\mathrm{THz}}}}{\omega_{\mathrm{THz}}}. \tag{2.10}$$

This equation shows that in order to have a phase-matching condition fulfilled, we need to have the group velocity of the NIR pulse equal to the phase velocity of the THz radiation inside the crystal. Since the refractive indices of NIR and THz are pretty close in most of the nonlinear crystals (see Table 2.1), one is able to do collinear phase matching to satisfy Eq. (2.7). The assumption behind this condition is that ω_{THz} should be arbitrarily small. In this case, we know that comparing to ω_{NIR}, ω_{THz} is more than two orders of magnitude smaller. Hence, the assumption is valid. It also explains why this approximation cannot be made when dealing with most of other cases like sum frequency generation. Anyway,

for the $LiNbO_3$, where the collinear phase matching does not work, one solution is to use tilted-pulse-front technique [62] in the crystal to phase-match the near-infrared beam and the THz radiation that takes the form of emission in a Cherenkov cone.

2.3 Tilted-pulse-front technique

In this technique, the intensity fronts of the pump beam are tilted in such a way that they coincide with the phase fronts of the generated THz beam inside the generation crystal. Phase matching condition in this case is satisfied by combining Eq. (2.7) and Eq. (2.10) to get the following:

$$\Delta k = k_{\omega_{\mathrm{THz}}} - \omega_{\mathrm{THz}} \frac{\partial k_{\omega_{\mathrm{NIR}}}}{\partial \omega_{\mathrm{NIR}}} = 0. \tag{2.11}$$

In this equation, if we write the wavevectors in terms of the refractive indices, we will have

$$\Delta k = \omega_{\mathrm{THz}} \frac{n(\omega_{\mathrm{THz}})}{c_0} - \omega_{\mathrm{THz}} \frac{\partial}{\partial \omega_{\mathrm{NIR}}} \left[\omega_{\mathrm{NIR}} \frac{n^{gr}(\omega_{\mathrm{NIR}})}{c_0} \right] = \frac{\omega_{\mathrm{THz}}}{c_0} \left[n(\omega_{\mathrm{THz}}) - n^{gr}(\omega_{\mathrm{NIR}}) \right]. \tag{2.12}$$

To get the matched condition, we need to have $\Delta k = 0$, which requires $n(\omega_{\mathrm{THz}}) = n^{gr}(\omega_{\mathrm{NIR}})$, and it is obviously not the case. Here is where tilted-pulse-front technique comes into play to satisfy the condition $\Delta k = 0$ by applying a correction factor $1/\cos\gamma$ to the group index of the NIR beam. This way, one is able to fulfill the phase matching condition by appropriate choice of the angle γ. Thus, the modified version of Eq. (2.12)

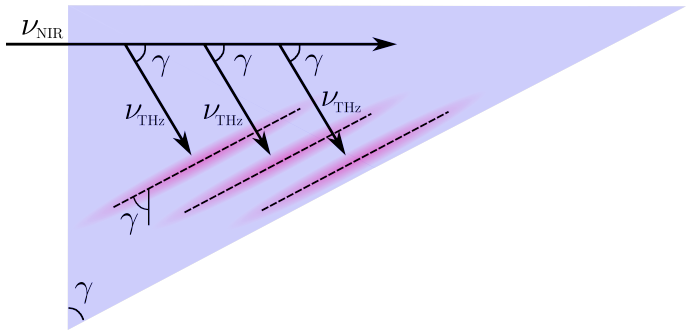

Figure 2.1: Illustration of velocity matching in $LiNbO_3$ (blue wedge) using tilted-pulse-front technique. The tilted intensity fronts of the NIR pump beam (dashed lines) generate the polaritonic THz waves in the crystal (pink waves). In order for the NIR to THz conversion to work efficiently, one has to have: $v_{NIR}\cos\gamma = v_{THz}$.

will be in the form

$$\Delta k = \frac{\omega_{THz}}{c_0}\left[n(\omega_{THz}) - \frac{n^{gr}(\omega_{NIR})}{\cos\gamma}\right]. \tag{2.13}$$

The procedure for Tilted-pulse-front technique is schematically shown in Fig. 2.1. This technique is based on Huygens–Fresnel principle [63]. By tilting the intensity front of the NIR beam, the THz radiation that is excited by this pulse front, propagates perpendicularly to its front with a velocity v_{THz}. Therefore, it creates an angle γ between the NIR and THz radiation, and thereby comes the correction factor in the phase matching condition given by Eq. (2.13).

The next step in the design procedure is to find the appropriate angle γ. The angle γ (also defined in Fig. 2.1) can be found from the equation

$$\gamma = \cos^{-1}\frac{v_{THz}}{v_{NIR}} = \cos^{-1}\frac{n^{gr}(\omega_{NIR})}{n(\omega_{THz})}. \tag{2.14}$$

Assuming the THz central frequency to be at 1 THz, and the near-infrared pump wavelength

which is at 790 nm, one can find the respective refractive index values to be $n^{gr}(\lambda_0 = 790\,nm) = 2.267$ and $n(\omega = 2\pi \times 1\,\mathrm{THz}) = 4.962$ [64]. Now, we can use Eq. (2.14) to find the value of this angle to be $\gamma \approx 63^\circ$. So, we need to tilt the intensity fronts of the NIR beam by 63 degrees to fulfil the matching condition. Note that the $LiNbO_3$ wedge is also cut at exactly 63° to maximize the NIR to THz conversion efficiency.

We use two cylindrical lenses and a diffraction grating to introduce the required amount of tilt to the pump fronts. Fig. 2.2 (a) shows the tilting scheme where the pump beam first diffracts from the grating. We calculate the amount of tilt acquired by the pump as it diffracts from the grating using a simple path (ray) diagram. As shown in Fig. 2.2 (b), in order not to disturb the phase of the incident beam after diffraction, the diffracted ray (blue line) travels some integer multiple of wavelengths (λ) more than the incident beam (violet line). We thus have $x + y = m\lambda$, where m is the order of diffraction and λ is the wavelength of light. This way, although diffracted front is tilted, both the incident and diffracted fronts are still in-phase. It can also be seen from this figure that $z = 1/g \cos\theta_d$, where g is the groove density of the grating and θ_d is the diffraction angle of the pump beam. Therefore, the tilt angle γ' is

$$\gamma' = \tan^{-1}\frac{x+y}{z} = \tan^{-1}\frac{g\,m\,\lambda}{\cos\theta_d}. \tag{2.15}$$

The angle γ' is the tilt angle of the beam right after the grating. We can now find the tilt angle of the pump after it transmits through the lenses inside the generation crystal (γ). This can be done by introducing the magnification factor of the lens system and refractive

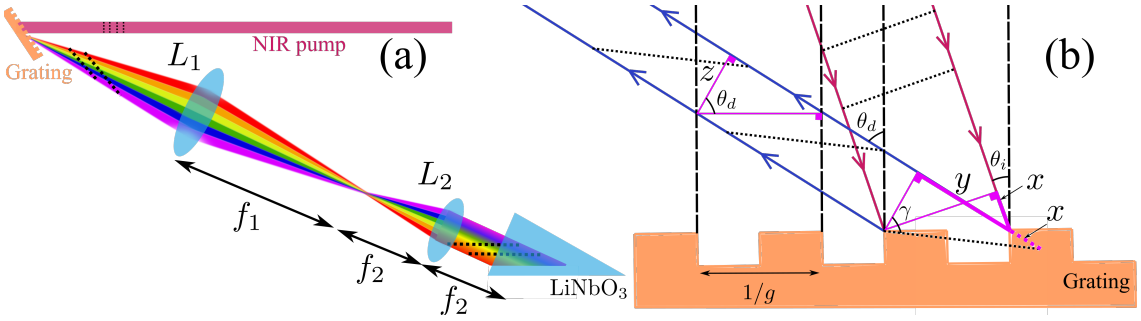

Figure 2.2: (a) Pulse-front tilting scheme. The dotted lines on the beams show the intensity fronts. (b) Ray optics calculation of the tilt. the groove density of the grating is 1800 mm^{-1}. The dimensions shown in this figure are not in scale.

index of the crystal as follows:

$$\gamma = \tan^{-1} \frac{m \lambda_0 g}{n_0^{gr} h_1 \cos \theta_d}. \tag{2.16}$$

Here, h_1 is the horizontal magnification factor of the pump pulse front introduced by the lens system. The wavelength λ_0 is the central pump wavelength, and n_0^{gr} is the group index of the crystal at λ_0.

From an experimental point of view, one wants the image of the grating inside the optical crystal in a way that it coincides with the tilted pulse front at the angle γ. In other words, maximum THz conversion efficiency is achieved if the angle of the grating image inside the crystal is equal to the tilt angle of the pulse front. The image of the grating inside the generation crystal through a lens pair with the magnification h_2 is described by [65]

$$\theta = \tan^{-1} n_0^{gr} h_2 \tan \theta_d, \tag{2.17}$$

where θ is angle of the grating inside the crystal. We want this angle to be equal to the tilt

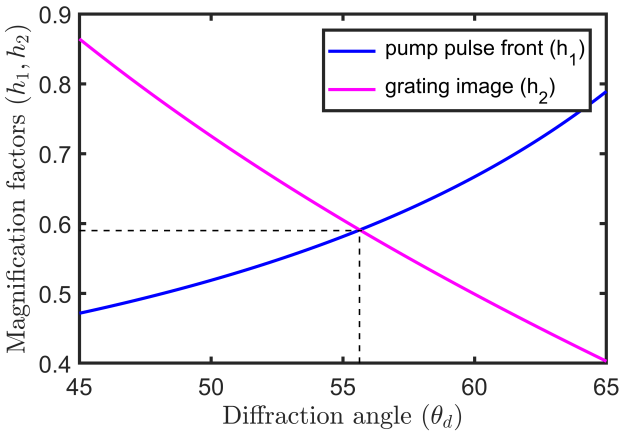

Figure 2.3: Calculated magnification factors of the lens pair as a function of diffraction angle of the grating. The magnification factor for the tilted pulse front (h_1) is equal to the magnification factor for the grating image inside the crystal (h_2) which determines the diffraction angle. This allows one to determine the angle of the diffraction grating in front of the pump beam.

angle ($\theta = \gamma$). By comparing the horizontal magnifications (h_1 and h_2) in both equations (2.16) and (2.17), and setting them equal to each other, one obtains the diffraction angle of the beam at the grating. This can be done by plotting both sides of the following equation

$$\frac{m\lambda_0 g}{\tan\gamma\, n_0^{gr}\cos\theta_d} = \frac{\tan\gamma}{n_0^{gr}\tan\theta_d}. \tag{2.18}$$

We let the first-order diffraction beam ($m = 1$) enter the generation crystal by spatially filtering out the higher diffraction orders. We calculate both the magnification factors as a function of diffraction angle. A plot of both sides of Eq. (2.18) is shown in Fig. 2.3 where a grating with a groove density of 1800 mm^{-1} is used, followed by a pair of lenses with a magnification factor of $h = 0.56$. Based on the results shown in Fig. 2.3, the diffraction angle is found to be $\theta_d = 55.7°$, where the magnification factor for the tilted pulse front

(h_1) is equal to the magnification factor for the grating image inside the crystal (h_2) at $h_1 = h_2 = 0.58$. We implement this magnification factor by choosing two cylindrical lenses of $f_1 = 13$ cm and $f_2 = 7$ cm. Also, we can find the incidence angle using the grating equation

$$\theta_i = \sin^{-1}(g\lambda - \sin\theta_d). \tag{2.19}$$

The final design criterion related to the part of the setup shown in Fig. 2.2 is the location of the image of the grating inside the LN crystal. We want the grating to be imaged close to the output face of the generation crystal within the coherence length of the nonlinear process. Coherence length ($L_c = 2\pi/|\Delta k|$) is the length in the crystal where the generated THz frequencies add up coherently and contribute to the THz spectrum. It also provides an estimation of the radiation frequency range that falls into the phase matching condition, and thus can be generated efficiently. It is defined as [19]

$$L_c(\omega_{\mathrm{THz}}) = \frac{2\pi c_0}{\omega_{\mathrm{THz}}\left[n(\omega_{\mathrm{THz}}) - \frac{n^{gr}(\omega_{\mathrm{NIR}})}{\cos\gamma}\right]}. \tag{2.20}$$

In order to find the value of the coherence length in our case, we need to have the value of the angle γ, as well as the refractive index values that we obtained before. Fig. 2.4 shows the coherence length of the nonlinear process in the $LiNbO_3$ used in our setup as a function of the generation frequency.

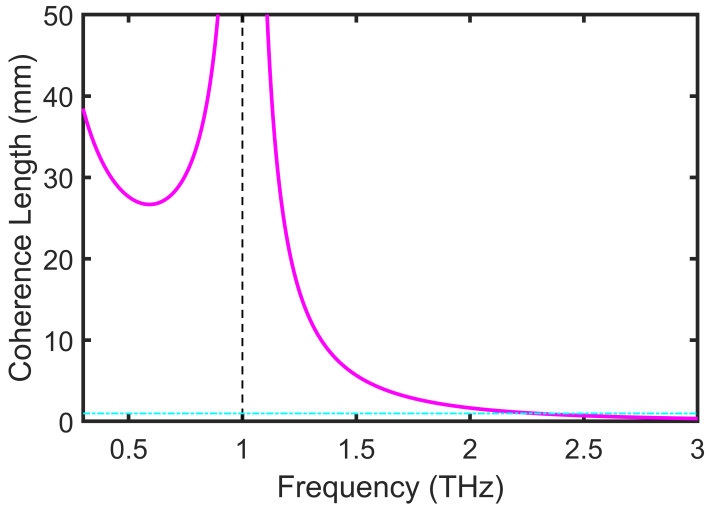

Figure 2.4: The calculated coherence length of the optical rectification process in the LN crystal. Coherence length falls below 1 mm for the frequencies less than 2.3 THz, which shows that the bandwidth of the process cuts off around this frequency. One needs to get the image of the grating within 1 mm spacing from the output facet of the crystal to maximize the generation bandwidth.

2.4 THz Detection using Electro-optic Sampling

In the detection arm, we use (110) ZnTe, which is an electro-optic (EO) crystal with zincblende structure to detect the THz field transient. We let both the THz beam and a near-infrared probe pulse overlap at the focus position into a thin ZnTe. THz detection based on Electro-optic sampling is schematically shown in Fig. 2.5. In the absence of a THz electric field, the quarter-wave plate (QWP) converts the linear polarization of the probe beam into circular polarization. When the THz beam co-propagates with the probe beam, its field modifies the optical refractive index of the probe pulse by the linear EO (Pockels) effect, thereby inducing an ellipticity to the probe's polarization. Using a delay line, we measure this ellipticity as a function of time delay with respect to the THz pulse

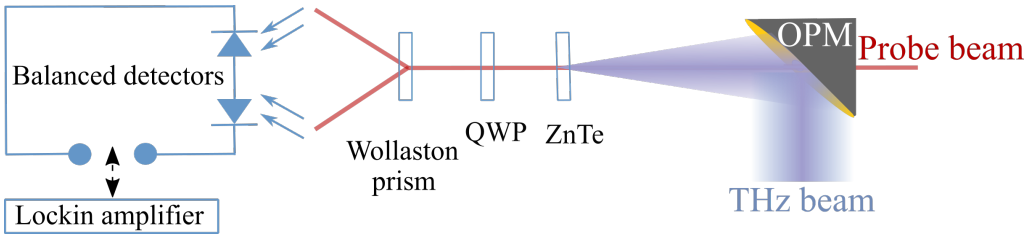

Figure 2.5: THz detection based on EO sampling. The off-axis parabolic mirror (OPM) has a small hole at its center to allow for the probe beam transmission so that both the THz and the probe pulses can copropagate inside the detection crystal.

in order to determine the time dependence of the THz field. A Wollaston prism along with a pair of balanced photodetectors and a lock-in amplifier allow for a linear detection of the induced birefringence at the chopping frequency of the probe.

Since in this study we are using ZnTe for detection, we will discuss the angular dependence of the detected field in a more detailed way. However, before we move to the detection, we briefly mention the THz generation mechanism in an EO material. The EO coefficient γ_{14} is related to the nonlinear second-order susceptibility coefficient d_{14} by

$$d_{14} = -\frac{\varepsilon_0^2}{4\pi}\,\gamma_{14} \tag{2.21}$$

The strength of the EO signal depends on the relative orientation of the crystal and the electric field of the THz, as well as the probe beam. This is true for both the generation and detection of the THz pulse. It is shown that if ZnTe is used to generate THz field, the angular dependence of the generated THz field is described by [29]

$$|E_{\mathrm{THz}}| = d_{14}E_0^2\left[\sin^2(2\theta)+\sin^4(\theta)\right]^{\frac{1}{2}}. \tag{2.22}$$

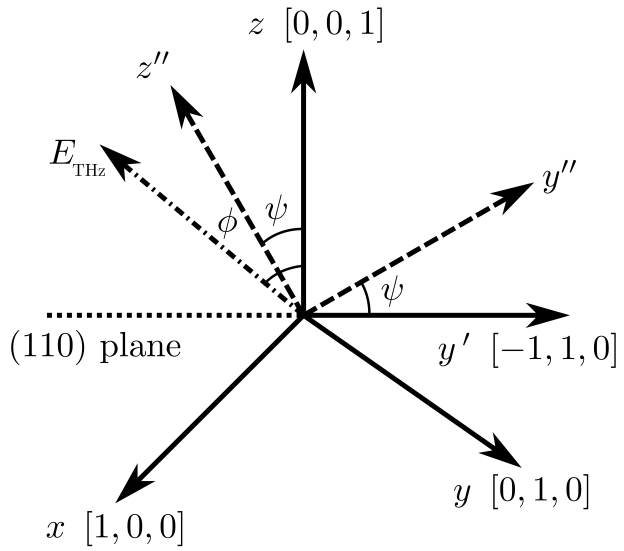

Figure 2.6: Angle of the THz polarization direction with respect to the z-axis in the (110) ZnTe geometry. The plane of the page is the (110) plane of the crystal.

In this equation, θ is the angle between the z-axis ([001] direction in Fig. 2.6) of the (110) ZnTe crystal and the polarization direction of the incident pump field. Also, E_0 is the magnitude of the optical field vector.

For the detection, we are looking for the dependence of the EO sampling signal on the angle ϕ. Let us assume that x, y and z are the crystallographic axes shown in Fig. 2.6 as $[1,0,0] \rightarrow x$, $[0,1,0] \rightarrow y$ and $[0,0,1] \rightarrow z$, respectively. The (110) cut is on the plane of the page. Also, ϕ is the angle between the THz electric field and z-axis. The birefringence in the crystal can be described using an index ellipsoid as [66]

$$\frac{x^2}{n_x^2} + \frac{y^2}{n_y^2} + \frac{z^2}{n_z^2} = 1. \tag{2.23}$$

When an arbitrary electric field $\mathbf{E} = (E_x, E_y, E_z)$ is applied to a zincblende crystal, the index ellipsoid will be described by [66, 67]

$$\frac{x^2+y^2+z^2}{n_0^2} + 2r_{41}\left(E_x yz + E_y zx + E_z xy\right) = 1. \tag{2.24}$$

Here, r_{41} is the EO coefficient of the crystal. THz field is normally incident upon the (110) EO crystal (see Fig. 2.6). Therefore, different components of its electric field can be written as

$$\mathbf{E} = E_{\mathrm{THz}}\left(\sin\phi/\sqrt{2}, -\sin\phi/\sqrt{2}, \cos\phi\right). \tag{2.25}$$

Substituting Eq. (2.25) into Eq. (2.24), we can write the equation for the index ellipsoid as

$$\frac{x^2+y^2+z^2}{n_0^2} + \frac{2r_{41}E_{\mathrm{THz}}\sin\phi}{\sqrt{2}}yz - \frac{2r_{41}E_{\mathrm{THz}}\sin\phi}{\sqrt{2}}zx + 2\,r_{41}\,E_{\mathrm{THz}}\cos\phi\,xy = 1. \tag{2.26}$$

Now, it is more convenient to construct a lab coordinate, $x'y'z'$, so that $x'y'$ is on the (110) plane as shown in Fig. 2.6. This new lab coordinate is built by rotating the xyz system around the z-axis by 45°. The new coordinate $x'y'z'$ is related to the xyz system using the rotation matrix as follows:

$$\begin{bmatrix} x' \\ y' \\ z' \end{bmatrix} = \begin{bmatrix} 1/\sqrt{2} & 1/\sqrt{2} & 0 \\ -1/\sqrt{2} & 1/\sqrt{2} & 0 \\ 0 & 0 & 1 \end{bmatrix} \begin{bmatrix} x \\ y \\ z \end{bmatrix}. \tag{2.27}$$

Using this transformation we can express Eq. (2.26) in the new $x'y'z'$ system. Moreover,

we can set $x^{'} = 0$, to get the equation for the index ellipsoid on the (110) plane ($y^{'}z^{'}$ plane) [66, 67]:

$$\left(\frac{1}{n_0^2} - r_{41}\,E_{THz}\cos\phi\right) y'^2 + \frac{z'^2}{n_0^2} + 2\,r_{41}\,E_{THz}\sin\phi\,y'z' = 1. \tag{2.28}$$

The ellipse equation on (110) plane provides the two principal indices of refraction of the ellipse as a function of ϕ. The refractive index along the y'' axis shown in Fig. 2.6 will be

$$n_{y''} \approx n_0 + \frac{n_0^3\,r_{41}\,E_{THz}}{4}\left(\cos\phi - \sqrt{1+3\sin^2\phi}\right). \tag{2.29}$$

Also, the refractive index along the z'' axis is [67, 68]

$$n_{z''} \approx n_0 + \frac{n_0^3\,r_{41}\,E_{THz}}{4}\left(\cos\phi + \sqrt{1+3\sin^2\phi}\right). \tag{2.30}$$

In the THz EO sampling, the signal level depends on the phase retardation, which itself is directly proportional to $\Delta n = n_{y''} - n_{z''}$. After substituting the expressions for the refractive indices along y'' and z'' axis, we have

$$\Delta n = \frac{n_0^3\,r_{41}\,E_{\mathrm{THz}}}{2}\sqrt{1+3\sin^2\phi}. \tag{2.31}$$

Knowing the refractive index difference along the principal axes of the index ellipsoid, we can calculate the amount of phase retardation. Phase retardation is the phase difference between the two field polarization components (y'' and z'') of the probe-laser field as it propagates through the detection crystal. The bigger this phase retardation, the more responsive the EO material is, and the EO signal is stronger. Initially, the probe field is set

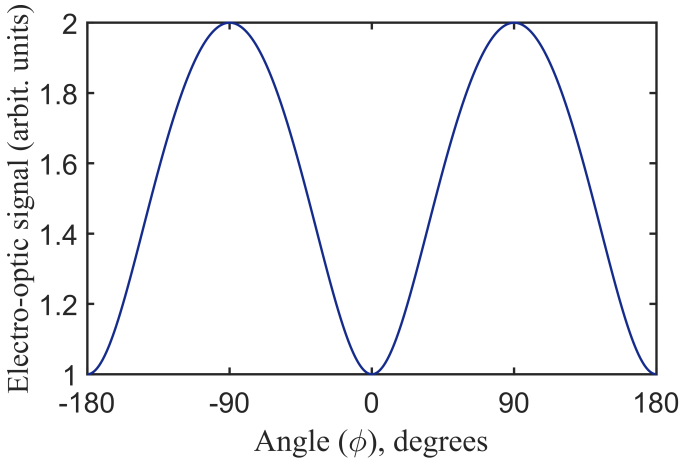

Figure 2.7: Angular dependence of the EO signal for THz detection.

to be circularly polarized but as it transmits through the detection crystal, its field becomes elliptically polarized. The phase retardation is therefore

$$\chi = \frac{2\pi L}{\lambda}\Delta n, \tag{2.32}$$

where L is the thickness of the crystal. Combining Eqs. (2.31) and (2.32), we can find the angle ϕ dependence of the sampling signal intensity, which is proportional to the phase retardation

$$I_{\text{sampling}} \propto \frac{E_{\text{THz}}\sqrt{1+3\sin^2(\phi)}}{2}. \tag{2.33}$$

We plot the angular dependence of the EO signal (I_{sampling}) in Fig. 2.7. The optimum signal intensity is achieved once the angle between the THz polarization and the crystal z-axis is $\pm 90^\circ$. Having a strong EO signal is quite important in obtaining measurements with high signal-to-noise ratio (SNR). This can be achieved in the experiment by adjusting the angle between the z-axis of the detection crystal mounted on a rotation mount and the

THz polarization direction, so that the EO signal is optimal as given in Fig. 2.7.

The other important criteria is the electric field evaluation to convert the voltage values of the raw data to the actual electric field values in units of volts per meter (V/m). Let's assume the EO signal is optimized by setting $\phi = 90^\circ$. In this case, the phase retardation is

$$\chi = \frac{2\pi L}{\lambda} n_0^3 r_{41} E_{\mathrm{THz}}. \tag{2.34}$$

The peak of the electric field at the detection crystal (E_{THz}) is calculated by relating the modulation of the balanced photodetectors (Fig. 2.5) to the phase retardation as [29]

$$\frac{A-B}{A+B} = \chi = \frac{2\pi L}{\lambda} n_0^3 r_{41} E_{\mathrm{THz}}. \tag{2.35}$$

In our experiment, $n_0 = 2.85$ is the refractive index of ZnTe at $\lambda = 800$ nm. Thickness of the crystal is $L = 200$ μm and the modulation of the balanced photodetectors is $(A-B)/(A+B) = 0.65$. Assuming the electro-optical coefficient of ZnTe is $r_{41} = 4.04$ pm/V [29], we estimate the peak of the THz electric field in our setup is $E_{\mathrm{THz}} = 44.2$ kV/cm. Also, there is around 15% Fresnel reflection losses. We account for it to validate our estimation of the peak electric field to be around 50 kV/cm.

2.5 Experimental setup

A schematic view of the experimental setup is given in Fig. 2.8. The optical pump is a mode-locked Ti:sapph laser with a repetition rate of 1 kHz. The laser delivers 1.2 W of average power and has 800 nm pulses with 45 fs duration. In the probe arm, 5 percent of

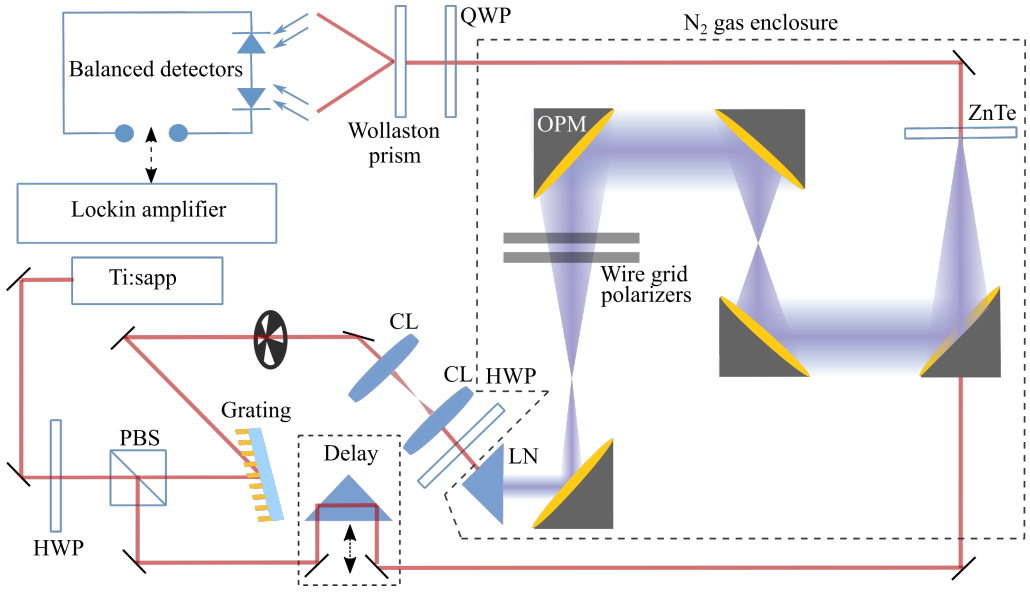

Figure 2.8: THz generation and detection setup scheme. A half-wave plate (HWP) and a polarizing beam splitter (PBS) are used at the beginning of the setup to split the pump and probe beams. Also, two cylindrical lenses (CL's) are used to image the grating inside the generation crystal. The dashed line around the THz part of the setup shows the N_2 enclosure. A pair of free-standing wire-grid polarizers are used to control the intensity of the THz beam at the location of the sample under test.

the input power is split using a polarizing beam splitter (PBS) to co-propagate with the THz pulse in time and space inside the detection crystal (ZnTe). The polarization of the pump laser in the generation crystal ($LiNbO_3$) will be vertical. However, we convert the polarization state of the pump to horizontal using the PBS to maximize the diffraction efficiency of the grating, and later on we convert it back to vertical using a half-wave plate (HWP) right before the generation crystal. We performed a knife edge test and found the FWHM of the beam to be 5 mm. The beam size is then used to find the appropriate size of the generation crystal which is found after considering the size of the pump beam and the required magnification of the tilted-pulse-front technique. A chopper is positioned in

front of the pump beam to allow for modulation of the THz beam and to create a good reference signal for the Lockin amplifier. The chopping frequency is set to one-quarter of the laser repetition rate (250 Hz). This chopping frequency is the same as measuring every four pulse of the laser. This narrower bandwidth of the signal provides a better SNR by removing the noise that arises after the chopped signal. We also took a triggering signal from the laser and used it as the chopper reference signal. This is done to compensate for the timing jitter of the mode-locked laser, resulting in a higher SNR output data. To describe the performance of a particular TDS system, THz researchers report on the SNR and dynamic range (DR), and they are often being used interchangeably. The SNR is given by the ratio of the mean peak of the signal to its standard deviation, while the DR is the ratio of the mean peak of the THz signal to the standard deviation of the noise [69]. We estimate the DR of the THz electric field data in our setup to be of the order of 10^4.

To further improve the setup, we tweak the chirp parameter of the pump to gain higher THz intensity. THz generation happens through a nonlinear optical process and it is more efficient for shorter pulses. On the other hand, the pump pulse travels for some distance and transmits through a few dispersive optics. To compensate for the group velocity dispersion (GVD) broadening of the pulse, we initially chirp the pulse (negatively) so that it narrows down until it reaches the generation crystal. The efficiency of the THz generation is shown in Fig. 2.9 where maximum THz radiation is achieved once the pump pulse is initially chirped to have 110 fs duration. THz voltage is measured using a pyroelectric THz detector from Microtech instruments that is connected and synced to the lockin amplifier.

Apart from the efficiency of the generation process, we ideally want to have a gaussian THz beam with a smooth profile, so that we can focus it tightly using the off-axis parabolic

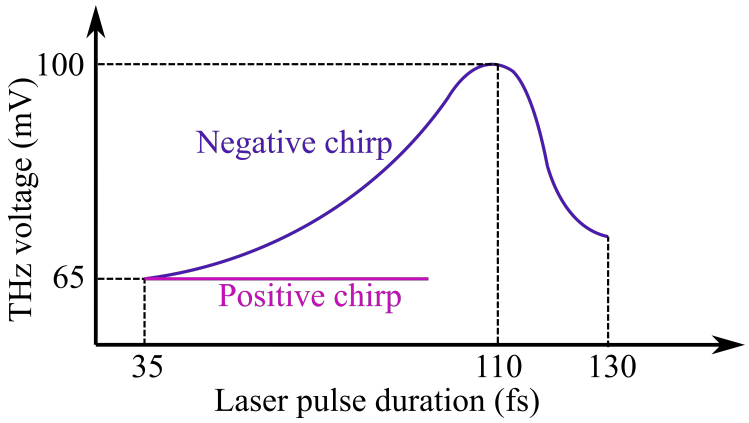

Figure 2.9: Effect of the chirp of the NIR pulse on THz yield.

mirrors (OPM's). This can be achieved by filtering out the higher diffraction orders entering the generation crystal. Fig. 2.10 shows the effect of this spatial filtering on the profile of the generated THz beam. We captured the profile of the THz beam after the generation crystal using an uncooled bolometric camera (INO Microxcam-384i). It can be seen from Fig. 2.10(a) that before the spatial filtering, there is a bump near the peak of the beam profile. This bump is later on removed when spatial filtering is applied (Fig. 2.10(b)). Also, in both cases, THz power keeps increasing by applying an initial negative chirp to the pump pulse until the peak level reaches its maximum at around 114 fs.

After the THz beam is generated inside the $LiNbO_3$, off-axis parabolic mirrors are used to direct and focus/refocus the radiation. The idea is to magnify the beam using mirrors with different sizes and reflective focal lengths (RFL) to be able to increase the intensity as much as possible by tightly focusing the light. Fig. 2.11(a) shows the mirror arrangement used to focus the THz beam. Two images of the beam (side view and top view) captured by the THz camera are shown at the focus point in Fig. 2.11(b). THz mirror alignment is challenging due to invisibility of the THz radiation. We align the mirrors

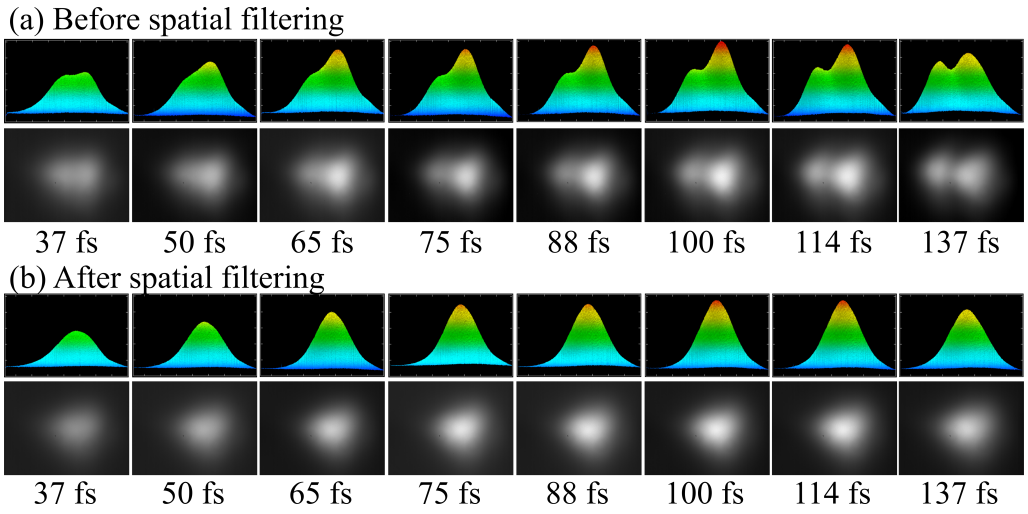

Figure 2.10: Effect of the chirp and spatial filtering of the pump pulse on the strength and shape of the THz beam right after the generation crystal. Images in the first row in (a) show the side view of the THz beams before the spatial filtering. Images in the second row of (a) show the top view of the beam profile. Brighter regions show higher THz power. Images in the first row in (b) show the side view of the THz beams after spatial filtering. Images in the second row of (b) show the top view of the beam profile. Width of each image is 1.2 cm.

altogether beforehand on a separate board using a HeNe laser beam. Then we slide the board into the experimental setup and fix it in the right position with reference to the THz beam imaged at the detector position. We also account for the noncollimation of the THz beam right after the generation crystal. The divergence of the beam after the crystal is shown in Fig. 2.11(c).

Since THz beam is very sensitive to the mirror positions, one has to be careful with the alignment of the parabolic mirrors to obtain a THz beam at the focal point with a gaussian transverse profile that is sharp and symmetric with minimal aberrations. We measure the spot size of the focusing THz beam at different locations along its propagation direction (or y-direction shown in Fig. 2.11(a)) using Knife edge technique. The results of the

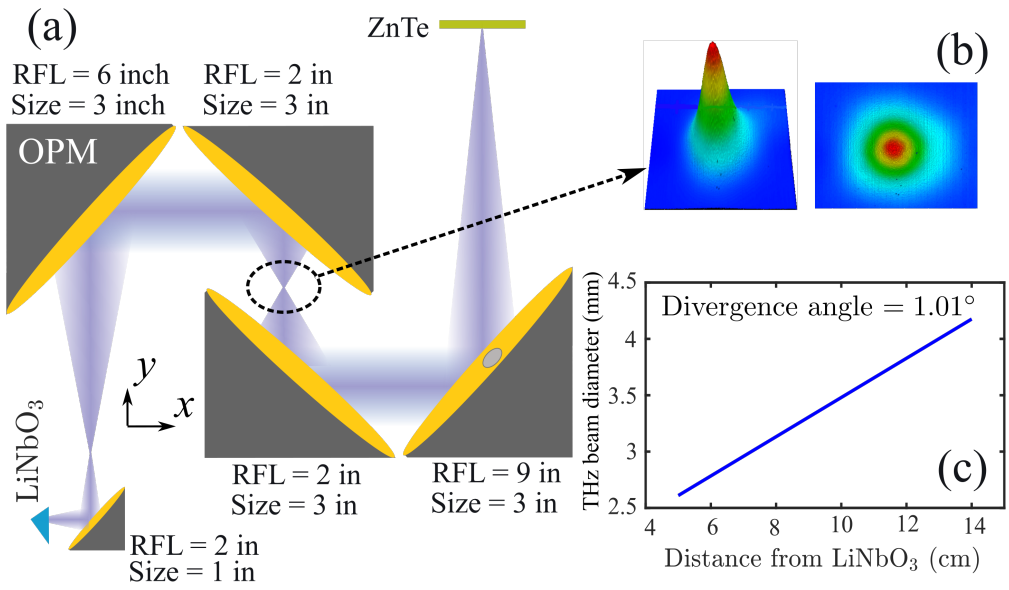

Figure 2.11: (a) Parabolic mirror arrangement of the setup. We use different size OPA's with different reflective focal lengths (RFL's). The dimensions and distances are in scale. (b) Images of the THz power at the focus. (c) the beam diameter of the generated THz radiation in the $LiNbO_3$.

measurement are shown in Fig. 2.12(a) where the measured values at each y point are fitted by error functions. The derivative of the fitted error functions is shown in Fig. 2.12(b).

As we move along the y-direction, the spot size is getting smaller meaning that beam is focusing. At some point it has its minimum value ($684\,\mu m$). This spot size is about 1λ at 0.5 THz. We place our test materials at this location to perform the THz nonlinear measurements. After the focus point, the THz beam starts to defocus. We find the Rayleigh length based on the measured profiles shown in Fig. 2.12 to be ≈ 2.8 mm. This length is the same as the theoretical Rayleigh length calculated at 0.5 THz, which is the frequency at which the source spectrum has its maximum amplitude.

We enclose the experimental setup to be able to purge it by N_2 to avoid unwanted

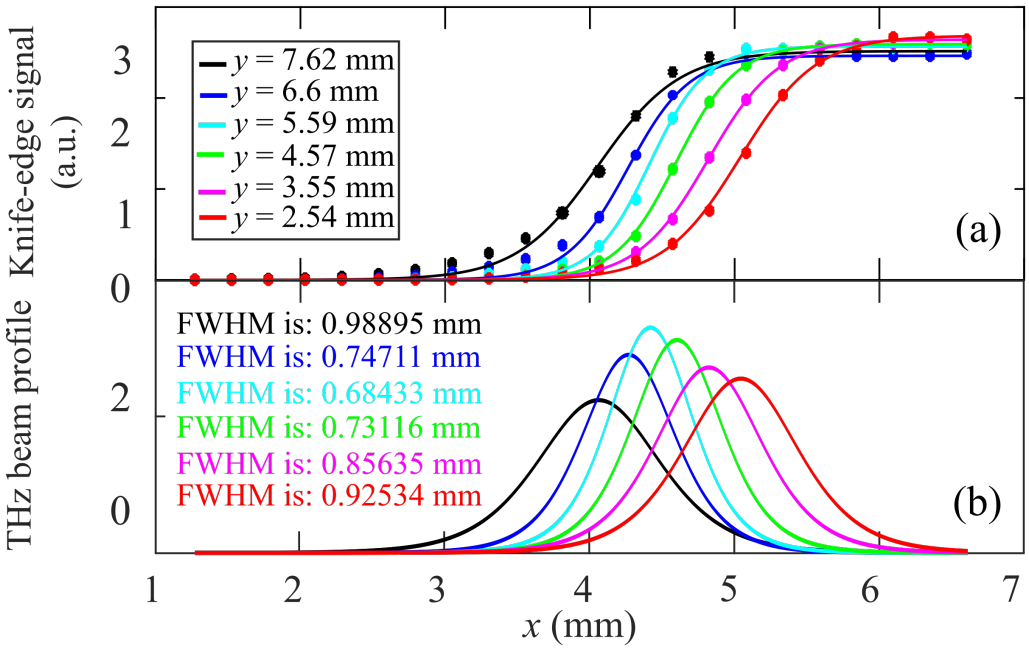

Figure 2.12: (a) Knife edge signal and the fitted error functions. (b) Transverse profile of the THz beam along the focusing beam.

resonances of water vapour molecules with THz spectral components by minimizing the free space humidity at the THz beam.

We control the THz field using a pair of THz polarizers. We collect the spectral response at different THz powers by rotating the first polarizer while keeping the second one fixed to maintain a constant polarization state. These polarizers are free-standing wire grids, and they do not introduce any delay to the THz field. Also, we expect to see negligible dispersion of the THz pulse transmitting through these polarizers, specifically for the field amplitudes greater than 0.1 kV/cm. The profile of the maximum detected THz electric field is shown in Fig. 2.13 in both time and frequency domains. The spectrum of the electric field is found by performing the fast Fourier transform (FFT) on the temporal

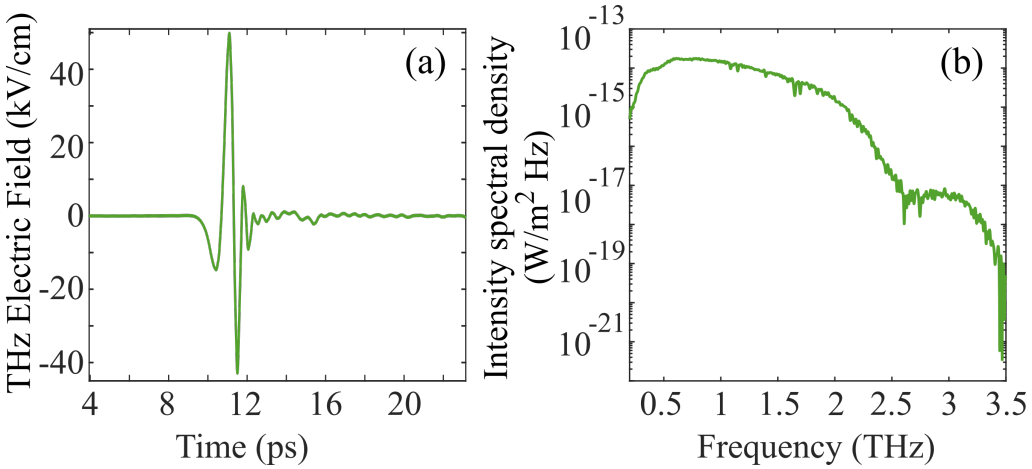

Figure 2.13: Profile of the detected electric field in (a) time and (b) its field intensity in frequency. The area under this spectrum density shows the intensity of the source (W/m^2).

shape. In order to find the absolute intensity spectral values of the electric field (E) in units of W/m^2Hz, we apply the Parseval's theorem to re-scale the FFT values, and we use the equation

$$I = \frac{1}{2}\varepsilon_0 c |E|^2. \tag{2.36}$$

By comparing the maximum intensity value of the signal shown in Fig. 2.13(b) and its intensity level after 2.5 THz, one can find the dynamic range to be around 10^4. Also, to find the value of the field at the focus, we multiply the peak value of the field (50 kV/cm) by 4.5 which is the focal length ratio of the parabolic mirrors, to obtain the peak field value of 225 kV/cm at the focus.

2.6 Conclusion

In conclusion, a THz-TDS system is built and improved through experimental work where the magnitude of the THz radiation reaches 225 kV/cm at the focal point. Also, the dynamic range of our TDS system is of the order of $\approx 10^4$. We use the experimental setup as described here to measure the nonlinear refractive index in water vapour and different solids.

3. Modelling of the THz pulse propagation

Modelling of the THz pulse propagation leads to a better understanding of the modification of the THz field after it transmits through the material. Also, the interaction of the THz pulse and material can be studied by taking into account the effect of Phonon contribution to the previously present instantaneous nonlinear response. Previous studies indicate that by operating close to the vibrational lattice resonance, a delayed nonlinear response will be created in addition to the instantaneous electronic response. This results in the enhancement of the overall third-order nonlinear Kerr effect by several orders of magnitude [38, 51, 57]. However, it is not clear what the share of the delayed response in the strength of the overall Kerr effect is.

In this Chapter, we study the characteristic time scales for different contributions to the overall Kerr effect during the nonlinear optical interactions at the THz frequencies. This can be done by setting a frequency dispersive polarization term in the numerical simulations for the nonlinear response of the material.

3.1 Material response time

Different physical processes induce nonlinear polarization and change the refractive index of the material during light-matter interactions. These mechanisms have different time characteristics for the nonlinear response to develop. Table 3.1 summarizes the nonlinear refractive index coefficient (n_2) as well as the corresponding characteristic time of each physical process. As we can see, the molecular orientation with a pico-second characteristic

Physical Mechanism	$\mathbf{n_2}$ (cm^2/W)	**Response Time** (sec)
Electronic polarization	10^{-16}	10^{-15}
Molecular orientation	10^{-14}	10^{-12}
Saturated atomic absorption	10^{-14}	10^{-9}
Electrostriction	10^{-10}	10^{-8}
Thermal effects	10^{-6}	10^{-3}

Table 3.1: Different physical processes that induce nonlinear refractive index change in the material. The data is taken from [17]. Different mechanisms provide the nonlinear response with different strengths. The change in the refractive index as a result of molecular movement has a pico-second characteristic time and is stronger than the nonlinear refractive index with electronic origin.

time is two orders of magnitude stronger than the electronic polarization. This can be another promising sign to observe strong nonlinear response at THz frequencies. We study the characteristic time scales for different contributions to the overall Kerr effect during the nonlinear optical interactions at the THz frequencies by adopting a model taking into account both contributions of the Kerr effect corresponding to an instantaneous and retarded third-order nonlinear responses. This model is similar to the conventional model for the Raman effect in silica fibers [52]. Since lattice-driven nonlinearities are slower than

the electronic responses, they are modelled in a similar manner to the stimulated Raman scattering (SRS) in silica fiber where there is a long interaction length with optical pulses resulting in important changes in the optical spectrum observed at the fiber output.

3.2 Numerical technique

In order to accurately model the electric field propagation in the THz range, one needs to use the proper approximations while solving Maxwell's equations. In the many-cycle regime of optical pulses where there are several carrier oscillations within the envelope of the pulse, the slowly varying envelope approximation (SVEA) is valid [17]. The SVEA neglects the second-order spatial derivative of the field in the wave equation and leaves only the first derivative with respect to the spatial coordinate along the propagation direction. For both ultra-short optical pulses and broadband THz transients, where the pulse envelope contains only a few optical cycles, the SVEA is no longer valid and fails to describe the propagation of such pulses [[17],[70]]. In this study, we use a unidirectional pulse propagation equation (UPPE) [71, 72] which gives a seamless transition from Maxwell's equations to an optical pulse propagation model without making the SVEA. The UPPE is a non-paraxial version of the Forward Maxwell Equation (FME) which is itself a paraxial equation. However, both UPPE and FME allow for diffraction in the transverse plane as well as for modelling space-time focusing [73]. This comprehensive model helps with building a rich environment in which one can see and account for the impact of different linear and nonlinear effects on the electric field, as well as on the spatial profile of the THz field during its propagation. This knowledge can be useful in the interpretation of

THz-TDS measurements, and it can help with estimating the material parameters when comparing the simulation and experimental results. Both linear and nonlinear propagation effects of a single-cycle THz pulse are accounted for in our model. To quantify the effect of dispersion on the induced nonlinearity, we compare two scenarios: an optical pulse propagating inside (i) a material with strong normal dispersion and (ii) a material with anomalous dispersion.

3.2.1 UPPE

The derivation of the UPPE equations has been done in [71, 74] using two different approaches based on the temporal (time-propagated UPPE) and spatial evolution. The spatial coordinate in the latter is usually chosen as z (z-propagated UPPE). The initial condition for a time-propagated UPPE is in general the electric and magnetic fields' amplitudes of a pulse at an initial moment as functions of spatial coordinate. On the other hand, the initial condition for the z-propagated UPPE is the electric and magnetic fields' amplitudes at a fixed location as functions of time. This requires a complete knowledge of the total field at all the past and future times, which makes it hard to implement without simplifying assumptions. Although we use the UPPE solver that applies the actual time-propagated approach based on a direct integration of Maxwell's equations, here we present an intuitive (with approximations) derivation of the other similar approach (z-propagated UPPE) to be able to introduce the UPPE on the terms that we are interested in. This procedure has been given in detail in [71, 72].

In order to derive the z-propagated UPPE, we start from the most general form of the Maxwell's equations. Combining the Maxwell-Ampère and Maxwell-Gauss differential

equations, one can obtain:

$$\nabla^2\mathbf{E} - \nabla(\nabla\cdot\mathbf{E}) + \frac{\omega^2 n^2(\omega)}{c^2}\mathbf{E} = \mu_0(-i\omega\mathbf{J} - \omega^2\mathbf{P}). \tag{3.1}$$

Here, **E**, **P** and **J** are space and frequency dependent vectors of the electric field, nonlinear polarization and current density of free charges, respectively. The third term on the left is the Fourier transform of a time convolution of the material permittivity $\varepsilon(\omega)$, which is related to the dispersive refractive index of the material as $\varepsilon(\omega) = n^2(\omega)$. We then make some assumptions to simplify the problem. We first assume that the electric field propagates along the z direction, and that it is linearly polarized along a direction in the transverse plane, perpendicular to the propagation direction (z). This allows the second term in Eq. (3.1) to vanish (as long as the beam is not strongly focused). Unless one is interested in the separate contribution of the current in the material response, one can combine the terms on the right-hand side of Eq. (3.1) by using the equivalent of free charge current, which is a time derivative of the nonlinear polarization. Finally, by projecting Eq. (3.1) onto the polarization direction, one can obtain the scalar form:

$$(\partial_z^2 + \nabla_\perp^2)\,E + k^2(\omega)\,E = -\mu_0\omega^2 P, \tag{3.2}$$

where $k(\omega) = n(\omega)\,\omega/c$. By rearranging the above equation and factorizing the forward and backward propagators, one can obtain [75]

$$[\partial_z + ik(\omega)]\,[\partial_z - ik(\omega)]\,E = -\nabla_\perp^2\,E - \mu_0\omega^2 P. \tag{3.3}$$

The general solution to this equation under the assumption that there is no diffraction in the transverse plane ($\nabla_{\perp}^2 E$) and no nonlinear polarization (P) consists of a forward and a backward propagating field

$$E = E^{+} \exp\left[ik(\omega)z\right] + E^{-} \exp\left[-ik(\omega)z\right]. \tag{3.4}$$

FME is obtained by assuming that the forward-propagating part is dominant ($|E^{+}| \gg |E^{-}|$):

$$\frac{\partial E}{\partial z} = i\left[k(\omega) - \frac{k_{\perp}^2}{2k(\omega)}\right] E + i\frac{\mu_0 \omega^2}{2k(\omega)} P. \tag{3.5}$$

In the above equation, there is an inherent assumption that the transverse components of the wavevector are negligible in comparison to the longitudinal components.

3.2.2 Non-Paraxial Regime

In general, the condition $|k| \gg |k_{\perp}|$ used in the FME given by Eq. (3.5) represents a fair approximation, especially for the visible and near-infrared ranges. However, in THz frequency range, where the propagating pulse contains a wide-band spectrum, meaning that the spectral pulse width and the central wavenumber are comparable, this condition is often not valid. Hence, in order to get a more accurate picture of the THz beam focusing, it is desirable to go back to the non-paraxial regime where the extent of the angular spectrum of the field is non-negligible compared to the wavenumber of the beam along the propagation axis [76, 77]. With this in mind, we take Eq. (3.2) and rewrite it in a more general form:

$$\left\{\partial_z^2 + \left[k^2(\omega) - k_{\perp}^2\right]\right\} E = -\mu_0 \omega^2 P. \tag{3.6}$$

Following the procedure similar to that used for deriving Eqs. (3.3)-(3.5), the UPPE with no paraxial approximations can be obtained:

$$\frac{\partial E}{\partial z} = i\sqrt{k^2(\omega) - k_\perp^2}\, E + i\frac{\mu_0 \omega^2}{2\sqrt{k^2(\omega) - k_\perp^2}} P. \tag{3.7}$$

This is a more general version of the UPPE called z-propagated UPPE [71]. The first term on the right-hand side represents the dispersion and frequency-dependent diffraction, while the nonlinear polarization is accounted for in the second term.

3.2.3 Nonlinear Response Modelling

Let us consider the propagation of a broadband THz pulse in a material with a third-order nonlinear optical response. The induced polarization can be represented as the sum of the linear and nonlinear contributions. The nonlinear polarization can be related to the electric field $E(t)$ and to the time-dependent susceptibility as [52]

$$P(t) = \varepsilon_0 \chi_0^{(3)} E(t) \int g(t - t')\, E^2(t')\, \mathrm{d}t'. \tag{3.8}$$

Here $\chi_0^{(3)}$ is a scaling factor, and $g(t)$ is the response function given by

$$g(t) = \alpha\, \delta(t) + (1 - \alpha)\, g_R(t). \tag{3.9}$$

The first term in Eq. (3.9) describes the instantaneous Kerr effect, while the second term describes the delayed lattice-related effect, modeled by a single Lorentzian function,

centered at the phonon resonance frequency

$$g_R(\omega) = \frac{\omega_R^2}{\omega_R^2 + 2i\,\omega\,\delta_R - \omega^2}. \tag{3.10}$$

Here ω_R is the angular frequency of the phonon resonance and δ_R is the resonance linewidth. The parameter α ($0 \leq \alpha \leq 1$) in Eq. (3.9) determines the ratio of the Kerr susceptibility to the overall susceptibility including both Kerr and lattice-related effects. In other words,

$$\alpha = \frac{g(t) - g_R(t)}{\delta(t) - g_R(t)}. \tag{3.11}$$

By setting α to 1, one can eliminate any delayed response and observe the instantaneous Kerr response alone, while $\alpha = 0$ gives the delayed Kerr response, only. Using Eqs. (3.8) and (3.9), we can study the impact of the parameter α, describing the role of vibrational modes in the overall nonlinear response, on the induced polarization and the transmitted THz pulse. Fig. 3.1 shows the response times we use to model the delayed response of the material. On the left hand side of the Fig. 3.1 we see the lattice-driven response time where typical values are $\tau = 10$ fs to $\tau = 100$ fs. On the other hand, electronic response is much faster (less than 1 fs). We investigate the effect of the response times as well as the contribution of lattice-driven response in the overall Kerr+lattice-driven response in the transmission of the intense THz electric fields. Also, in order to obtain the lattice-driven response function $[g_R(\omega)]$, we take the reported values for the linear refractive indices (see Fig. 3.2) and absorption coefficient of the materials at the THz frequencies, and we calculate the $\chi^{(3)}$ dispersion using the two-level atom approximation [17]. In such a way, we obtain the material-specific response time ($1/\delta_R$) and phonon resonance frequency

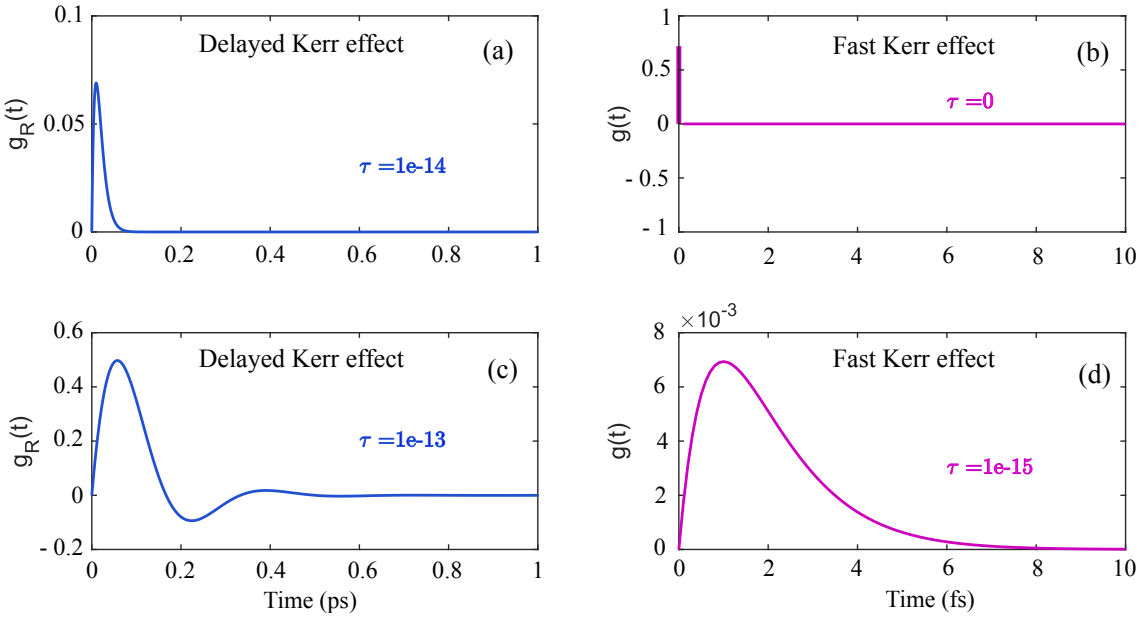

Figure 3.1: The typical response times that we use to model the delayed response of the material. (a) and (c) show the delayed response times for the Kerr effect while (b) and (d) show the typical (fast) electronic response times. The delayed response time is about 100 times slower than the electronic response time.

(ω_R) from the $\chi^{(3)}$ dispersion curve, and we plug them into Eq. (3.10).

3.3 Results and Discussion

We use the gUPPEcore package [80] to solve UPPE describing the propagation of a THz pulse within a dielectric material. In order to be consistent with most of the practical THz pulses, we set the spectral range of our input pulse between 0 and 3 THz. For the simulations, we have included both the linear and nonlinear instantaneous and Lorentz-dispersive effects. Also, we work in a non-paraxial regime, and there is no SVEA. We let the beam propagate through two different materials having linear optical properties

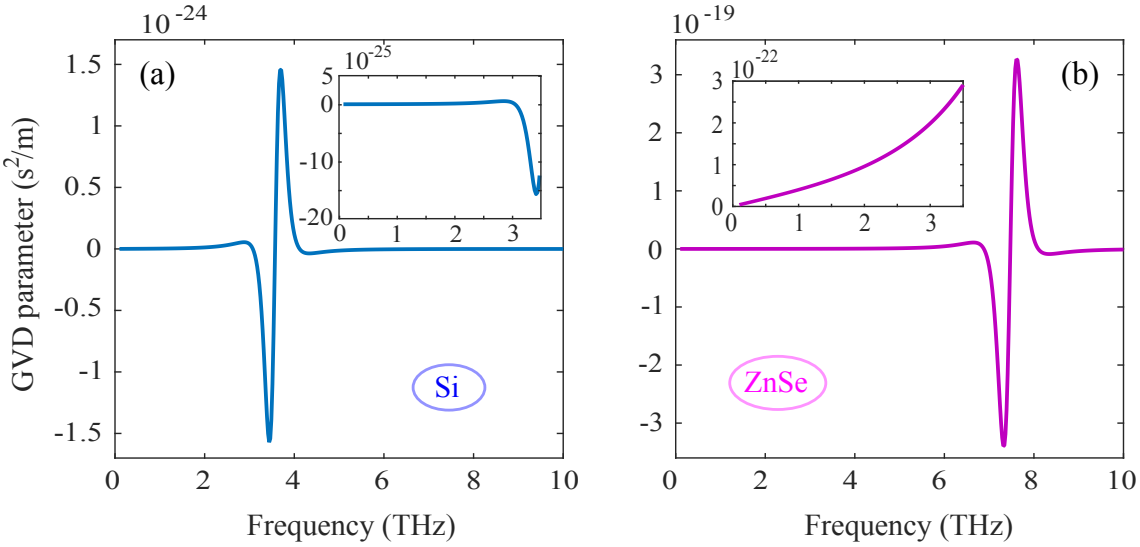

Figure 3.2: Group velocity dispersion curves for (a) silicon and (b) ZnSe materials calculated from [78] and [79], respectively. The inset shows the GVD in the frequency range of interest. The GVD of ZnSe is 200 times larger compared to the GVD in Si at that frequency range.

of two broadly used semiconductors: silicon (Si) and zinc selenide (ZnSe), and we compare the results. The reason behind this material selection is the totally different linear dispersions of the two materials in the frequency range of interest. Group velocity dispersion (GVD) of both materials is given in Fig. 3.2. Si shows a weak anomalous GVD in the operation frequency range (0-3.5 THz) [78], while ZnSe exhibits a normal GVD in the same frequency range, together with a strong phonon resonance at $\sim$ 6.6 THz [79]. In the following, we systematically study the influence of different mechanisms on the temporal, spatial and spectral profile of the propagating THz pulse.

3.3.1 THz Electric Field

We studied the transition of light-matter interaction from the linear ($n_2 = 0$) to an arbitrarily high nonlinear regime ($n_2 = 1 \times 10^{-15}\,\mathrm{m}^2/\mathrm{W}$) for different strengths of the lattice-related effect, described by the parameter α.

For the nonlinear study, we first set α to 1 to consider the instantaneous Kerr contribution only. After that, we set α to 0.9 to add a small contribution from the lattice-related (non-instantaneous) effect. The intensity of the input pulse was set to $I = 1 \times 10^{13}\,\mathrm{W/m}^2$, while the thicknesses of both samples were set equally to 2 cm. Also, the input pulse duration was set to $\tau = 0.5$ ps, and the initial beam waist was $w_0 = 1.5$ cm. The temporal profiles of the input THz electric field after its propagation through Si are shown in Fig. 3.3. For Si, the pulse affected by the instantaneous Kerr effect experiences around 3.4 ps

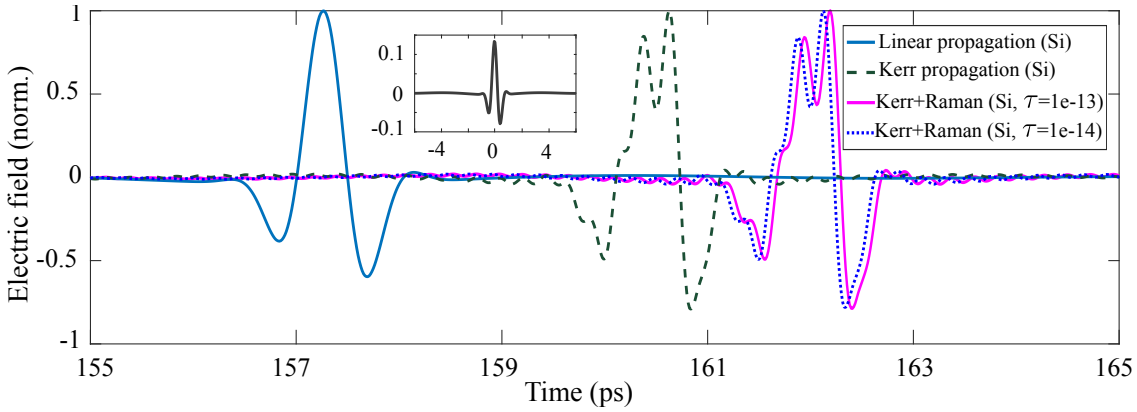

Figure 3.3: Propagation of the THz pulse in (a) Si. The linear (solid light blue curve) arrives the first. The THz pulse propagated in the Kerr medium (dashed green line) arrives with a time delay of 3.4 ps. Finally, the THz pulses propagated in the Kerr+lattice-driven medium (dotted blue and solid violet lines) arrive one after another with a time delay of ≈ 5 ps. The inset shows the initial THz electric field.

time delay due to the refractive index change of at least $\Delta n = n_2 I = 0.01$. Moreover, the

lattice-driven contribution introduces an additional time shift to the propagating pulse affected by the Kerr nonlinearity. This time shift becomes slightly larger when the response time of the phonons changes from 10 to 100 fs (solid violet line in Fig. 3.3). The phonon resonance frequency of Si is set to 3 THz. On the other hand, the phonon resonance of ZnSe is calculated to be at 6.6 THz with a linewidth of 1 THz, which gives a response time of 1 ps. As shown in Fig. 3.4, pulses affected by Kerr and Kerr+lattice-related effects

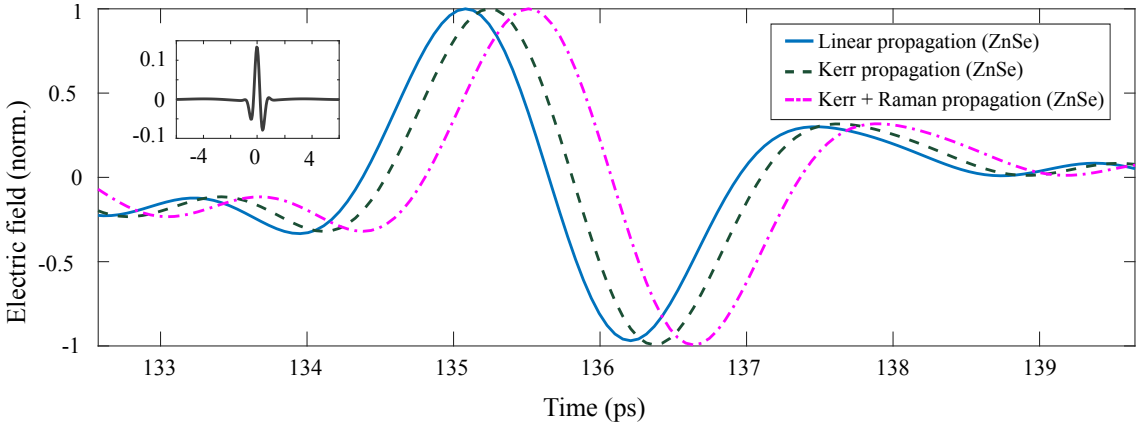

Figure 3.4: Propagation of the THz pulse in ZnSe. The linear (solid light blue curve) arrives the first. The THz pulse propagated in the Kerr medium (dashed green line) arrives with a time delay of 240 fs. Finally, the THz pulse propagated in the Kerr+lattice-driven medium (dash-dotted violet line) arrives with a time delay of $\approx$ 500 fs. The inset shows the initial THz electric field.

experience 240 fs and 500 fs time shifts, respectively. Since there is a strong dispersion associated with ZnSe, the time delays in this case are smaller compared to the time delays of the pulses in Si.

3.3.2 Self-Focusing

Self-focusing of light is a third-order nonlinear optical process in which an intense beam of light changes the refractive index of the medium in such a manner that the beam is forced to come to a focus inside the material. Self-focusing is the spatial analog of self-phase modulation (SPM), which is the change in the phase of an optical pulse resulting from the nonlinearity of the refractive index of the material medium [17]. SPM depends on the linear dispersion during the propagation of an optical pulse in a material. It is, therefore, necessary to consider the combined effects of SPM and GVD on the pulse evolution. It can be shown that a medium with a normal GVD introduces a time broadening to the propagating pulse, while the pulse broadening is less pronounced in a medium with an anomalous GVD, whereby optical soliton propagation is possible [81]. This could be understood by looking at the effect of dispersion on the newly generated frequencies due to the SPM, in the two different dispersion regimes. In the normal dispersion regime, the lower frequencies generated at the leading edge tend to travel faster than the higher frequency components at the trailing edge of the pulse, hence, SPM leads to enhanced rate of broadening of the pulse. However, in the anomalous dispersion regime, trailing edge of the pulse travels faster than the leading edge which results in the much smaller rate of the pulse broadening than expected in the absence of SPM. We have studied the effect of GVD on the self-focusing of THz pulses in the two materials with different GVDs. Figs. 3.5 and 3.6 show the intensity distribution of the THz field in Si and ZnSe, respectively. The subplots show the pulses at different propagation distances (left to right) and under different polarization models of linear, Kerr and Kerr+lattice-driven (top to bottom). It is shown in Fig. 3.5 that, during the nonlinear propagation (second and third rows), the initial

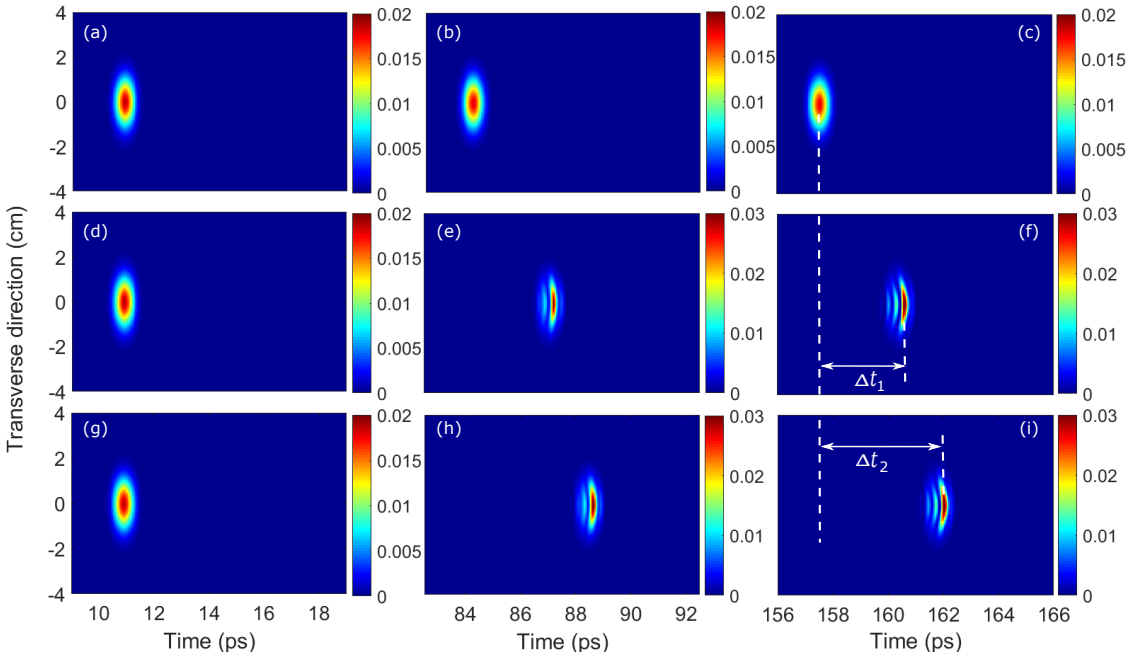

Figure 3.5: Intensity distribution of the THz field at different propagation distances (left to right) in Si. (a) - (c) assumes a linear propagation, (d) - (f) shows the results of Kerr effect (no lattice-related effect), and (g) - (i) gives the intensity distribution for the combined Kerr+lattice-related effect ($\alpha = 0.9$) during the pulse propagation. The pulse is delayed by $\Delta t_1 = 3.4$ ps due to the Kerr effect. This amount of time shift is a result of an overall refractive index change of at least $\Delta n = n_2 I = 0.01$. Kerr+lattice-driven contribution introduces a larger time shift of $\Delta t_2 = 5$ ps.

spatial Gaussian profile of the pulse does not remain Gaussian in Si and breaks up into a strong self-focused trailing peak and a weak leading pulse. However, this is not the case with ZnSe material (See Fig. 3.6). In ZnSe, due to the 200 times stronger GVD parameter, the bending of spatio-temporal profile does not occur. In other words, normal dispersion compensates for the nonlinear refraction, inhibiting the self-focusing effect. The described interplay of SPM and GVD can be quantified by taking the ratio of the dispersion length to the nonlinear length: $L_{\mathrm{D}}/L_{\mathrm{NL}}$ [81]. This ratio governs the relative importance of GVD

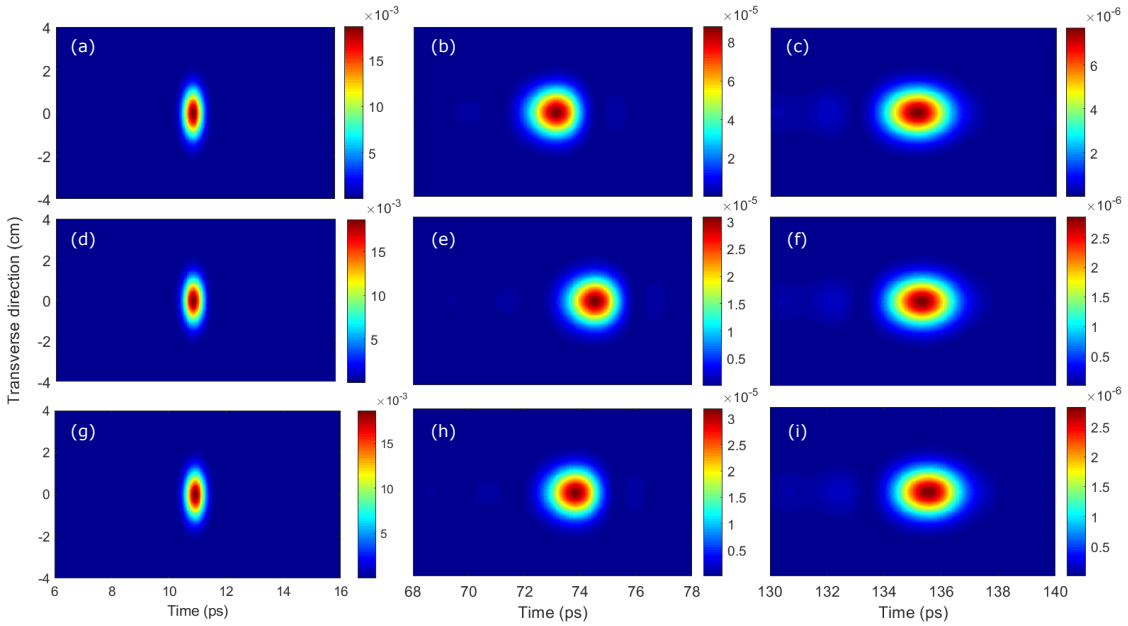

Figure 3.6: Intensity distribution of the THz field at different propagation distances (left to right) in ZnSe. (a) - (c) assumes a linear propagation, (d) - (f) shows the results of Kerr effect (no lattice-related effect), and (g) - (i) gives the intensity distribution for the combined Kerr+lattice-related effect during the pulse propagation. The amount of time shift introduced by Kerr+lattice-related effect is twice as large as the time shift introduced by pure Kerr effect.

and SPM effects during the pulse propagation. If this ratio is much greater than one, SPM dominates, otherwise, GVD dominates. Here, we calculate $L_{\mathrm{D}}/L_{\mathrm{NL}}$ for both Si and ZnSe to be able to see the relative strength of GVD over SPM in the two samples. The dispersion length (L_{D}) can be defined as the length at which the effective pulse width increases by a certain factor, and is related to the GVD parameter as

$$L_{\mathrm{D}} = \frac{\tau^2}{|\beta_2|}. \tag{3.12}$$

Here, $\tau = 0.5$ ps is the initial time duration of the pulse, and β_2 is the GVD parameter (in s^2/m). The nonlinear length (L_{NL}) is the effective propagation length at which the acquired nonlinear phase shift of the pulse is one radian. It depends on the peak power P of the pulse as

$$L_{NL} = \frac{1}{\gamma P}, \tag{3.13}$$

where γ is the nonlinear coefficient, defined as [81]

$$\gamma = \frac{n_2\,\omega_0}{c\,A_{eff}}. \tag{3.14}$$

Here n_2 is the nonlinear refractive index, c is the speed of light in vacuum and A_{eff} is the effective mode area, which in our case is $A_{eff} = 7.07 \times 10^{-4}$ m^2. The peak power of the pulse is $P = 7.07 \times 10^9$ W. We calculated γ to be 3×10^{-8} $(Wm)^{-1}$ at the central frequency 1 THz. Therefore, for Si we get the ratio of the dispersion to the nonlinear lengths to be $L_D^{Si}/L_{NL}^{Si} \approx 520$. The same calculation for ZnSe yields $L_D^{ZnSe}/L_{NL}^{ZnSe} \approx 1$. This explains why self-focusing does not occur in ZnSe (Fig. 3.6): due to the larger contribution from GVD.

3.3.3 Diffraction and Spectral Broadening

Due to the super-long wavelength regime of THz radiation, it is more diffractive than optical or near-infrared radiation. We take a closer look at the diffraction of the beam and see how linear and nonlinear behaviour of the material can modify its diffraction pattern. Fig. 3.7 shows the diffraction of the spectral components of the THz beam in Si in arbitrary logarithmic units.

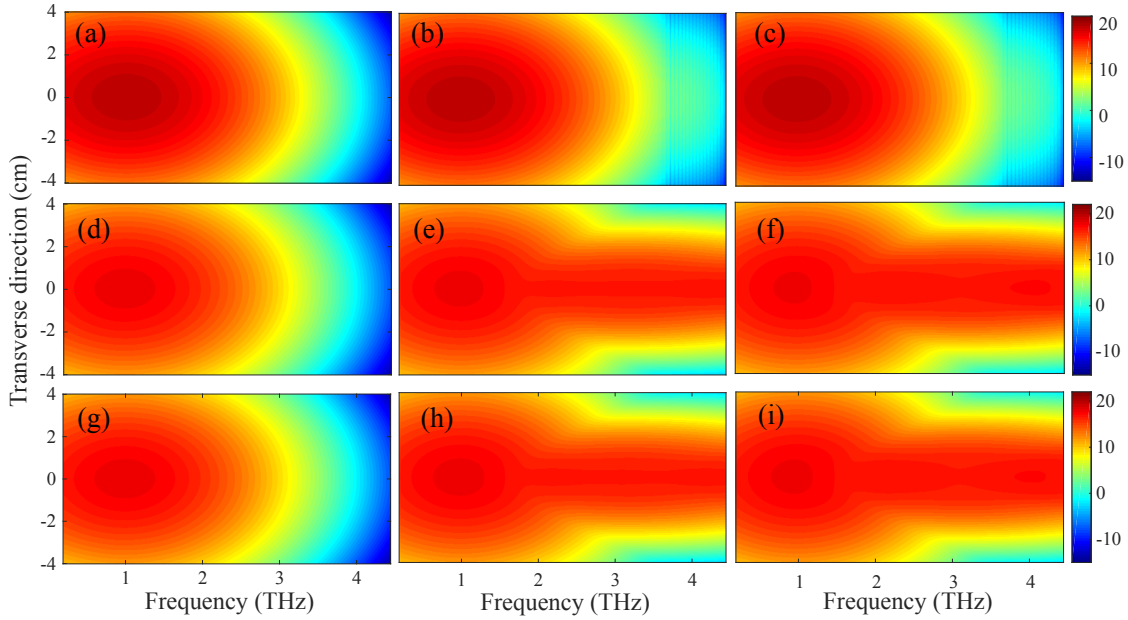

Figure 3.7: Intensity distribution (logarithmic units) of THz spectral power at different propagation distances (left to right) in Si. Spatio-spectral plots visualize the spectral broadening/shrinking of the pulse as well as the diffraction effects. First row [(a) - (c)] assumes a linear propagation. Second row [(d) - (f)] shows the results of Kerr effect (no lattice-related effect), and third row [(g) - (i)] gives the the combined Kerr+lattice-related effects during THz pulse propagation in Si.

Higher frequency components naturally tend to localize closer to the beam axis than the lower frequency components (see the outward curvature of the spectral distribution). Spectral broadening due to SPM is also shown in the same figure. One can see that, except for the linear case [Fig. 3.7 (a)-(c)], there is a strong spectral broadening occurring as a result of the nonzero third-order susceptibility. Moreover, as shown in Fig. 3.7 (g)-(i), lattice-related effect contributes equally to the frequency generation as the Kerr effect. This spectral broadening is more pronounced for quasi-longitudinal rays compared to the off-axis rays located far from the beam axis.

Fig. 3.8 shows the spectral power of the transverse components of the THz beam in ZnSe in arbitrary logarithmic units. In this case, linear absorption strongly suppresses the higher frequency portion of the spectrum. As mentioned in the previous part, the efficiency of SPM is low due to the strong normal GVD of the ZnSe in this range. Spectral broadening still occurs, but it is less effective than that acquired by the beam in Si. For each plot in the same row, it is seen that the spectrum shrinks as the beam moves forward. Also, unlike the linear case, Kerr and Kerr+lattice-driven propagations demonstrate some spectral broadening which is considerably less efficient than the broadening of the spectrum in Si. Moreover, spectral broadening is the same for the Kerr and Kerr+lattice-related effects, which implies the equal contribution of lattice-related effect and spontaneous Kerr effect to the spectral broadening.

3.4 Conclusion

Nonlinear THz spectroscopy and coherent control of the vibrational states of an arrangement of atoms or molecules in different crystalline structures is an evolving field waiting for more efficient and more accurate modelling techniques to better understand light-matter interaction at the THz frequencies. Also, finding some promising materials that show highly nonlinear behaviour in the THz frequency range seems to be an emerging quest. We presented a model of THz pulse propagation with the emphasis on some of the unique properties of low frequency THz beams, such as non-paraxiality, as well as the single-cycle regime of the pulse. We verified that there could be a strong role played by the phonon contribution to the overall Kerr-type THz nonlinear optical interactions depending

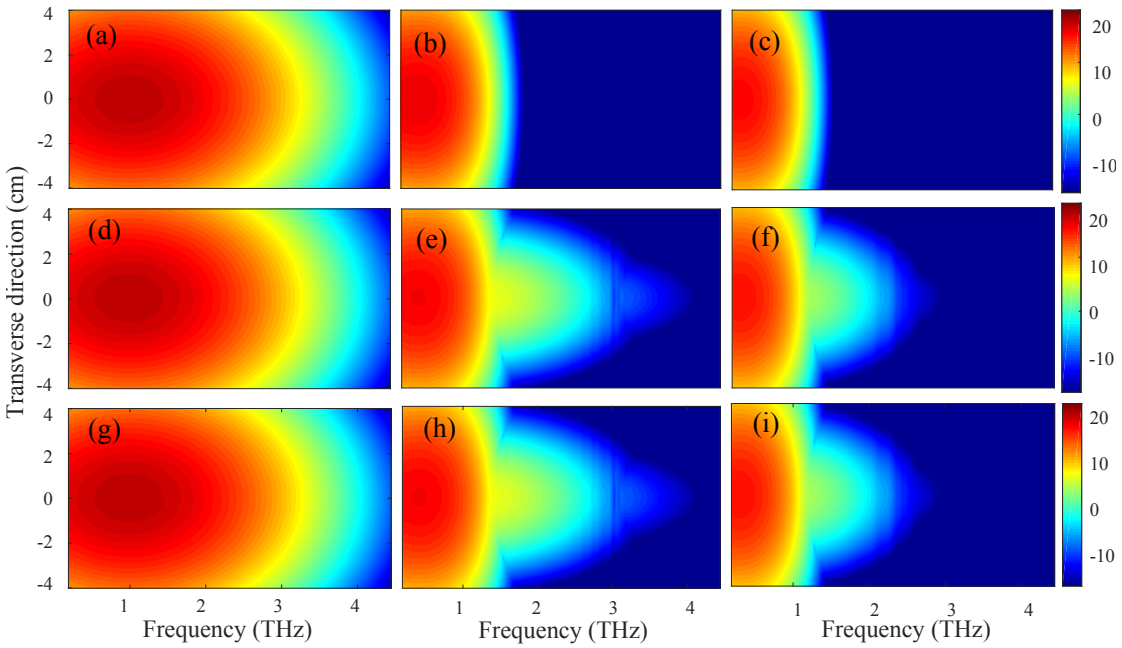

Figure 3.8: Intensity distribution (logarithmic units) of THz spectral power at different propagation distances (left to right) in ZnSe. Spatio-spectral plots visualize the spectral broadening/shrinking of the pulse as well as the diffraction effects. First row [(a) - (c)] assumes a linear propagation. Unlike Si (results shown in Fig. 3.7), linear absorption strongly suppresses the higher frequency portion of the spectrum. Second row [(d) - (f)] shows the results of Kerr effect (no lattice-related effect), and third row [(g) - (i)] gives the the combined Kerr+lattice-related effects during THz pulse propagation in ZnSe.

on the lattice response in the material medium and the intensity of the excitation pulse. This model helps with the extraction of n_2 values during the interpretation of nonlinear THz-TDS measurements. It also helps with finding highly nonlinear solids that show high n_2 levels due to the proximity of their phonon responses at the THz frequencies.

4. THz Nonlinear Optical Response of Water vapour

Water vapour pervades the atmosphere of the Earth and exhibits absorption in a broad frequency range of the electromagnetic spectrum, associated with rotational, as well as inter- and intra-molecular vibrational transitions [82, 83]. The absorption spectrum of water vapour reflects its molecular structure and, therefore, can be used as a spectroscopic fingerprint for its detection and identification. This spectrum is, however, very complex and highly rich in resonances, which have been the center of intense spectroscopic investigations for many decades [84–87]. Moreover, atmospheric water vapour is responsible for almost all the spectral modifications of electromagnetic radiation from 0.5 to 20 THz [88]. It is, therefore, crucial to gain a better understanding of these resonances, especially in the context of high field excitation, due to an increasing demand for high power sources to enable numerous emerging THz applications.

Indeed, THz-based systems are finding a niche in fields such as information and communication technology [5], spectroscopy and imaging [89–91], ultrafast control [92], as well as biomedicine [93, 94]. In addition, long-path THz time-domain spectroscopy in the

open air is realized to demonstrate the potential of line-of-sight THz communications [95, 96], THz sensing [97], monitoring pollutants and dangerous gases [98], non-destructive evaluation [99], global environmental monitoring [100], and THz imaging through the fog and smoke [101], which often require propagation of intense THz pulses through the atmosphere. Therefore, studying the nonlinear response of water vapour in the THz domain not only provides insight into the inter-molecular structure of water vapour but also represents great importance for practical applications.

With the coherent generation and detection of THz radiation, it is possible to measure not only absorption spectra with high spectral resolution, but also the dispersive response of water vapour simultaneously [102]. Also, unlike solids and liquids, gaseous materials such as water vapour can have sharp resonances in the THz range, and the nonlinear THz response of these transitions has not been studied to date.

In this Chapter, we report on the nature of nonlinear interactions of THz pulses with atmospheric water vapour at different THz pulse intensities. First, we measure the linear response of water vapour and explain our results by comparing them with theoretical predictions. Then, we perform nonlinear THz time-domain spectroscopy (THz-TDS) to show how increasing the electric field intensity of the THz radiation modifies the absorption and dispersion of the vapour. In contrast to two-level atomic systems, where the absorption decreases with increasing field intensity, we observe an increase in absorption for some of the transitions. The observed reverse-saturation of absorption is explained based on multi-photon transitions. Furthermore, we show that the THz field experiences an extremely large nonlinear refractive index at frequencies near to the resonances of water molecules.

4.1 Experiment

The THz field is generated using optical rectification in a lithium niobate crystal with the tilted-pulse-front technique [26]. The details of the generation and detection process have been explained earlier in Chapter 2. However, here, we show the experimental setup to locate the vapour cell and THz polarizers. Ideally, we would like to locate the polarizers in a place where the transmitting THz beam is collimated. However, for this experiment, we locate them before the second parabolic mirror, where the THz beam is diverging. This should not cause any problems with the quality of the beam as these polarizers are free-standing wire grids. The experiment is performed in collaboration with Dr. Murat Yildirim. It can be seen from Fig. 4.1 that the vapour cell between the parabolic mirrors where THz beam is collimated. This choice is made to avoid saturation of the optical nonlinearity due to the intense THz beam and also to simplify the modeling of the Kerr coefficient n_2. Moreover, a pair of free-standing wire-grid polarizers is used after the first parabolic mirror to control the intensity of the THz beam.

We estimate the maximum peak value of the THz electric field to be $\approx$ 2.7 kV/cm at the location of the vapour cell.

4.1.1 Water vapour cell

The water vapour cell is a cylinder with a length of 8 cm and a diameter of 5.5 cm. To avoid absorption and reflection of the THz field, ultra-thin cling wraps are used as the windows of the cell [103] (See Fig. 4.2). The vapour cell is placed in the collimated arm of the THz field and filled with dry nitrogen under atmospheric pressure. A few drops of

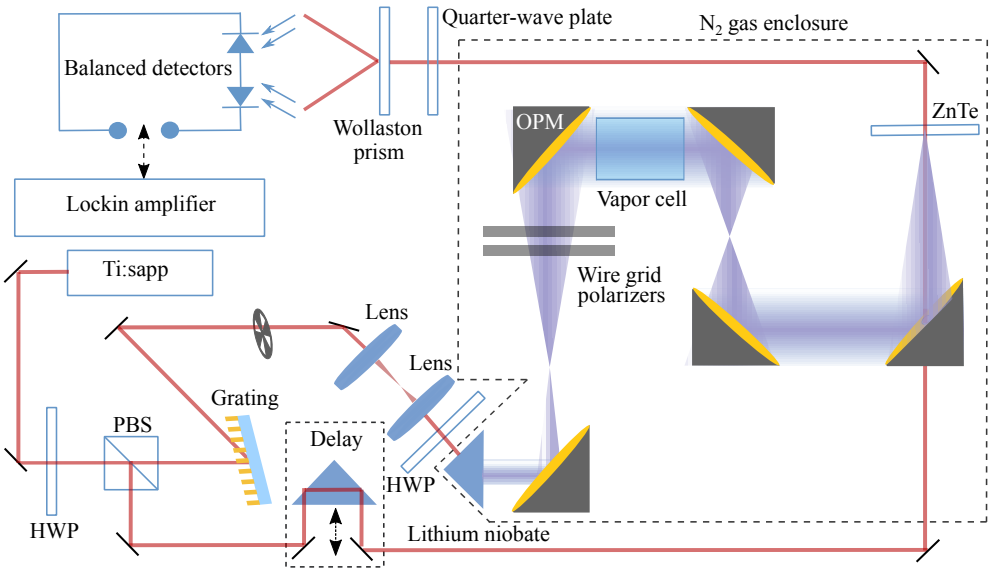

Figure 4.1: Experimental setup diagram for THz generation and detection. The vapour cell is placed between two parabolic mirrors where the THz beam is collimated. A half-wave plate (HWP) and a polarizing beam splitter (PBS) are used to split the pump and probe beams. OPM is off-axis parabolic mirror.

distilled water are placed inside the cell provide the required water vapour. We make sure the cell is sealed properly. A heating wire wrapped around the cell and a thermocouple are used to keep the temperature of the vapour cell at $T = 309^{\circ}$ K. To determine the effect of water vapour on the transmitted field, we collect the data with and without the water vapour. We repeat the measurements at different THz powers by rotating the first polarizer while keeping the second one fixed to maintain a constant polarization state. Isolation tape is wrapped on both sides of the cylinder to limit heat transfer to the middle of the cell. This way, we avoid condensation on both facets of the cell.

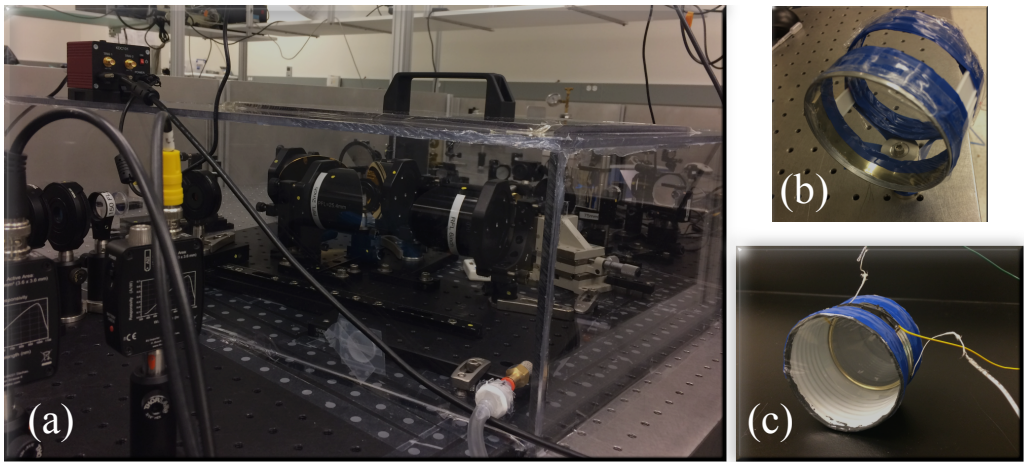

Figure 4.2: (a) A view of the experimental setup with N_2 enclosure. (b) The vapour cell cling wrap facets and defect side wall to allow nitrogen purging. This cell is used to collect empty cell measurements. (c) The actual vapour cell with cling wraps on the facets.

4.2 Theoretical model

For this study, we focused our attention on the spectral region between 1 and 1.5 THz where water vapour exhibits six strong resonances and where our THz system features optimal signal-to-noise ratio. The theory part is done in collaboration with Dr. Akbar Safari. The linear susceptibility of the vapour due to these six resonances is given by

$$\chi = \chi_R + i\,\chi_I = \sum_{j=1}^{6} \frac{c^2}{2\,\pi^2\,\nu_j}\,\frac{\nu_j - \nu + i\,\gamma_j}{\gamma_j^2 + (\nu_j - \nu)^2}\,n_w\,S_j, \tag{4.1}$$

where c is the speed of light in cm/s, $n_w = 1.389 \times 10^{18}$ cm^{-3} is the number density of the water molecules and ν_j is the resonant frequency of the jth transition. The linewidth of

each transition depends on the temperature T according to

$$\gamma_j = c\left(\frac{296}{T}\right)^{a_j}\left(\gamma_s P_w + \gamma_f P_f\right), \tag{4.2}$$

where a_j is the temperature exponent for the air broadening, and P_w and P_f are the partial pressures of the water vapour and the nitrogen gas in the cell. The self-broadening and foreign gas broadening coefficients of these six transitions are approximately the same and are found to be $\gamma_s = 0.5$ and $\gamma_f = 0.1$ cm^{-1} atm.$^{-1}$, respectively. The required parameters are extracted from HITRAN database [104] and [105] and are listed in Table 4.1.

j	ν_j (THz)	a_j	γ_j (GHz)	A_j (s^{-1})	g_j''	$S_j \times 10^{20}$ (cm/molecule)
1	1.0974	0.78	3.91	0.0164	21	15.18
2	1.1133	0.79	3.40	0.0184	3	4.521
3	1.1629	0.78	3.70	0.0227	21	16.67
4	1.2076	0.81	3.49	0.0283	9	5.308
5	1.2288	0.76	3.73	0.0187	5	4.421
6	1.4106	0.80	3.70	0.0426	33	13.87

Table 4.1: Transition parameters of the six strongest resonances of water vapour molecules in the spectral range between 1 and 1.5 THz. The vapour cell is at $T = 309^\circ$K and contains one atmosphere of nitrogen gas. ν_j and γ_j are the central frequency and the linewidth, a_j is the air broadening exponent, A_j is the Einstein A coefficient, g_j'' is the degeneracy factor of the excited state, and S_j is the spectral line intensity of the jth transition.

The spectral line intensity for each transition S_j is a function of temperature. In thermodynamic equilibrium, the population distribution between the energy levels is governed by Boltzman statistics and changes with temperature. Therefore, the spectral

line intensity for each transition can be calculated from

$$S_j = \frac{A_j\, c}{8\,\pi\, \nu_j^2}\, \frac{g_j''\, e^{-h\nu_j/k_BT}\left(1 - e^{-h\nu_j/k_BT}\right)}{\sum_k g_k\, e^{-h\nu_j/k_BT}}, \tag{4.3}$$

where A_j is the Einstein A coefficient and g_j'' is the degeneracy factor of the excited state (Table 4.1). h and k_B are Planck and Boltzman constants, respectively. The sum in the denominator of Eq. (4.3) represents the total internal partition sum and can be found in HITRAN database for water molecules [104]. The last column of Table 4.1 shows the spectral line intensities at $T = 309^\circ$ K calculated from Eq. (4.3).

4.3 Results and discussion

Figure 4.3 (a) shows the time-domain signals for the lowest THz amplitude corresponding to 162 V/cm, where a linear response of water vapour is expected. The effect of the sharp resonances of the water vapour appears as the trailing oscillations due to the free induction decay of the resonances. A long scan time of 155 ps is used during the measurements in order to collect as much spectral information as possible. The spectral density of the THz field is shown in Fig. 4.3 (b) where the fast Fourier transform (FFT) of the temporal shape is displayed. The zero-padding technique [106] is applied on the temporal signal to achieve a smoother interpolation in the frequency domain.

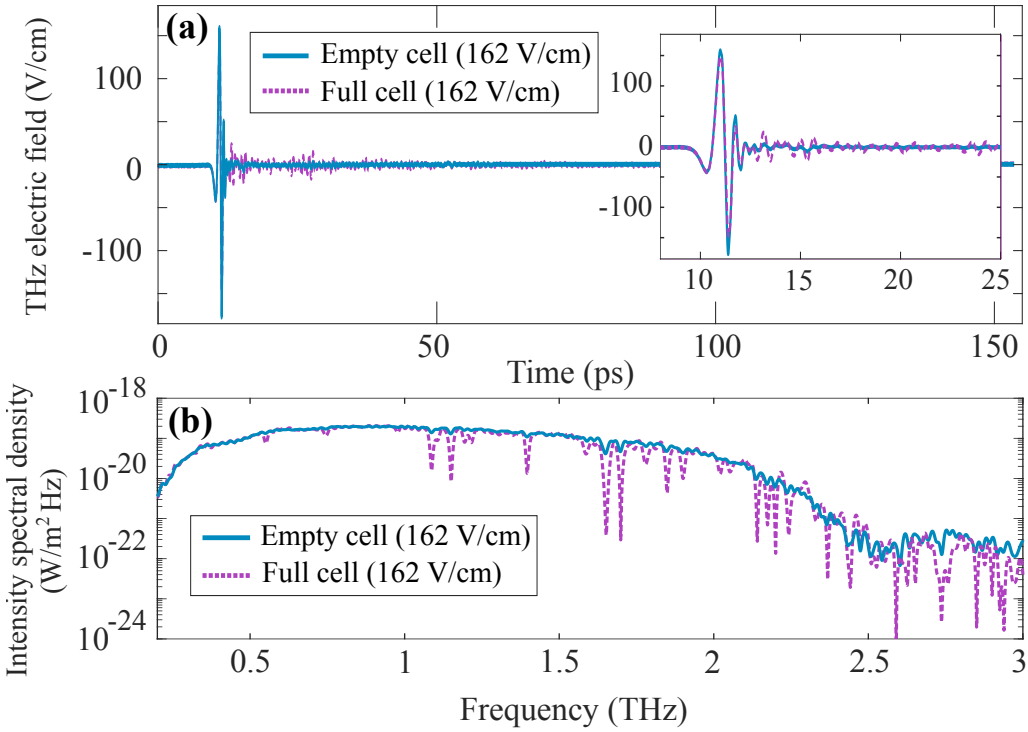

Figure 4.3: (a) THz field plotted as a function of time with and without water vapour; these plots show the transient response of the overall system. The dashed line shows the THz electric fields in the presence of the water vapour, while the solid line shows the reference signals collected in the absence of the vapour. The inset in (a) enlarges the main peaks and the trailing oscillations. (b) Intensity spectral density with and without water vapour obtained from Fourier transform of the time-domain signals. THz spectrum extends to 2.5 THz, but we focus on the resonances between 1 and 1.5 THz where the signal-to-noise ratio of the source is maximum.

4.3.1 Absorption coefficient

In Fig. 4.4, we plot the calculated (linear response) and experimentally measured absorption coefficients. The experimental absorption curves were calculated based on the intensity spectral densities of the THz signals with different field intensities. We notice that for the lowest intensity signal, the absorption coefficient fits well with the linear theoretical

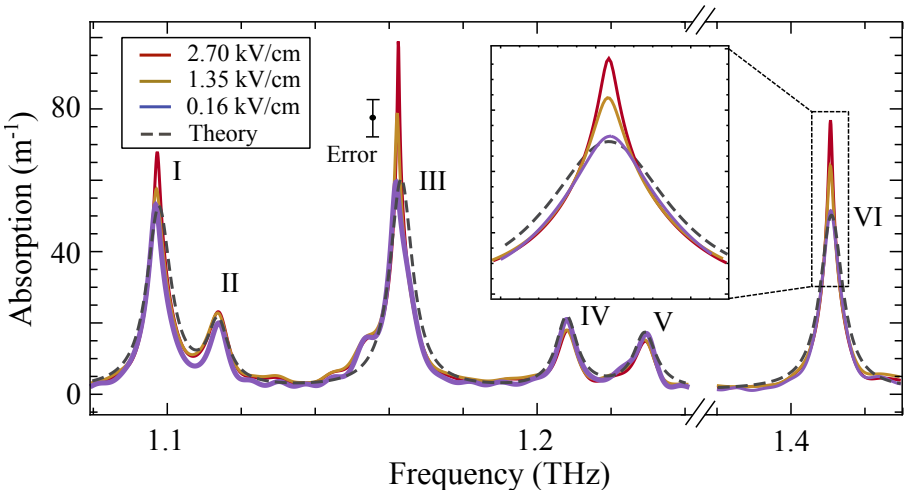

Figure 4.4: Absorption coefficient of water vapour at temperature $T = 309°$ K. The absorption peaks are numbered from I to VI, and the corresponding labels are shown next to each peak. While the absorption of the lowest-intensity signals fits well with the linear model, the absorption at some resonances increases with increasing the intensity.

model. However, as the strength of the field increases, there is a consistent increase in the absorption at the location of the resonances I, III and VI. This change is an indication of the nonlinear process associated with multi-photon transitions and optical pumping.

4.3.2 Time-domain analysis

The same effect can be seen in the time domain as well. In Fig. 4.5, we plot the integrated values

$$A_i(t) = \frac{\int_0^t |E_i(t)|^2 dt}{\int_0^\infty |E_{i,0}(t)|^2 dt}, \tag{4.4}$$

where $E_i(t)$ is the electric field at each intensity level i in the presence of the vapour and $E_{i,0}(t)$ is the electric field at each intensity level i in the absence of the vapour. In order to

compare the data at different signal intensities, we normalize the curves to unity. Since the area under the $A(t)$ profile is inversely proportional to the absorption, we can compare the absorption of THz signals with different intensity levels in time by looking at the $A(t)$ curves.

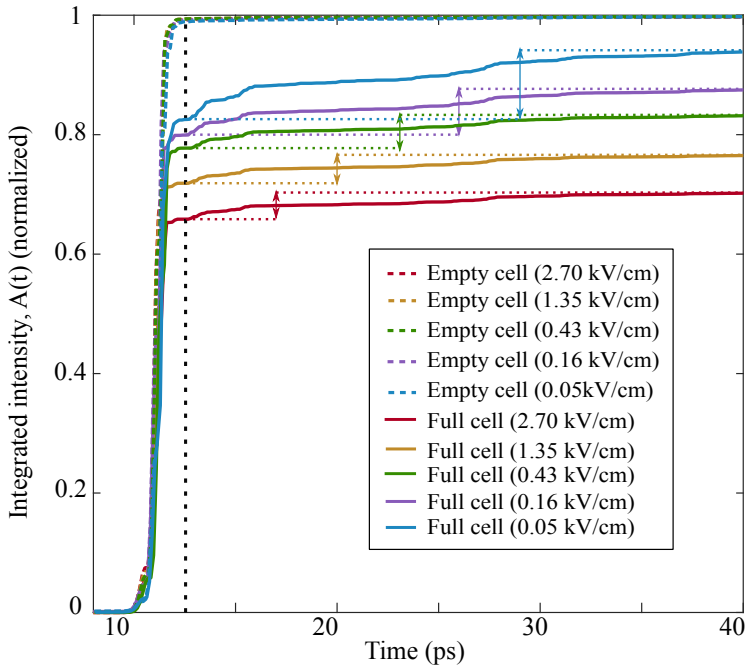

Figure 4.5: Temporal verification of the reverse saturable absorption. Unlike the "no water vapour" case (dashed lines), the solid lines end up at lower values for higher-intensity fields which is due to the nonlinear absorption of the water vapour molecules.

Fig. 4.5 shows the integrated THz intensity, collected at the output of the cell, plotted as a function of time. The dashed lines show the characteristics for the empty cell with no vapour in it, obtained for various values of the applied THz field (see the legend). The solid lines show the corresponding characteristics for the cell with maximum water vapour concentration at different strengths of the applied THz field. One can see two distinct effects exhibited by these results. First, there is a sharp increase in the integrated signal $A(t)$

at 11.1 ps, which corresponds to the peak of the applied THz field, shown in Fig. 4.3 (a). In principle, we would expect all the reference signals (the cell with no vapour) to approach a fixed value after the rapid jump around the peak time. The dashed lines (reference characteristics) follow this expectation. The solid lines, representing the data collected in the presence of the water vapour, show the same behaviour, except that they tend to reach their maximum values more slowly than their corresponding reference counterparts. This result shows that the water vapour molecules display a non-instantaneous response to the THz field.

Second, a strong power dependence can be seen in the integrated signals in the presence of the water vapour. As we increase the THz intensity, the difference between the two signals (with and without vapour) becomes larger. We attribute this behaviour to the nonlinear response of the water vapour molecules under the intense THz radiation. The vertical arrows in the figure show the difference in the values of the parameter A at the initial moment when the peak of the THz pulse ends (vertical black dotted line in Fig. 4.5) and at the final moment where the electric field vanishes and A approaches a constant value. The area under the field profile is smaller for higher-intensity pulses (see the change in the length of the arrows), which indicates reverse saturable absorption. This is an interesting observation which verifies the nonlinear response of vapour molecules observed in the frequency domain (see Fig. 4.4).

4.3.3 Energy levels

With a two-level-system approximation, one expects to see saturation of the transition, and thus, a decrease in absorption as the intensity increases. However, Fig. 4.4 clearly shows

that absorption of water molecules at some resonances increases with intensity, which indicates that two-level approximation is not valid here. In Fig. 4.6, we plot the rotational energy levels of water molecules relevant to the six transitions in our study. The blue

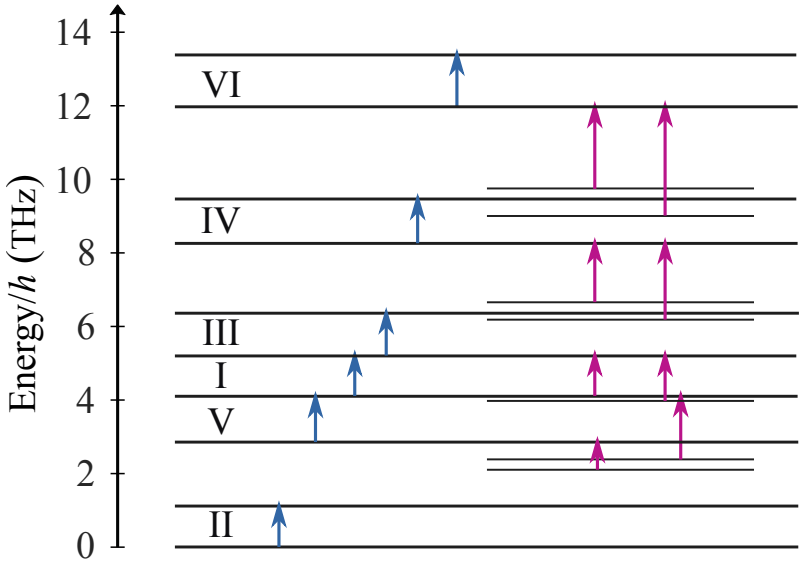

Figure 4.6: Energy level diagrams for the rotational transitions of water vapour where the lower and upper states of each transition under study is shown. The shorter lines on the right show the degenerate states at which an upper state of one transition coincides with the lower state of some other transition. Except for the second resonance, where the lower energy state coincides with the ground state, there is at least one degenerate transition for other resonances that pump the main transition.

arrows show the transitions corresponding the the six resonances shown in Fig. 4.4. As can be seen, the transition V populates the ground state of transition I, which consecutively, populates the ground state of transition III. Therefore, a large increase in the absorption of the third transition is expected as its ground state population increases with THz field intensity. Moreover, the THz field has a broad spectrum covering the frequency window from 0 to 3 THz which excites many other transitions as can be seen in Fig 4.3(b). The excited state of some of these transitions are indeed the ground state of one of the six

transitions in our study. These transitions are shown by the pink arrows in Fig. 4.6. For example, the ground state of the sixth transition is pumped by two other transitions at 2.2 THz and 2.97 THz.

4.3.4 Nonlinear refractive index

Furthermore, since we use a coherent detection technique, we are able to retrieve the spectral phase information of the THz field from the Fourier analysis. Fig. 4.7 shows the phase of the THz field after the vapour cell as a function of frequency. It can be seen from

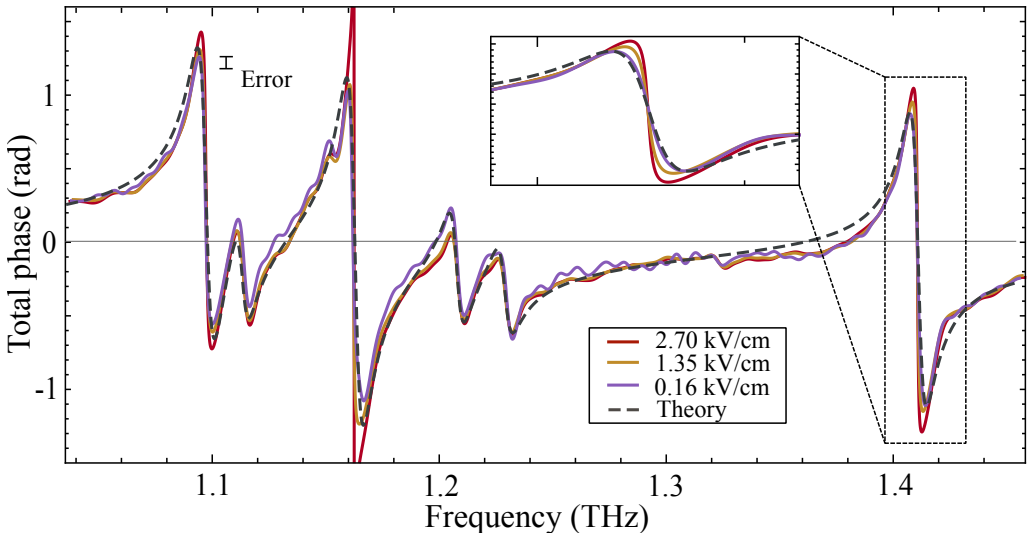

Figure 4.7: Overall phase of the transmitted THz field, including linear and nonlinear contributions, as a function of frequency. As the intensity of the field increases, the swings in the phase in the vicinity of the resonances become more pronounced. The inset magnifies the phase for the resonance at 1.4 THz.

the graph that the theoretical linear model fits well with the phase of the lowest-intensity signal, which is expected to be linear. Nonlinear response of the material can be found

where the higher-intensity signal acquires additional phase shift, specifically, at the location of the water vapour resonances. This nonlinear phase shift can be understood again from multi-photon transitions and pumping of the ground states by the broadband THz pulse, as explained earlier.

By subtracting the phase of the lowest-intensity signal from those of the higher-intensity signals, we find the induced nonlinear phase shift $\Delta\phi$ of the THz field. Then, the nonlinear change in the refractive index can be calculated from [17]

$$\Delta n = \frac{\Delta\phi}{kL}, \tag{4.5}$$

where L is the length of the cell and k is the wavenumber. This change in the refractive index is shown for the last resonance in the top inset of Fig. 4.8.

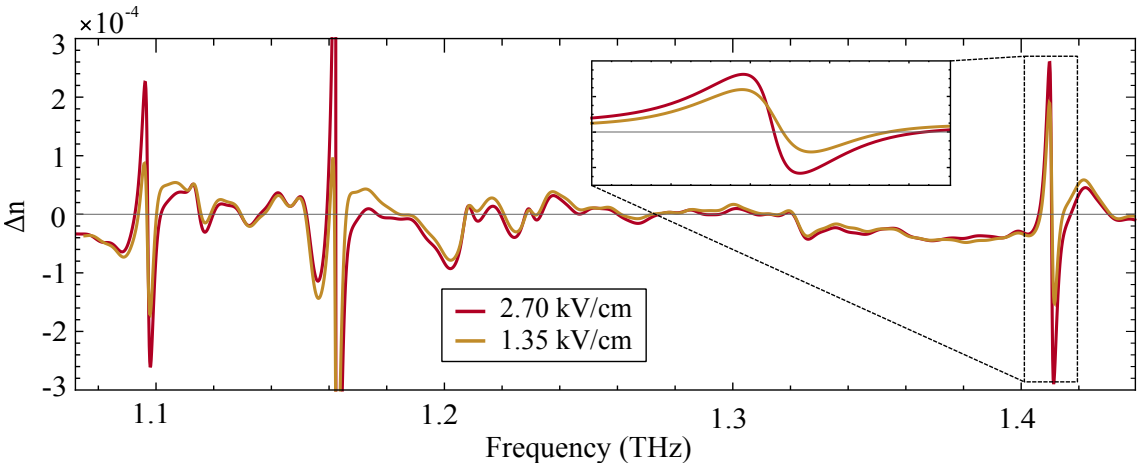

Figure 4.8: The refractive index change (Δn) as a function of frequency. As the intensity of the field increases, the swings in the refractive index change in the vicinity of the resonances become more pronounced. The inset magnifies the amount of the refractive index change for the resonance at 1.4 THz.

To the lowest order of approximation, the nonlinear change in the refractive index is often modeled by $\Delta n = n_2 I$, where I is the intensity of the field and n_2 is called the optical Kerr coefficient or nonlinear refractive index. However, in our work, Δn arises from multi-photon transitions for which the spectral intensity of the THz field varies [see Fig. 4.3(b)]. Thus, one cannot assign a single intensity to each resonance that contributes to Δn independently. Therefore, the nonlinear response of the vapour cannot be characterized by a simple Kerr coefficient, unambiguously. Nevertheless, if we consider the maximum spectral density for each resonance, we find a maximum intensity in a linewidth of the resonances to be around 10^{-6} W/m^2, and thus, we can estimate a minimum Kerr coefficient of the order of 100 m^2/W [107].

4.4 Conclusion

In conclusion, we observed an extremely large nonlinear response of water vapour in the THz regime. We attribute this large nonlinearity to optical pumping and multi-photon transitions in water molecules. Time-domain spectroscopy has been used widely to measure the absorption spectrum of water vapour in the THz regime. However, our results show that optical pumping can modify the observed spectrum even at intensities far below the saturation intensity of the transitions. A primary obstacle to many THz applications is the attenuation of the field by water vapour in the atmosphere. A naïve approach to overcome this problem is to increase the THz intensity to saturate the transition and reduce the absorption. However, our study shows that, as the intensity increases, the absorption of many resonant lines increases as well. Moreover, nonlinear spectroscopy provides valuable

information on the transitions and the energy levels of the molecules. Thus, our work paves the way for a better understanding of water vapour molecular structure, to validate the rotational energy levels of water molecules and to study the role of water clusters in the absorption spectrum [108–112].

5. THz Nonlinear Optical Response of Solids

With recent developments in coherent THz radiation sources, THz pulses with higher intensities are becoming routinely accessible [25]. As a consequence, THz science has been growing with studying the nonlinear response of different materials in the THz region of the spectrum. For instance, the nonlinear response of free electrons to an intense single-cycle THz pulse was reported in [40]. Also, THz-induced carrier multiplication via impact ionization was shown in [41–43], and THz saturable absorption and higher-harmonic generation by hot electrons were demonstrated in [44–49]. Moreover, it has been shown that a phonon-induced THz Kerr effect can result in a larger nonlinear refractive index (n_2) than that of the optical Kerr effect [25, 38, 113]. Such large nonlinearities have been measured in semiconductors as well as other solids and liquids [44, 45, 114–116].

In this Chapter, we report on the nonlinear response of solids in the THz frequencies. We select the samples with different structures (crystalline or amorphous) and various refractive indices. The goal of this Chapter is to study their nonlinear optical responses using a time-domain characterization approach.

5.1 Experiment

The THz field is generated using optical rectification in a lithium niobate crystal with the tilted-pulse-front technique [26]. The details of the generation and detection process have been explained earlier in Chapter 2. However, here, we show the experimental setup to locate the sample and THz polarizers. The experiment is performed together with Dr. Murat Yildirim.

Fig. 5.1 shows the experimental setup where the THz polarizers are placed in front of the collimated beam to control the intensity of the beam at the focal point where the sample is located. In order to determine the material's response to the transmitted field,

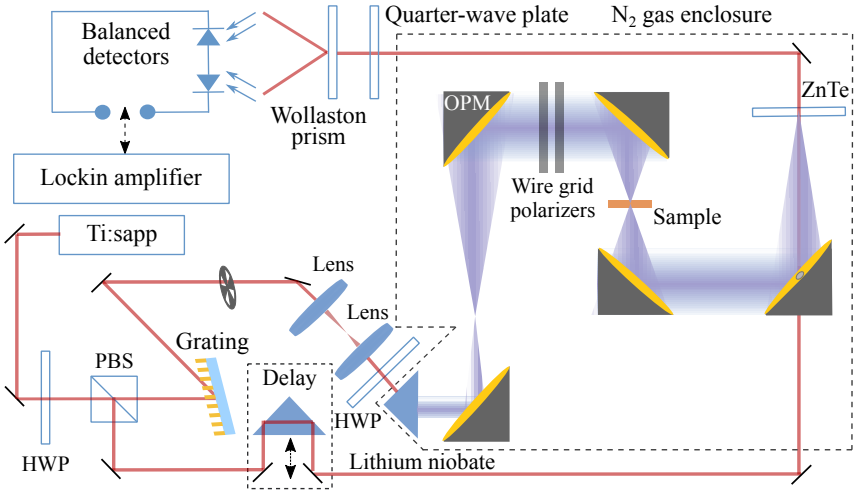

Figure 5.1: Experimental setup diagram for THz generation and detection. The polarizers are placed between two parabolic mirrors where the THz beam is collimated. A half-wave plate (HWP) and a polarizing beam splitter (PBS) are used to split the pump and probe beams. OPM is off-axis parabolic mirror.

we collect the data with and without the sample in place. We repeat the measurements at different THz field amplitudes by rotating the first polarizer while keeping the second one

fixed to maintain a constant polarization state. This way, we can control the intensity of the THz beam without introducing dispersion to the transmitted field.

5.2 Results and discussion

5.2.1 Time-domain analysis

THz electric fields at different intensity levels in time and frequency domains are shown in Fig. 5.2(a) and (b), respectively. Also, the normalized time-domain electric fields are shown in Fig. 5.2(c) to make sure no dispersion is introduced to the fields by rotating the THz polarizer. We measure the peak fields for different angles of the THz polarizer, as shown in Fig. 5.2(d). Based on the results of this figure, we calculate the intensity extinction ratio of the THz polarizers to be ≈ 1000. However, for the angles where transmission is less than 10%, the shape of the field changes, which is undesirable, and we avoided those angular settings in our experiment.

We tested five different materials for their nonlinear optical responses. These samples are crystalline quartz, calcium floride (CaF_2), magnesium fluoride (MgF_2), zinc selenide (ZnSe), and BK7 glass. Quartz is a hard, crystalline mineral composed of silicon and oxygen atoms. Its chemical formula is SiO_2, and it is the second most abundant mineral in the Earth's continental crust, behind feldspar. Its crystalline structure belongs to the trigonal crystalline structures. Calcium fluoride and magnesium fluoride are inorganic compounds with cubic and tetragonal crystal systems, respectively. Zinc selenide is an intrinsic semiconductor with the zincblende crystalline structure, and finally, BK7 is a borosilicate glass with an amorphous structure. Among these materials, BK7 shows the strongest

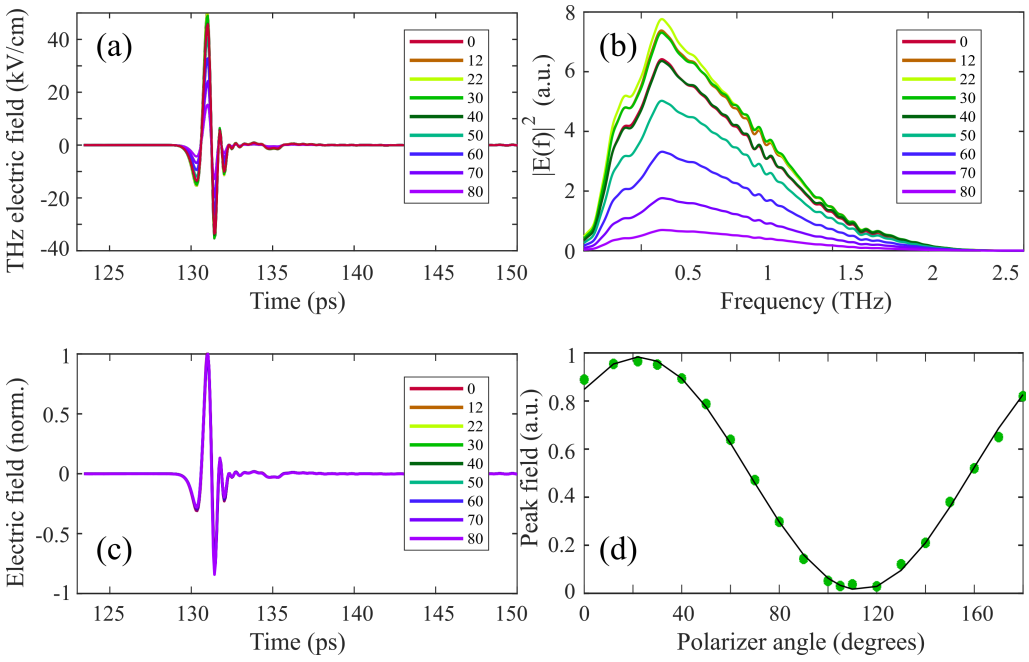

Figure 5.2: (a) THz fields plotted as a function of time at different peak amplitudes provided by a pair of THz polarizers. (b) shows the THz power spectrum obtained from the Fourier transform of the time-domain signals of part (a). The normalized profiles of the free space fields at different field intensities are shown in (c) where the pulse experiences negligible distortion or delay. A trace of the peak values of the fields measured for different polarizer angles is shown in (d) where a cosine function fits the measured points.

linear absorption peak centered at 1.2 THz [117]. This strong absorption can be justified by the presence of ionic network modifiers in BK7 glasses. Ionic network modifiers are the components that break up and modify the structure of the glass network [117, 118]. Also, since ionic polarizability contributes to the dielectric constant of glasses at THz frequencies and below [117], the THz refractive index of BK7 glass is higher than its refractive index at the visible and near-infrared. We would expect to see the transmitted electric fields of different shapes due to the difference in the thicknesses and refractive

indices of our samples. Fig. 5.3 shows the dispersion induced time broadening of the transmitted THz pulses. In Fig. 5.3, we have normalized the peak field values to unity and

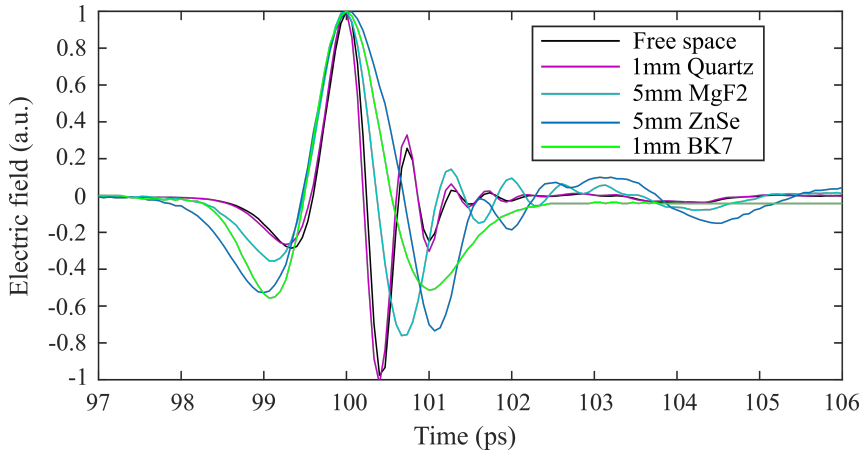

Figure 5.3: Distortion of the THz pulses as they transmit through different samples. The black line is the reference signal obtained when there is no sample (free space).

have placed the peak values at the same time so that we can compare the time duration of the pulses. It can be seen from Fig. 5.3 that the THz pulse has its minimum duration when there is no sample in place (free space), while BK7 introduces the strongest broadening.

We performed the experiment by letting THz pulses at different intensities to pass through the samples, and calculated the amount of delay introduced by the samples to the electric fields as the field intensity increased. Fig. 5.4 shows the overall response of different samples at different intensities. In this figure, we show the average delay of each field at their rising and falling lobes with respect to the THz field with the minimum amplitude (20 kV/cm). As can be seen in Fig. 5.4, the amounts of delay of the free space fields of different intensity levels locate around zero. However, the amounts of delay of the fields transmitting through some of the samples increase as the field intensity rises.

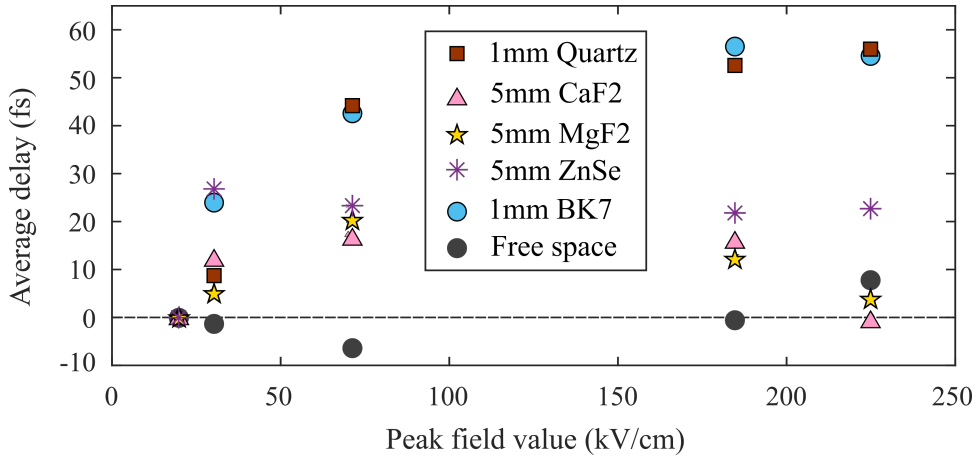

Figure 5.4: Average delay of the THz signals as the field intensity increases. The data represent the optical response of different materials. The free space data fluctuate around the zero line. The deviations of the free space average delay reflect the amount of measurement error.

We attribute this behavior to the nonlinear optical response of these materials at the THz frequencies. This response is more pronounced for quartz and BK7. Hence, we limit our study to these two materials. It can also be seen that after certain peak field values, the nonlinear responses of these material media, which result in higher average delays of the THz pulses, get saturated. For some of the other samples (CaF_2, MgF_2 and ZnSe), the amount of the average delay is not significant, and we do not proceed with further spectral analysis of these samples. Detailed data analysis for different samples to find the best material candidates is done in collaboration with Soheil Zibod.

We plot the transmitted fields for quartz and BK7 in Fig. 5.5. We can observe time shifts of the pulses as the peak field increases. The pulses with higher intensity tend to arrive later (in time). Fig. 5.5(a) and (b) show the transmitted electric fields for quartz and BK7, respectively. We can see that the fields shown in Fig. 5.5(b) that transmit through

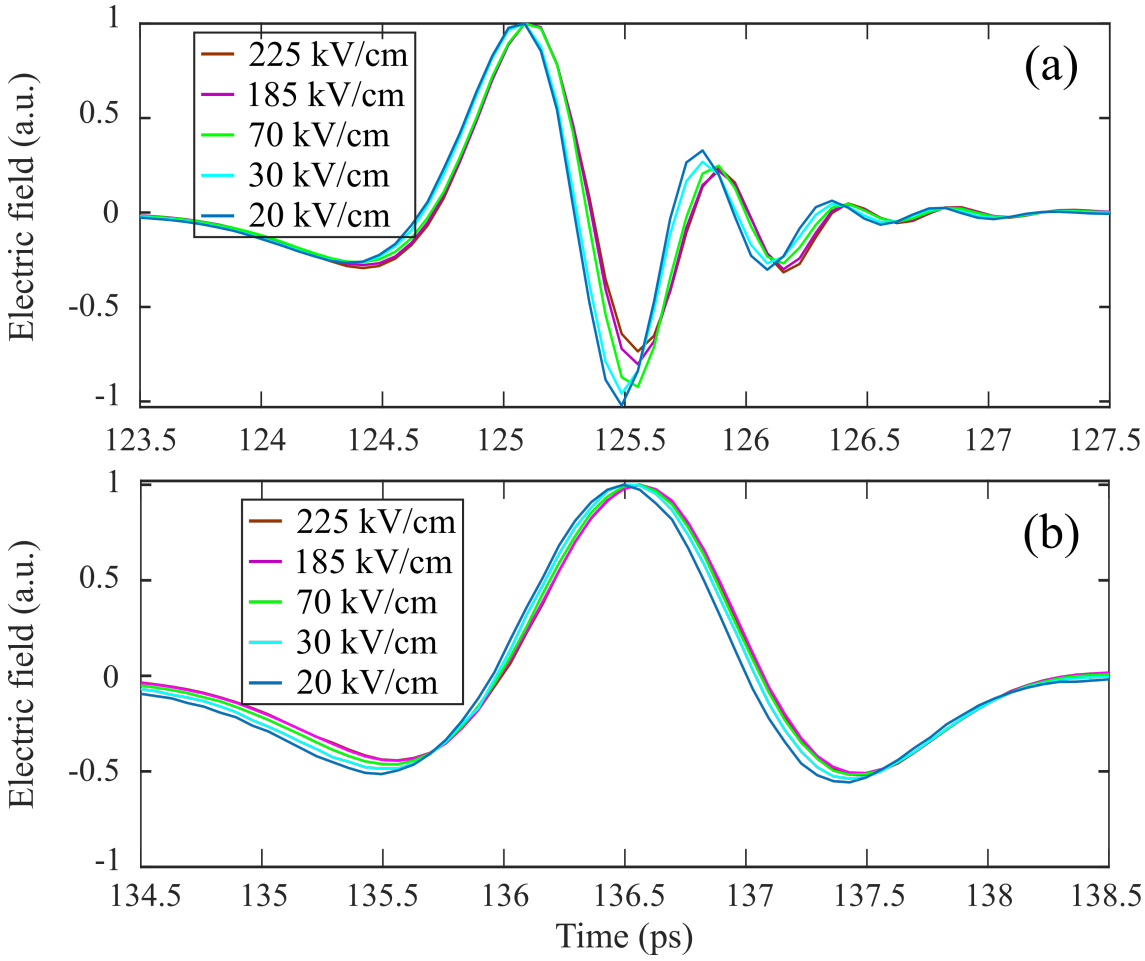

Figure 5.5: THz electric field transients in time-domain. (a) shows the electric fields at different intensity levels transmitted through Z-cut quartz. The polarization of the THz beam is linear and is aligned with the optic axis of the crystal. (b) shows the electric fields at different intensity levels transmitted through BK7. In both cases, as the intensity increases, the fields tend to arrive later (in time).

BK7 undergo more time broadening than the fields of quartz shown in Fig. 5.5(a). This is due to the stronger dispersion of BK7 at these frequencies. We can also see that the higher frequency components which tend to locate at the trailing edge of the pulse vanish for the

fields that transmit through BK7 (see Fig. 5.5(a)-(b)). This observation can be verified in the frequency domain.

5.2.2 Spectral intensity and phase

The power spectrum of the fields $\left(|E(\mathrm{f})|^2\right)$ is shown in Fig. 5.6. They are obtained from the fast Fourier transform (FFT) of the time-domain field transients given in the last part. Fig. 5.6(a) and (b) show the power spectrum for quartz and BK7, respectively. We notice

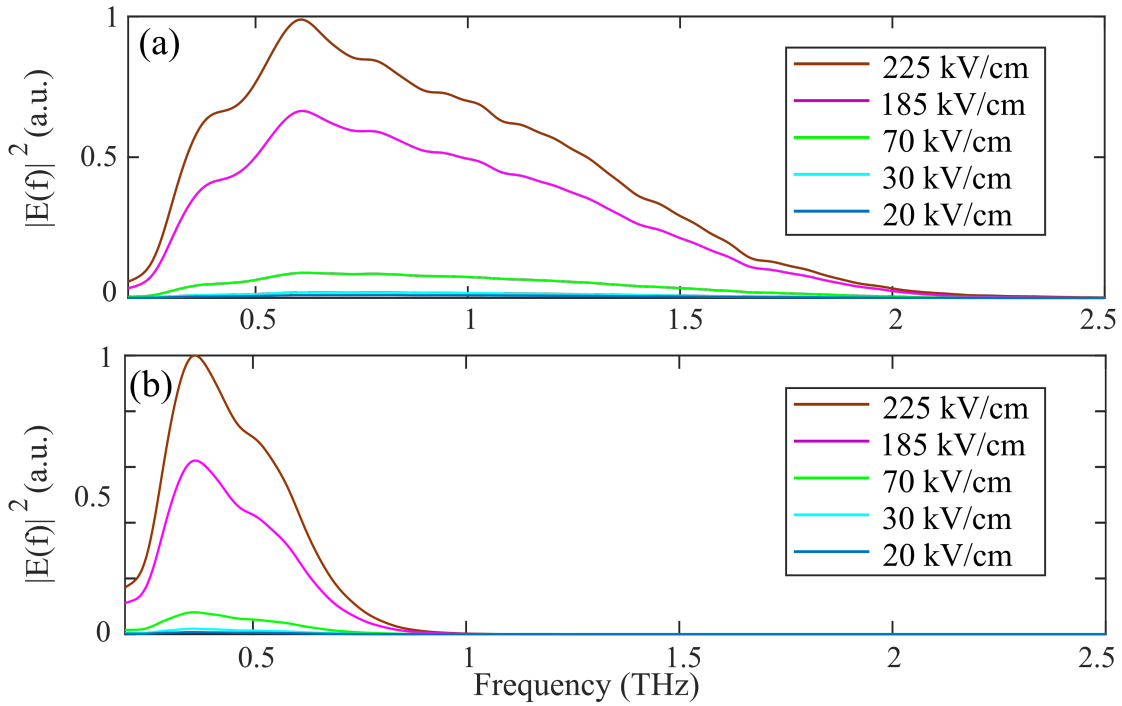

Figure 5.6: Power spectrum of the transmitted pulses through (a) quartz and (b) BK7.

that in the case of BK7, the spectrum shrank considerably. A similar observation is reported in [117].

We can find the phase of the signals from their complex Fourier components as we measure the electric fields. By subtracting the phase of the lower-intensity signal from the phase of the higher intensity signals, we can find the net accumulated nonlinear phase shifts. Fig. 5.7 shows the phase shifts of the field as its intensity level rises. Fig. 5.7(a)

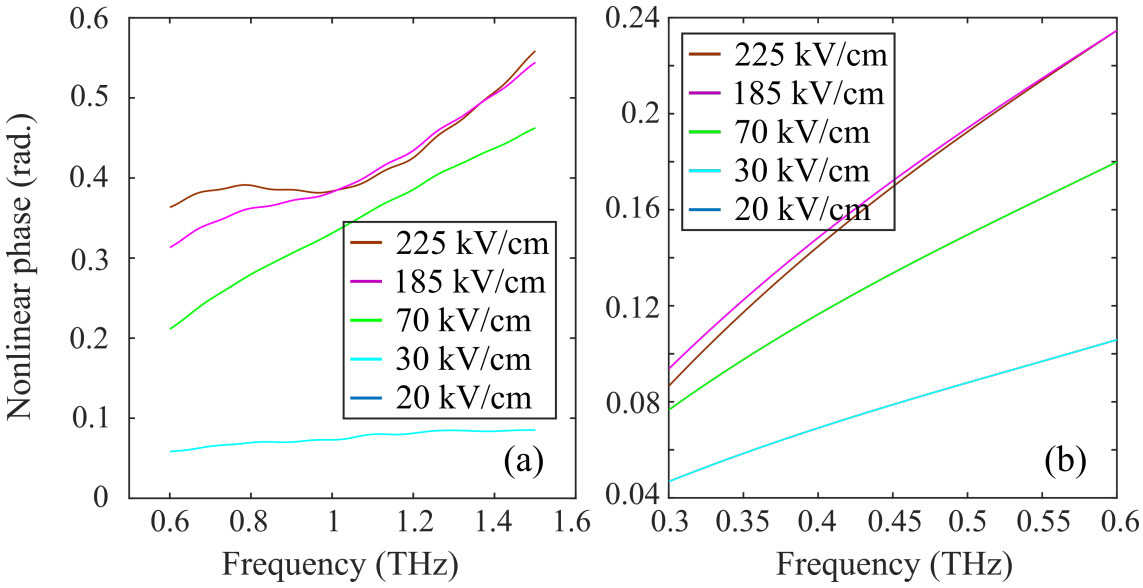

Figure 5.7: Dispersion of the nonlinear phase shift introduced to the THz fields transmitted through (a) quartz and (b) BK7.

shows the phase shift of the THz pulse transmitted through quartz at different intensity levels. There is an increase in the slope of the curves as the intensity increases. The same behavior is seen in Fig. 5.7(b) for BK7. In the latter, the phase shifts are found to be smaller than the phase shifts in quartz.

5.2.3 Nonlinear refractive index

In order to calculate the nonlinear refractive index, we first find the intensity of the pulse. The spectral density of the pulse is found according to

$$I = \frac{1}{2}\, n_0\, \varepsilon_0\, c_0\, |E|^2, \tag{5.1}$$

where ε_0 is vacuum permittivity, c_0 is the speed of light in vacuum, and n_0 is the linear refractive index of the material. FFT provides the shape of the spectral density in arbitrary units. However, in order to find the actual values of the FFT, we apply Parseval's theorem to re-scale the FFT values and hence we find the spectral density in the actual unit of $\mathrm{W/m^2\,Hz}$. The area under the curve of spectral density as a function of frequency provides the intensity. We note that in this case, unlike in the case of the water vapour, we deal with broad resonances. Water vapour has sharp resonances, which allow us to distinguish the effect of water vapour from any other background effects. In the case of solids, we would not expect to see sharp resonances in the frequency domain, and therefore it is not easy to distinguish the effect of high power THz pulses on the material response. Fortunately, in this technique, we only care about the change in the phase signals, and assuming that the background effect is not nonlinear, any artifact will be canceled out by subtracting the phase of the minimum intensity signal. We have verified this assumption in water vapour, and we found it to be a valid assumption. Next, we obtain the dispersion of the nonlinear refractive index using the spectral intensity and the nonlinear phase curves according to

$$n_2 = \frac{\Delta\phi}{I\,k\,L}, \tag{5.2}$$

where $\Delta\phi$ is the nonlinear phase shift as a function of frequency that can be obtained from Fig. 5.7, k is the wavenumber and L is the thickness of the sample. The dispersion profile of n_2 is given in Fig. 5.8 for both quartz and BK7. The error bars are the standard deviation of the average n_2 values obtained from the signals at different intensity levels and also from repeating the measurements at the same intensity. It can be seen that the value of the

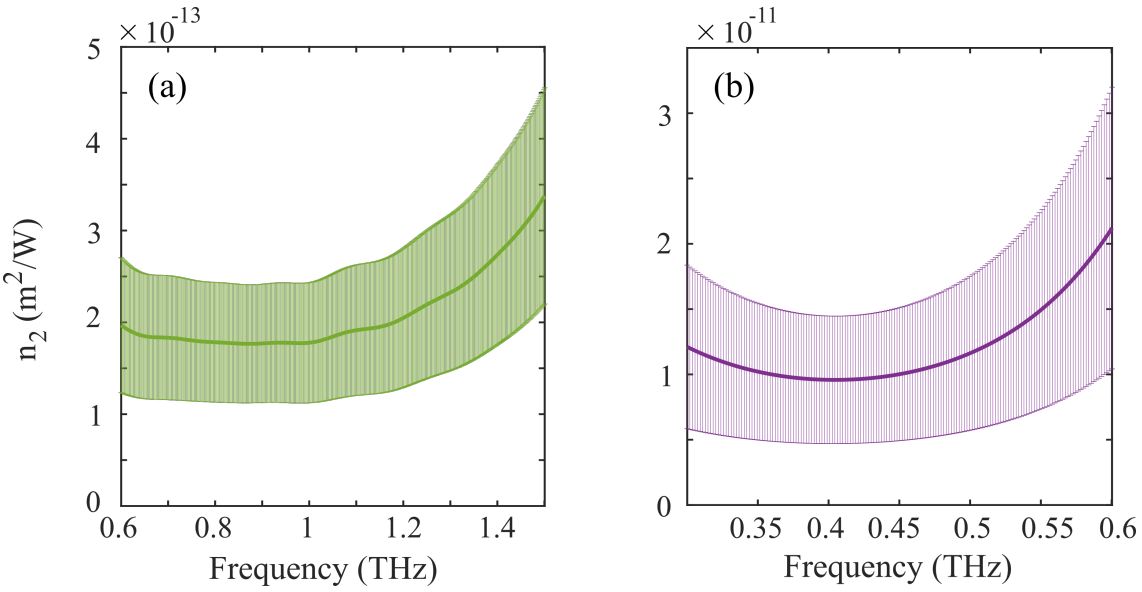

Figure 5.8: Dispersion of the nonlinear refractive index in (a) quartz and (b) BK7. The error bar is standard deviation of the mean.

nonlinear refractive index of quartz [Fig. 5.8(a)] is two orders of magnitudes smaller than the nonlinear refractive index of BK7 [Fig. 5.8(b)]. Compared to the predicted value in [38] for crystalline quartz, the value of n_2 is found to be two orders of magnitude larger. This could be due to the assumptions the authors have made in their calculations. They assume their THz radiation is quasimonochromatic. However, in our case, we have a short pulse of THz, where its power spectrum extends from 0.1 to 2.5 THz. Therefore the nature

of the nonlinear phenomena is clearly different from the case reported in [38].

5.3 Conclusion

In conclusion, we perform nonlinear THz-TDS measurements to obtain dispersion of the Kerr coefficient of some candidate materials. Our developed technique is based on time-domain field extraction and works with both amplitude and phase of the signals. This temporal technique has been used in place of the spatial z-scan technique, which is the most common technique for n_2 extraction in the visible frequency range. We select two good material candidates, among others, based on their promising time-domain delay responses (Fig. 5.4). We perform frequency-domain analysis to obtain the Kerr coefficients from their spectral phase and intensity information. The value of n_2 is large in their given frequency interval, which is limited to the frequency content of the input pulse as well as the spectral response of each material. We assign this large nonlinear response to the vibrational contribution to n_2, the phonon modes, as well as the local vibrational modes of impurities, which are all expected to contribute to the value of the Kerr coefficient. The observed time-domain delay responses are consistent with the modeling results shown in Chapter 3. In Chapter 3, we observed a delay of around 4 ps and 0.5 ps between the linearly and the nonlinearly propagating THz pulses in Si and ZnSe, respectively (see Fig. 3.3 and Fig. 3.4). In the experiment, we confirmed that the average delay introduced to the THz pulses transmitting through the samples depends on their structure and dispersion behavior, and is varying between 20 to 60 fs (see Fig. 5.4) for the refractive index change of $\Delta n \approx 10^{-3}$. This amount of delay is proportional to the delay of the pulses seen in the

modeling results, which are obtained for higher intensity level signals. This indicates the accuracy of the modeling results performed in Chapter 3.

6. Conclusions

THz radiation facilitates the observation of the time evolution of the Kerr effect on an ultrafast timescale. Hence, this relatively unexplored field of optical science creates an extremely useful environment that provides an insightful understanding of the polarizability dynamics of many material media [20, 33, 114]. This doctoral dissertation studies the nonlinear optical response of the water vapour as well as some solids at THz frequencies. It focuses on the response time of the third-order nonlinear processes of material media and presents interesting theoretical and experimental results that show the large effect of the slower lattice-driven processes in the strength of the overall third-order nonlinear optical processes at THz frequencies.

In this work, we first present a theoretical study to point out the importance of the linear (dispersion) as well as the nonlinear response time of material medium on the strength of the nonlinear optical process. Next, we proceed with the optical experiments to confirm the theoretical results. We develop a technique based on time-domain THz spectroscopy to measure the nonlinear response of transparent materials. Our experimental results indicate extremely large nonlinear optical responses of water vapor and some solids when compared to their nonlinear optical responses to the visible or the near-infrared

electromagnetic radiation. For the experiment, we use the optical rectification, as a second-order nonlinear process, to generate intense electric fields in lithium niobate using the titled-pulse-front technique. In the generation arm, an 800 nm Ti:sapphire laser beam pumps the lithium niobate. Also, we use a thin ZnTe crystal and electro-optic sampling to detect the THz electric field.

First, we theoretically study the propagation of broadband single-cycle THz pulses through a medium with both linear and nonlinear optical responses. Our theoretical model takes into account non-paraxial effects, self-focusing, and diffraction, as well as dispersion, in both the linear and nonlinear optical regimes. We confirm the role of non-instantaneous Kerr-type nonlinearity to the overall instantaneous and delayed Kerr effect during nonlinear light-matter interaction at the THz frequencies. Also, group-velocity dispersion turns out to be an important parameter in governing the efficiency of the nonlinear interactions. We also discuss the effect of linear dispersion on self-action effects during pulse propagation. Our study outlines important criteria in searching for a material with highly nonlinear optical behavior in the THz frequency range and can be used to interpret the THz-TDS measurement data by estimating the share of the electronic and vibrational contributions to the third-order nonlinear response.

Next, we use a time-domain THz spectroscopy technique to study the effect of the nonlinear interactions in water vapour on the shape of the transmitted electric fields. We noticed a strong nonlinear response at the location of the sharp resonances of water vapour, which appears as intensity-dependent oscillations at the trailing edge of the pulse. Water vapour pervades the atmosphere of the Earth, and due to its molecular rotations and vibrations, has several resonant vibro-rotational absorption lines in the THz range of

frequency. We developed a theoretical model to describe the nonlinear response of water molecules to a THz pulse excitation. Our experimental results are in good agreement with the theoretical model. Therefore, we can use our model to extract some fundamental parameters of the transitions.

Moreover, we studied the nonlinear response of some solids. Phonon resonances occur at THz frequencies, and we believe this molecular mechanism boosts the nonlinear optical interaction and results in a much larger Kerr coefficient as compared to the electronic Kerr coefficient in the visible and near-infrared range. We obtain the dispersion of the Kerr coefficient at the frequency range of the THz source. Our results indicate a large nonlinear refractive index for quartz, corresponding to a maximum refractive index change of $\Delta n = n_2 \times I = 10^{-4}$.

In summary, this doctoral work presented a study of the response time of the Kerr effect at THz frequencies. This study, along with other pioneering works that focus on the phonon-induced THz nonlinear optical response of material media, lay the groundwork for some more comprehensive studies: There are more materials to be studied, and there are other nonlinear optical effects that can be considered. One of the key limiting factors of the experimental studies performed in this thesis is the relatively narrow THz spectrum of the source, which is forced primarily by the time duration of the pump pulse, phase-matching of the nonlinear process during THz pulse generation, as well as the limited frequency response of the THz detection materials. There have been efforts to overcome the limited spectral bandwidth of the THz generation and detection by using new generation and detection materials, or by manipulating the phase matching conditions [56, 119].

There are many other unanswered interesting questions. For instance, how large would

be the nonlinear response of the solids at the location of their absorption resonances if we can extend the spectral range of the THz source to reach these resonances, or whether it is possible to observe the self-focusing of the THz beam, as discussed in Chapter 3, by getting rid of the linear dispersion effects using a narrow-band THz source that propagates through solids. The answer to these questions can help to make use of THz nonlinear optics in various applications, including nonlinear THz spectroscopy, sensing, imaging, and communications. We leave these to a future work.

Bibliography

[1] N. M. Burford and M. O. El-Shenawee. “Review of terahertz photoconductive antenna technology”. In: *Optical Engineering* 56.1 (2017), pp. 1–20.

[2] M. Hangyo, M. Tani, and T. Nagashima. “Terahertz Time-Domain Spectroscopy of Solids: A Review”. In: *International Journal of Infrared and Millimeter Waves* 26 (2005), p. 1661.

[3] B. Fischer et al. “Chemical recognition in terahertz time-domain spectroscopy and imaging”. In: *Semiconductor Science and Technology* 20.7 (June 2005), S246–S253.

[4] E. P. J. Parrott, Y. Sun, and E. Pickwell-MacPherson. “Terahertz spectroscopy: Its future role in medical diagnoses”. In: *Journal of Molecular Structure* 1006.1 (2011), pp. 66–76.

[5] T. Kleine-Ostmann and T. Nagatsuma. “A Review on Terahertz Communications Research”. In: *Journal of Infrared, Millimeter, and Terahertz Waves* 32.2 (2011), pp. 143–171.

[6] J. Lloyd-Hughes and T-I Jeon. “A Review of the Terahertz Conductivity of Bulk and Nano-Materials”. In: *Journal of Infrared, Millimeter, and Terahertz Waves* 33 (2013), p. 1866.

[7] R. Valdés Aguilar et al. “Terahertz Response and Colossal Kerr Rotation from the Surface States of the Topological Insulator Bi_2Se_3”. In: *Phys. Rev. Lett.* 108 (8 Feb. 2012), p. 087403.

[8] R. Matsunaga et al. “Higgs Amplitude Mode in the BCS Superconductors $Nb_{1-x}Ti_xN$ Induced by Terahertz Pulse Excitation”. In: *Phys. Rev. Lett.* 111 (5 July 2013), p. 057002.

[9] J. Li and K. Chang. “Electric field driven quantum phase transition between band insulator and topological insulator”. In: *Applied Physics Letters* 95.22 (2009), p. 222110.

[10] T. Otsuji et al. “Graphene-based devices in terahertz science and technology”. In: *Journal of Physics D: Applied Physics* 45.30 (July 2012), p. 303001.

[11] P. Y. Han et al. “A direct comparison between terahertz time-domain spectroscopy and far-infrared Fourier transform spectroscopy”. In: *Journal of Applied Physics* 89.4 (2001), pp. 2357–2359.

[12] G. Matthäus et al. “Surface-emitted THz generation using a compact ultrashort pulse fiber amplifier at 1060nm”. In: *Optics Communications* 261.1 (2006), pp. 114–117.

[13] X. Xie, J. Dai, and X.-C. Zhang. “Coherent Control of THz Wave Generation in Ambient Air”. In: *Phys. Rev. Lett.* 96 (7 Feb. 2006), p. 075005.

[14] H. Hamster et al. “Subpicosecond, electromagnetic pulses from intense laser-plasma interaction”. In: *Phys. Rev. Lett.* 71 (17 Oct. 1993), pp. 2725–2728.

[15] D. H. Auston, K. P. Cheung, and P. R. Smith. “Picosecond photoconducting Hertzian dipoles”. In: *Applied Physics Letters* 45.3 (1984), pp. 284–286.

[16] M. B. Ketchen et al. “Generation of subpicosecond electrical pulses on coplanar transmission lines”. In: *Applied Physics Letters* 48.12 (1986), pp. 751–753.

[17] R. W. Boyd. *Nonlinear Optics*. Elsevier, 2003.

[18] A. Rice et al. “Terahertz optical rectification from 110 zinc-blende crystals”. In: *Applied Physics Letters* 64.11 (1994), pp. 1324–1326.

[19] A. Nahata, A. S. Weling, and T. F. Heinz. “A wideband coherent terahertz spectroscopy system using optical rectification and electro-optic sampling”. In: *Applied Physics Letters* 69.16 (1996), pp. 2321–2323.

[20] K.-L. Yeh et al. “Generation of 10 micro-J ultrashort terahertz pulses by optical rectification”. In: *Applied Physics Letters* 90.17 (2007), p. 171121.

[21] J. Hebling et al. “Velocity matching by pulse front tilting for large-area THz-pulse generation”. In: *Opt. Express* 10.21 (Oct. 2002), pp. 1161–1166.

[22] H. Hirori et al. “Single-cycle terahertz pulses with amplitudes exceeding 1 MV/cm generated by optical rectification in LiNbO3”. In: *Applied Physics Letters* 98.9 (2011), p. 091106.

[23] K. P. Cheung and D. H. Auston. “A novel technique for measuring far-infrared absorption and dispersion”. In: *Infrared Physics* 26.1 (1986), pp. 23–27.

[24] D. Grischkowsky et al. “Spectroscopy with Ultrashort Electrical Pulses”. In: *Laser Spectroscopy VIII*. Ed. by Willy Persson and Sune Svanberg. Berlin, Heidelberg: Springer Berlin Heidelberg, 1987, pp. 438–443.

[25] J. Hebling et al. “High-Power THz Generation, THz Nonlinear Optics, and THz Nonlinear Spectroscopy”. In: *IEEE Journal of Selected Topics in Quantum Electronics* 14.2 (Mar. 2008), pp. 345–353.

[26] J. Hebling et al. “Generation of high-power terahertz pulses by tilted-pulse-front excitation and their application possibilities”. In: *J. Opt. Soc. Am. B* 25.7 (July 2008), B6–B19.

[27] C. Vicario, B. Monoszlai, and C. P. Hauri. “GV/m Single-Cycle Terahertz Fields from a Laser-Driven Large-Size Partitioned Organic Crystal”. In: *Phys. Rev. Lett.* 112 (21 May 2014), p. 213901.

[28] A. Gopal et al. “Observation of Gigawatt-Class THz Pulses from a Compact Laser-Driven Particle Accelerator”. In: *Phys. Rev. Lett.* 111 (7 Aug. 2013), p. 074802.

[29] F. Blanchard et al. “Generation of 1.5 μJ single-cycle terahertz pulses by optical rectification from a large aperture ZnTe crystal”. In: *Opt. Express* 15.20 (Oct. 2007), pp. 13212–13220.

[30] H. Yoneda et al. “High-power terahertz radiation emitter with a diamond photoconductive switch array”. In: *Appl. Opt.* 40.36 (Dec. 2001), pp. 6733–6736.

[31] C. W. Berry, M. R. Hashemi, and M. Jarrahi. “Generation of high power pulsed terahertz radiation using a plasmonic photoconductive emitter array with logarithmic spiral antennas”. In: *Applied Physics Letters* 104.8 (2014), p. 081122.

[32] H. A. Hafez et al. “Intense terahertz radiation and their applications”. In: *Journal of Optics* 18.9 (Aug. 2016), p. 093004.

[33] K. P. Cheung and D. H. Auston. “Excitation of Coherent Phonon Polaritons with Femtosecond Optical Pulses”. In: *Phys. Rev. Lett.* 55 (20 Nov. 1985), pp. 2152–2155.

[34] T. Kampfrath, K. Tanaka, and K. A. Nelson. “Resonant and nonresonant control over matter and light by intense terahertz transients”. In: *Nature Photonics* 7 (2013), p. 680.

[35] P. Gaal et al. “Internal motions of a quasiparticle governing its ultrafast nonlinear response”. In: *Opt. Express* 450.7173 (Dec. 2007), pp. 1210–1213.

[36] H. Hirori and K. Tanaka. “Dynamical Nonlinear Interactions of Solids with Strong Terahertz Pulses”. In: *Journal of the Physical Society of Japan* 85.8 (2016), p. 082001.

[37] A. N. Azarenkov et al. “Fast nonlinearity of the refractive index of solid-state dielectric active media”. In: *Quantum Electronics* 23.8 (Aug. 1993), pp. 633–655.

[38] K. Dolgaleva et al. “Prediction of an extremely large nonlinear refractive index for crystals at terahertz frequencies”. In: *Phys. Rev. A* 92 (2 Aug. 2015), p. 023809.

[39] R. R. Jones, D. You, and P. H. Bucksbaum. “Ionization of Rydberg atoms by subpicosecond half-cycle electromagnetic pulses”. In: *Phys. Rev. Lett.* 70 (9 Mar. 1993), pp. 1236–1239.

[40] D. Turchinovich, J. M. Hvam, and M. C. Hoffmann. “Self-phase modulation of a single-cycle terahertz pulse by nonlinear free-carrier response in a semiconductor”. In: *Phys. Rev. B* 85 (20 May 2012), p. 201304.

[41] A. T. Tarekegne et al. “Impact ionization in high resistivity silicon induced by an intense terahertz field enhanced by an antenna array”. In: *New Journal of Physics* 17.4 (Apr. 2015), p. 043002.

[42] S. Tani, F. Blanchard, and K. Tanaka. “Ultrafast Carrier Dynamics in Graphene under a High Electric Field”. In: *Phys. Rev. Lett.* 109 (16 Oct. 2012), p. 166603.

[43] C. Lange et al. “Extremely Nonperturbative Nonlinearities in GaAs Driven by Atomically Strong Terahertz Fields in Gold Metamaterials”. In: *Phys. Rev. Lett.* 113 (22 Nov. 2014), p. 227401.

[44] P. Gaal et al. “Nonlinear Terahertz Response of *n*-Type GaAs”. In: *Phys. Rev. Lett.* 96 (18 May 2006), p. 187402.

[45] X. Chai et al. “Subcycle Terahertz Nonlinear Optics”. In: *Phys. Rev. Lett.* 121 (14 Oct. 2018), p. 143901.

[46] H. Y. Hwang et al. “Nonlinear THz Conductivity Dynamics in P-Type CVD-Grown Graphene”. In: *The Journal of Physical Chemistry B* 117 (49 2013), pp. 15819–15824.

[47] L. Razzari et al. “Nonlinear ultrafast modulation of the optical absorption of intense few-cycle terahertz pulses in *n*-doped semiconductors”. In: *Phys. Rev. B* 79 (19 May 2009), p. 193204.

[48] H. A. Hafez et al. “Extremely efficient terahertz high-harmonic generation in graphene by hot Dirac fermions”. In: *Nature* 561 (7724 Sept. 2018), pp. 507–511.

[49] O. Schubert et al. “Sub-cycle control of terahertz high-harmonic generation by dynamical Bloch oscillations”. In: *Nature Photonics* 8 (2 2014), pp. 119–123.

[50] C. Flytzanis and N. Bloembergen. “Infrared Dispersion of Third-order Susceptibilities in Dielectrics: Retardation Effects”. In: *Progress in Quantum Electronics* 4 (1976), pp. 271–300.

[51] J. Hebling et al. “Nonlinear Lattice Response Observed Through Terahertz SPM”. In: *Ultrafast Phenomena XVI*. Ed. by Paul Corkum et al. Berlin, Heidelberg: Springer Berlin Heidelberg, 2009, pp. 651–653.

[52] K. J. Blow and D. Wood. “Theoretical description of transient stimulated Raman scattering in optical fibers”. In: *IEEE Journal of Quantum Electronics* 25.12 (Dec. 1989), pp. 2665–2673.

[53] H. Hirori et al. “Single-cycle terahertz pulses with amplitudes exceeding 1 MV/cm generated by optical rectification in LiNbO3”. In: *Applied Physics Letters* 98.9 (2011), p. 091106.

[54] H. Zhong, N. Karpowicz, and X.-C. Zhang. “Terahertz emission profile from laser-induced air plasma”. In: *Applied Physics Letters* 88.26 (2006), p. 261103.

[55] M. Shalaby and C. P. Hauri. “Demonstration of a low-frequency three-dimensional terahertz bullet with extreme brightness”. In: *Nature Communications* 6.5976 (Jan. 2015), pp. 4573–4580.

[56] C. Vicario et al. “High efficiency THz generation in DSTMS, DAST and OH1 pumped by Cr:forsterite laser”. In: *Opt. Express* 23.4 (Feb. 2015), pp. 4573–4580.

[57] J. Hebling et al. “Generation of high-power terahertz pulses by tilted-pulse-front excitation and their application possibilities”. In: *J. Opt. Soc. Am. B* 25.7 (July 2008), B6–B19.

[58] R. L. Sutherland. *Handbook of Nonlinear Optics*. CRC Press, 2003.

[59] W. D. Johnston and I. P. Kaminow. “Contributions to Optical Nonlinearity in GaAs as Determined from Raman Scattering Efficiencies”. In: *Phys. Rev.* 188 (3 Dec. 1969), pp. 1209–1211.

[60] J. Hebling et al. “Velocity matching by pulse front tilting for large-area THz-pulse generation”. In: *Opt. Express* 10.21 (Oct. 2002), pp. 1161–1166.

[61] A. Schneider, M. Stillhart, and P. Günter. “High efficiency generation and detection of terahertz pulses using laser pulses at telecommunication wavelengths”. In: *Opt. Express* 14.12 (June 2006), pp. 5376–5384.

[62] J. Hebling et al. “Velocity matching by pulse front tilting for large-area THz-pulse generation”. In: *Opt. Express* 10.21 (Oct. 2002), pp. 1161–1166.

[63] P. A. Tipler. *Physics for Scientists and Engineers*. W. H. Freeman, 1999.

[64] L. Pálfalvi et al. “Temperature dependence of the absorption and refraction of Mg-doped congruent and stoichiometric LiNbO3 in the THz range”. In: *Journal of Applied Physics* 97.12 (2005), p. 123505.

[65] J. A. Fülöp et al. “Design of high-energy terahertz sources based on optical rectification”. In: *Opt. Express* 18.12 (June 2010), pp. 12311–12327.

[66] S. Namba. “Electro-Optical Effect of Zincblende”. In: *J. Opt. Soc. Am.* 51.1 (Jan. 1961), pp. 76–79.

[67] Q. Chen et al. “Electro-optic transceivers for terahertz-wave applications”. In: *J. Opt. Soc. Am. B* 18.6 (June 2001), pp. 823–831.

[68] A. Yariv. *Optical Electronics*. London: Oxford University, 1991. Chap. Chap. 9.

[69] M. Naftaly and R. Dudley. “Methodologies for determining the dynamic ranges and signal-to-noise ratios of terahertz time-domain spectrometers”. In: *Opt. Lett.* 34.8 (Apr. 2009), pp. 1213–1215.

[70] T. Brabec and F. Krausz. “Nonlinear Optical Pulse Propagation in the Single-Cycle Regime”. In: *Phys. Rev. Lett.* 78 (17 Apr. 1997), pp. 3282–3285.

[71] M. Kolesik and J. V. Moloney. “Nonlinear optical pulse propagation simulation: From Maxwell’s to unidirectional equations”. In: *Phys. Rev. E* 70 (3 Sept. 2004), p. 036604.

[72] J. Andreasen and M. Kolesik. “Nonlinear propagation of light in structured media: Generalized unidirectional pulse propagation equations”. In: *Phys. Rev. E* 86 (3 Sept. 2012), p. 036706.

[73] A. Couairon et al. “Practitioner’s guide to laser pulse propagation models and simulation”. In: *The European Physical Journal Special Topics* 199.1 (Nov. 2011), pp. 5–76.

[74] M. Kolesik, J. V. Moloney, and M. Mlejnek. “Unidirectional Optical Pulse Propagation Equation”. In: *Phys. Rev. Lett.* 89 (28 Dec. 2002), p. 283902.

[75] M. D. Feit and J. A. Fleck. “Beam nonparaxiality, filament formation, and beam breakup in the self-focusing of optical beams”. In: *J. Opt. Soc. Am. B* 5.3 (Mar. 1988), pp. 633–640.

[76] L. M. Kovachev. “The light filament as vector solitary wave”. In: *AIP Conference Proceedings* 1629.1 (2014), pp. 167–171.

[77] P. Saari. “Evolution of subcycle pulses in nonparaxial Gaussian beams”. In: *Opt. Express* 8.11 (May 2001), pp. 590–598.

[78] J. Dai et al. “Terahertz time-domain spectroscopy characterization of the far-infrared absorption and index of refraction of high-resistivity, float-zone silicon”. In: *J. Opt. Soc. Am. B* 21.7 (July 2004), pp. 1379–1386.

[79] A. Deneuville, D. Tanner, and P. H. Holloway. "Optical constants of ZnSe in the far infrared". In: *Phys. Rev. B* 43 (8 Mar. 1991), pp. 6544–6550.

[80] M. Kolesik. *[Linux or OSX system] simulation framework*. 2019.

[81] G. P. Agrawal. *Nonlinear Fiber Optics*. Academic Press, 2001.

[82] A. Deepak, T. D. Wilkerson, and L. H. Ruhnke. *Atmospheric Water Vapor*. Academic Press, 1980.

[83] D. M. Slocum et al. "Atmospheric absorption of terahertz radiation and water vapor continuum effects". In: *Journal of Quantitative Spectroscopy and Radiative Transfer* 127 (2013), pp. 49–63.

[84] H. Horvath. "Atmospheric light absorption—A review". In: *Atmospheric Environment. Part A. General Topics* 27.3 (1993), pp. 293–317.

[85] R. Mecke. "Das Rotationsschwingungsspektrum des Wasserdampfes. I". In: *Zeitschrift für Physik* 81.5 (May 1933), pp. 313–331.

[86] W. M. Elsasser. "Far Infrared Absorption of Atmospheric Water Vapor". In: *Astrophys. J.* 87 (June 1938), p. 497.

[87] J. Savolainen, S. Ahmed, and P. Hamm. "Two-dimensional Raman-terahertz spectroscopy of water". In: *Proceedings of the National Academy of Sciences* 110.51 (2013), pp. 20402–20407.

[88] A. J. Kemp, J. R. Birch, and M. N. Afsar. "The refractive index of water vapour: A comparison of measurement and theory". In: *Infrared Physics* 18.5 (1978), pp. 827–833.

[89] J. Dong et al. "Global mapping of stratigraphy of an old-master painting using sparsity-based terahertz reflectometry". In: *Scientific Reports* 7.1 (2017), pp. 15098–15110.

[90] K. J. Kaltenecker et al. "Ultrabroadband perfect imaging in terahertz wire media using single-cycle pulses". In: *Optica* 3.5 (May 2016), pp. 458–464.

[91] J. F. Federici et al. "THz imaging and sensing for security applications-explosives, weapons and drugs". In: *Semiconductor Science and Technology* 20.7 (June 2005), S266–S280.

[92] P. Bowlan et al. "Probing and controlling terahertz-driven structural dynamics with surface sensitivity". In: *Optica* 4.3 (Mar. 2017), pp. 383–387.

[93] M-A Brun et al. "Terahertz imaging applied to cancer diagnosis". In: *Physics in Medicine and Biology* 55.16 (July 2010), pp. 4615–4623.

[94] O. A. Smolyanskaya et al. “Glycerol dehydration of native and diabetic animal tissues studied by THz-TDS and NMR methods”. In: *Biomed. Opt. Express* 9.3 (Mar. 2018), pp. 1198–1215.

[95] E. Moon, T. Jeon, and D. R. Grischkowsky. “Long-Path THz-TDS Atmospheric Measurements Between Buildings”. In: *IEEE Transactions on Terahertz Science and Technology* 5.5 (2015), pp. 742–750.

[96] G-R Kim, T-I Jeon, and D. Grischkowsky. “910-m propagation of THz ps pulses through the Atmosphere”. In: *Opt. Express* 25.21 (Oct. 2017), pp. 25422–25434.

[97] M. Brucherseifer et al. “Label-free probing of the binding state of DNA by time-domain terahertz sensing”. In: *Applied Physics Letters* 77.24 (2000), pp. 4049–4051.

[98] Y-D Hsieh et al. “Dynamic terahertz spectroscopy of gas molecules mixed with unwanted aerosol under atmospheric pressure using fibre-based asynchronous-optical-sampling terahertz time-domain spectroscopy”. In: *Scientific Reports* 6.1 (June 2016), p. 28114.

[99] C. D. Stoik, M. J. Bohn, and J. L. Blackshire. “Nondestructive evaluation of aircraft composites using transmissive terahertz time domain spectroscopy”. In: *Opt. Express* 16.21 (Oct. 2008), pp. 17039–17051.

[100] S. Kaushik. “Silicon-based Terahertz circuits and systems”. PhD thesis. California Institute of Technology, June 2012.

[101] Y. Yang, M. Mandehgar, and D. R. Grischkowsky. “Broadband THz Signals Propagate Through Dense Fog”. In: *IEEE Photonics Technology Letters* 27.4 (2015), pp. 383–386.

[102] Y. Yang, M. Mandehgar, and D. R. Grischkowsky. “Understanding THz Pulse Propagation in the Atmosphere”. In: *IEEE Transactions on Terahertz Science and Technology* 2.4 (2012), pp. 406–415.

[103] M. V. Exter, C. Fattinger, and D. Grischkowsky. “Terahertz time-domain spectroscopy of water vapor”. In: *Opt. Lett.* 14.20 (Oct. 1989), pp. 1128–1130.

[104] I. E. Gordon et al. “The HITRAN2016 molecular spectroscopic database”. In: *Journal of Quantitative Spectroscopy and Radiative Transfer* 203 (2017), pp. 3–69.

[105] H. Hoshina et al. “Precise measurement of pressure broadening parameters for water vapor with a terahertz time-domain spectrometer”. In: *Journal of Quantitative Spectroscopy and Radiative Transfer* 109.12 (2008), pp. 2303–2314.

[106] R. G. Lyons. *Understanding Digital Signal Processing*. Pearson Education, 2011.

[107] P. Rasekh et al. “Terahertz Nonlinear Optical Response of Water Vapor”. In: *arXiv* 2006.04711 (2020).

[108] J. Tennyson et al. “IUPAC critical evaluation of the rotational–vibrational spectra of water vapor, Part III: Energy levels and transition wavenumbers for H216O”. In: *Journal of Quantitative Spectroscopy and Radiative Transfer* 117 (2013), pp. 29–58.

[109] H. R. Carlon. “Do clusters contribute to the infrared absorption spectrum of water vapor?” In: *Infrared Physics* 19.5 (1979), pp. 549–557.

[110] H. R. Carlon. “Infrared absorption by molecular clusters in water vapor”. In: *Journal of Applied Physics* 52.5 (1981), pp. 3111–3115.

[111] K. Johnson et al. “Water vapor: An extraordinary terahertz wave source under optical excitation”. In: *Physics Letters A* 372.38 (2008), pp. 6037–6040.

[112] Z. Dai et al. “A combined experimental and theoretical study on the terahertz vibrations of water vapors”. In: *Spectrochimica Acta Part A: Molecular and Biomolecular Spectroscopy* 214 (2019), pp. 277–284.

[113] P. Rasekh et al. “Propagation of broadband THz pulses: effects of dispersion, diffraction and time-varying nonlinear refraction”. In: *Opt. Express* 28.3 (Feb. 2020), pp. 3237–3248.

[114] M. C. Hoffmann et al. “Terahertz Kerr effect”. In: *Applied Physics Letters* 95.23 (2009), p. 231105.

[115] M. Zalkovskij et al. “Terahertz-induced Kerr effect in amorphous chalcogenide glasses”. In: *Applied Physics Letters* 103.22 (2013), p. 221102.

[116] M. Cornet et al. “Terahertz Kerr effect in gallium phosphide crystal”. In: *J. Opt. Soc. Am. B* 31.7 (July 2014), pp. 1648–1652.

[117] M. Naftaly and R. E. Miles. “Terahertz Time-Domain Spectroscopy for Material Characterization”. In: *Proceedings of the IEEE* 95.8 (2007), pp. 1658–1665.

[118] M. J. Jackson and B. Mills. “Thermal expansion of alumino-alkalisilicate and alumino- borosilicate glasses – comparison of empirical models”. In: *J. Mater* 16.15 (1997), pp. 1264–1266.

[119] A. Halpin et al. “Enhanced Terahertz Detection Efficiency via Grating-Assisted Noncollinear Electro-Optic Sampling”. In: *Phys. Rev. Applied* 12 (3 Sept. 2019), p. 031003.